Confocal and cavity-enhanced spectroscopy of semiconductor van der Waals heterostructures

Michael Förg

München 2020

Confocal and cavity-enhanced spectroscopy of semiconductor van der Waals heterostructures

Michael Förg

Dissertation
der Fakultät für Physik
der Ludwig-Maximilians-Universität
München

vorgelegt von
Michael Förg
aus Mindelheim

München, den 08.06.2020

Erstgutachter: Prof. Dr. Alexander Högele
Zweitgutachter: Prof. Dr. Alexander Urban
Tag der mündlichen Prüfung: 28.07.2020

Zusammenfassung

Heterostrukturen zweidimensionaler Materialien zeichnen sich durch vielversprechende elektronische und optische Eigenschaften aus. Eine sehr bekannte Klasse dieser Heterostrukturen ist aus Monolagen von Übergangsmetalldichalkogeniden aufgebaut. Innerhalb der einzelnen Lagen finden sich unter Photoanregung stark gebundene Exzitonen mit valley-spezifischen optischen Auswahlregeln. Diese valleytronischen Charakteristiken werden an langlebige Interlagenexzitonen vererbt, die sich in künstlich arrangierten Heterostrukturen erzeugen lassen und ein statisches Dipolmoment senkrecht zur Ebene besitzen.

In dieser Arbeit wurden Heterostrukturen aus Molybdändiselenid und Wolframdiselenid mit Methoden der optischen Spektroskopie untersucht. Basierend auf Messungen der Frequenzverdoppelung, differentieller Reflektion, sowie energie- und zeitaufgelöster Photolumineszenz konnte das atomare Register gewachsener Heterobilagen bestimmt werden. In diesem Zusammenhang wurden die optischen Übergänge als Faltung von Interlagenexzitonen in verschiedenen Spin- und Valleykonfigurationen modelliert. Daraufhin wurde die Licht-Materie-Wechselwirkung dieser Kanäle mit einem kryogenen Rasterscanresonator untersucht. Nach der Charakterisierung des Systems wurde seine Längendurchstimmbarkeit genutzt, um die Rekombinationsrate zu verstärken. Diese Messungen erlaubten es, die Raten der Licht-Materie-Wechselwirkung für alle drei Zerfallskanäle zu berechnen. Zusätzlich wurde die Absorption der Interlagenexzitonen in einem hochreflektiven Resonatorsystem gemessen. Der Wert der Absorption stimmt mit den vorangegangenen konfokalen Messungen überein und weist auf eine Dehnungsempfindlichkeit der Polarisation von Interlagenexzitonen hin.

Zuletzt wurden Heterobilagen und Heterotrilagen im Hinblick auf den Einfluss einer zusätzlichen Lage auf die optischen Übergänge miteinander verglichen. Konfokale Spektroskopie wurde durch numerische Berechnungen der Dichtefunktionaltheorie ergänzt. Magnetolumineszenz-Experimente ermöglichten es, zusammen mit den theoretischen Vorhersagen, impulsdirekte Übergänge in der Heterobilage von impulsindirekten Übergängen in der Heterotrilage zu unterscheiden. Diese Erkenntnisse tragen zum Verständnis der optischen Eigenschaften von Heterostrukturen aus Übergangsmetalldichalkogeniden bei und ermöglichen die Konstruktion komplexerer vertikaler Anordnungen.

Abstract

Heterostructures of layered two-dimensional materials have attracted much attention in modern solid state physics due to their promising transport and optical properties. A very prominent class of heterostructures are build of monolayer transition metal dichalcogenides. After photoactivation, the single-layer components host tightly bound excitons with valley-contrasting optical selection rules. Inheriting these valleytronic characteristics, long-lived interlayer excitons with a permanent out-of-plane dipole moment can arise in artificially assembled heterostructures.

Within this thesis, heterostructures of molybdenum diselenide and tungsten diselenide were studied with optical spectroscopy. Based on measurements of second harmonic generation, differential reflectance as well as energy and time-resolved photoluminescence, the atomic registry of grown heterobilayers was determined. In this context, the optical transitions were modeled as a convolution of interlayer excitons in various spin and valley configurations. Subsequently, the light-matter coupling of these recombination channels was probed by a cryogenic scanning cavity setup. After an initial characterization of the system, its length-tunability was used to enhance the interlayer exciton recombination in the limit of weak coupling. These measurements enabled to infer the light-matter coupling rates for all decay channels. In addition, interlayer exciton absorption was tested in a high finesse scanning cavity system. The measured absorption strength is consistent with the initial confocal studies and indicates a strain-susceptibility of interlayer exciton polarization.

Finally, heterobilayer and heterotrilayer structures were investigated in direct comparison, probing the influence of an additional layer of molybdenum diselenide upon the optical transitions. Confocal spectroscopy methods were complemented by numerical calculations using density functional theory. Magneto-luminescence experiments were performed and enabled, along with theorical predictions, to differentiate the momentum direct transition in the heterobilayer from momentum-indirect transition in the heterotrilayer. These results shed light on the intrinsic optical properties of transition metal dichalcogenide heterostructures and facilitate the design of more complex vertical arrangements.

Contents

Chapter 1

Introduction

Advancing from a two-dimensional (2D) area to a three-dimensional space is described in Edwin A. Abbott's novella *Flatland: A romance of many dimensions* [1] with the words "it is Knowledge; it is Three Dimensions: open your eye once again and try to look steadily." A similar change of perception is taking place in modern solid state physics, where increasingly complex vertical arrangements are built from layered materials. The discovery of graphene [2], a crystal structure of carbon atoms arranged in two dimensions, started a focused research interest in these materials in the flatland more than a decade ago [3]. As a result, the unique transport phenomena in graphene have been supplemented by families of insulating [4, 5], semiconducting [6], magnetic [7] and ferroelectric [8] 2D materials, to name a few. All these nanosheets share strong in-plane bonds leading to their 2D nature. The individual layers, in contrast, are held together by weak van der Waals forces facilitating the fabrication of monolayer (ML) crystals by means of mechanical exfoliation [2, 9], but also enabling the reversed process of building artificial stacks and heterostructures [10]. Harvesting the benefits of the single components, this route into the third dimension is not only opening the door towards a plethora of new physical phenomena, but comes with the promise of applications like wearable devices, photovoltaics and batteries [11, 12].

Heterostructures built from the semiconducting class of transition metal dichalchogenides (TMDs) are one auspicious platform to study within the diverse family of layered materials. In this thesis, optical characteristics of heterostacks made of the two representative TMD constituents molybdenum diselenide ($MoSe_2$) and tungsten diselenide (WSe_2) were studied. The individual MLs exhibit a direct band gap at the K and K' points of the Brillouin zone [13] and a high exciton binding energy giving rise to tightly bound excitons up to room temperature [14, 15]. Strong spin-orbit coupling along with a broken inversion symmetry leads to different optical selection rules in K and K' and enables the direct addressing of the individual

valleys with circularly polarized light of opposite helicity [16, 17]. In heterobilayers (HBLs) of $MoSe_2$ and WSe_2, a staggered band alignment [18] facilitates the formation of layer-separated excitonic complexes with a permanent out-of-plane dipole moment. The reduced wavefunction overlap leads to extended lifetimes up to several hundred nanoseconds [19–22]. Inheriting the valley-contrasting properties of their ML components, these long lived bosonic quasiparticles are, on the one hand, promising candidates to investigate condensation [23] and expansion [24] phenomena of optically addressable dipolar gases. On the other hand, they display application-relevant properties like gate-tunable polarization switching of optical helicity [25] or spin-valley conserving exciton transport [26].

The increased dimensionality of heterostructures becomes apparent in the vertical arrangement of HBLs. Assuming similar lattice constants of $MoSe_2$ and WSe_2 there are already six distinct stacking alignments of the two layers [27, 28]. Such commensurate systems, in which the opto-electronic properties are associated with one atomic registry, can be realized by chemical vapor deposition (CVD) of $MoSe_2$-WSe_2 HBLs and the accompanying accommodation of small lattice mismatches by atomic vacancies [29, 30]. Additional complexity arises in the presence of moiré-modulated structures made via exfoliation-stacking. The spatial variation of the electronic band structure induced by the moiré superlattice [31] gives rise to correlated phenomena within TMD HBLs [32, 33].

Starting with a naturally aligned $MoSe_2$-WSe_2 HBL made via CVD-growth, the intrinsic optical properties of interlayer transitions were studied in this work. Using confocal spectroscopic methods including second harmonic generation (SHG), photoluminescence (PL) and differential reflectance (DR) we determined the atomic registry of the grown structure and interpreted the optical transitions in the framework of interlayer excitons in distinct spin and valley configurations. Expanding the variety of optical inspection we employed a microcavity-system to probe the light-matter interaction of the different interlayer exciton species. Motivated by the observation of strong exciton-photon coupling in TMD MLs [34–38] and the possibility of dipolar exciton-polaritons and condensates in HBL systems, we inferred the light-matter interaction strength from cavity-induced Purcell enhancement in the weak coupling regime. Finally, we follow the route into three dimensions by spectroscopic studies of a $MoSe_2$-WSe_2 heterostructure with HBL and heterotrilayer (HTL) regions supplemented by theoretical calculations. A global twist angle within the sample simplified the comparison of both structures and enabled to shed light onto the direct or indirect nature of the band gap of HBLs and HTLs.

Scope of the thesis

This thesis is structured as follows:

Starting with basic aspects of layered semiconductors, Chapter 2 introduces the structure and optoelectronic properties of TMD MLs, HBLs and HTLs. The individual stacking possibilities within relevant heterostructures are discussed along with corresponding optical selection rules. Expanding the theoretical review, fundamental characteristics of optical resonators are elaborated in Chapter 3. The description includes basic derivations for optical resonators, peculiarities of fiber-based microcavities as well as a short summary of light-matter interaction.

Chapter 4 describes the experimental methods used for the subsequent experiments. The confocal microscope for cryogenic spectroscopy is presented along with modifications to operate in a scanning-cavity configuration. The description of spectroscopic methods is complemented by the different approaches of sample fabrication.

HBLs of $MoSe_2$ and WSe_2 were studied with confocal spectroscopy probing the interlayer exciton recombination (Chapter 5). A model of interlayer excitons in distinct spin and valley configurations is introduced based on comprehensive spectroscopic measurements. Subsequently, the light-matter coupling of interlayer excitons was tested with a cryogenic microcavity system (Chapter 6).

The influence of an additional $MoSe_2$ layer on the direct nature of the band gap is presented in Chapter 7. A gate-tunable sample featuring HBL and HTL regions was investigated confocally under varying excitation powers and external magnetic fields. In comparison with theoretical calculations the results allow to determine the direct and indirect radiative transitions.

Finally, Chapter 8 summarizes the experimental results and provides perspectives on subsequent research.

Chapter 2

Basic aspects of transition metal dichalcogenides

In this chapter, an overview of relevant physical properties of TMDs is given. Starting with a ML, parameters like crystal structure, phonons as well as the opto-electronic properties are summarized. Afterwards, we focus on the discussion of heterostructures made from molybdenum and tungsten diselenide. Possible aligned stackings of commensurate lattices are shown along with a general description of band offsets and electronic band structure calculations based on density functional theory. Complementary to the numerical results, symmetry analysis is employed to derive optical selection rules for interlayer excitons in HBL systems. Finally, a twist angle between the lattices is introduced giving rise to the observation of moiré lattices.

2.1 Review on monolayer physics

PARTS OF THIS SECTION ARE ADAPTED FROM THE MANUSCRIPT [P1]
Lindlau, J., Robert, C., Funk, V., Förg, M., Colombier, L., Neumann, A., Taniguchi, T., Watanabe, K., Glazov, M. M., Marie, X., Urbaszek, B. & Högele, A. Identifying optical signatures of momentum-dark excitons in monolayer transition metal dichalcogenides. *arXiv preprint.* arXiv: 1710.00988 (2017)

MLs are the building blocks of van der Waals heterostructures opening up new functionalities and physical phenomena. Therefore, it is instructive to give a short review on the intrinsic properties of these single layer components.

2.1.1 Crystal structure and lattice vibrations

TMDs are layered materials with the formula MX_2, where M is a transition metal element and X are chalcogen atoms. They form covalently bonded X-M-X structures with two atomic planes of chalcogen atoms seperated by a plane of metal atoms [6] as shown in Figure 2.1a While these individual layers can exist in three phase configurations 1H, 1T and 1T′ [39], we focus on a description of group-VI TMDs in the 1H phase relevant for our work. In this case, the atomic planes of a ML arrange in a hexagonal lattice illustrated in Figure 2.1b. Similar to graphene [2], those MLs are bound together by weak van der Waals forces in the bulk material. Therefore, it is possible to reach the limit of a single layer by means of mechanical exfoliation [9], but also bottom-up approaches have been established like growing MLs via CVD [40] or molecular beam epitaxy [41].

In bulk, those TMD crystals belong to the D^4_{6h} symmetry group, which reduces to D^1_{3h} in the ML due to the broken inversion symmetry [17]. This honeycomb-like lattice symmetry also leads to a hexagonal symmetry in reciprocal space (Figure 2.1c). Here, the extrema of valence band (VB) and conduction band (CB) are located at the K and K' points of the first Brillouin zone [13], defining the main contributions to the ML photo-physics. In addition to that, charge carriers residing in Γ and Q exhibit non-negligible contributions, making them relevant for the following considerations.

In context of the crystal structure, it is instructive to discuss lattice vibrations induced by small displacements of the individual atoms. With three atoms in a unit cell, TMD MLs of the form MX_2 have 9 phonon branches. They can be grouped into in-plane and out-of-plane vibrational modes with different symmetry properties [42].

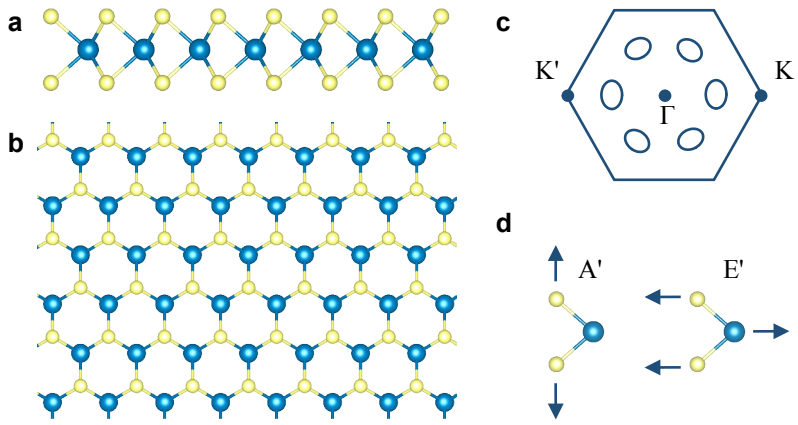

Figure 2.1: Side view (**a**) and top view (**b**) of a transition metal dichalchogenide (MX_2) in 1H phase. The transition metal atoms (M) are colored in blue, chalcogen atoms (X) in yellow. **c**, Schematic drawing of the Brillouin zone inheriting the hexagonal symmetry with band extrema at K and K′. Additionally, the local conduction band minima of Q-pockets are indicated as six ellipses. **d**, Schematic drawing of optical vibrational modes with out-of-plane (A′) and in-plane (E′) motion of the lattice atoms.

Out of those, only the in-plane acoustic (LA, TA) and optical (LO, TO) modes with E′ symmetry as well as the out-of-plane A_1 mode with A′ symmetry are relevant to the scattering with electrons or holes [43]. A schematic drawing of such lattice vibrations is shown in Figure 2.1d. The scattering interaction introduces phonon-assisted recombination pathways for excitons in mono- and multilayered TMDs and is therefore a significant parameter in the scope of this work. Jin, Li, Mullen, *et al.* [43] calculated the respective phonon energies at high symmetry points of the Brilluoin zone. In Table 2.1 those energies are reproduced for $MoSe_2$ and WSe_2.

	$MoSe_2$			WSe_2		
Mode	Γ	K	Q	Γ	K	Q
TA	0	16.6	13.3	0	15.6	11.6
LA	0	19.9	16.9	0	18.0	14.3
TO(E′)	36.1	35.5	36.4	30.5	26.7	27.3
LO(E′)	36.6	37.4	37.5	30.8	31.5	32.5
A_1	30.3	25.6	27.1	30.8	31.0	30.4

Table 2.1: Phonon mode energies in meV at the high-symmetry points of the first Brillouin zone for ML $MoSe_2$ and WSe_2 according to Reference [43].

It might be important to note that multi-layered structures can have additional corrections to their phonon energies [44]. Furthermore, heterostructures can exhibit low-energy interlayer phonons arising from layer breathing modes of two incommensurate layers [45]. An extensive summary of phonons in layered materials is given in Reference [46].

2.1.2 Optoelectronic properties

After summarizing the structural and mechanical properties of TMD MLs, we discuss optolectonic characteristics focusing on the two materials $MoSe_2$ and WSe_2, which are most relevant for the subsequent experiments. In their ML form they are direct band gap semiconductors with CB minimum and VB maximum at the K and K' points of the hexagonal Brillouin zone [13]. At these extrema, the main contribution to VB and CB stems from d orbitals of the transition metal atoms imposing a strong spin orbit coupling [13, 47]. Together with the broken inversion symmetry, this leads to coupled spin and valley physics in those TMD MLs [17]. While VB states exhibit a spin splitting of several hundred meV [41, 47], the CB is split by only few tens of meV [48, 49]. The VB mainly consists of metal d orbitals with $\mathrm{m} = \pm 2$ resulting in a strong spin-orbit coupling. In contrast, the predominantly contributing orbitals in the CB have $\mathrm{m} = 0$, canceling this effect. Minor contributions from p orbitals, however, lead to a finite splitting that can have a different sign for the individual MLs [48]. A schematic illustration of this single particle band structure can be found in Figure 2.2 for $MoSe_2$ and WSe_2. In addition to the K and K' valleys, the CB of TMD MLs exhibits local minima at six non-equivalent Q-pockets related pairwise by time-reversal symmetry [35, 50]. Depending on the specific material and the details of calculations, the Q-valley band-edges can be as far as $\Delta_{\mathrm{KQ}} \simeq 160$ meV above the CB minimum as in $MoSe_2$, or in the range of $\sim 0 - 80$ meV in tungsten-based MLs [43, 49, 51].

With binding energies of several hundred meV [14], the photo-physics of TMD MLs are dominated by Coulomb-correlated electron-hole pairs forming excitonic complexes. These excitons have a Bohr radius on the order of a few nm with electron-hole correlation extending over several lattice periods and can be described as Wannier-Mott type [52]. Our spectroscopic studies will focus on excitons made from holes residing in the upper spin-split VB at K and K'. In the simplest case, an exciton is formed with electron and hole residing in the same valley with a parallel spin configuration of conduction and valence band. Those excitons can recombine via

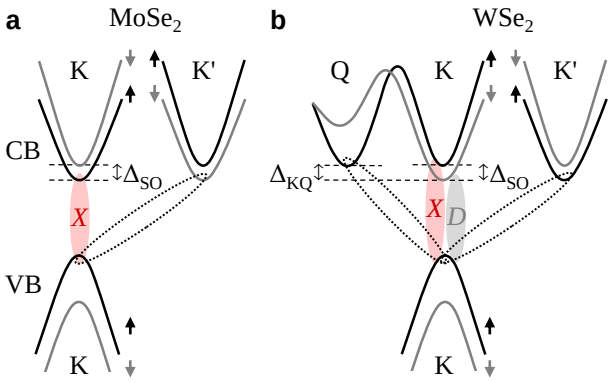

Figure 2.2: Schematic band structure at high symmetry points in the first Brillouin zone of molybdenum (**a**) and tungsten (**b**) dichalcogenide MLs. CB and VB with spin-up and spin-down electron sub-bands (shown in black and grey, respectively), spin-orbit splitting Δ_{SO}, and the energy separation Δ_{KQ} between the CB minima at K and Q. Momentum-direct spin-bright and spin-forbidden excitons (X and D, indicated by ellipses shaded in red and grey) are formed by electrons and unoccupied states in the K-valley. Momentum-dark excitons (dashed ellipses) with the empty state at K can be formed with electrons at Q or K'.

out-of-plane emission of a photon and are labeled as X excitons in Figure 2.2. The optical selection rules for these bright excitons at K valleys can be deduced from symmetry analysis [16, 17] and reveal chiral transitions: excitons at K (K') couple to σ^+ (σ^-) polarized light. This valley-contrasting circular dichroism permits to probe the spin-valley polarization of excitons by means of optical spectroscopy.

With an antiparallel spin configuration between upper VB and lowest lying CB, WSe_2 favors the formation of spin-forbidden excitons indicated as D in Figure 2.2. Coupling to light with out-of-plane polarization these transitions are forbidden for excitation or detection at normal incidence, but can be experimentally observed with high numerical aperture (NA) objectives [53] or brightened up by applying an in-plane magnetic field [54, 55]. In addition to direct excitons, also excitons with finite center-of-mass momenta can be constructed from electrons in valleys other than the hole in K. They are indicated in Figure 2.2 with dashed ellipses and do not recombine directly via photon emission but require the assistance of acoustic or optical phonons. A detailed summary of excitons in layered semiconductors and their optoelectronic properties is presented in Reference [52].

2.2 Properties of $MoSe_2$-WSe_2 heterostructures

THIS SECTION IS PARTLY BASED ON THE PUBLICATION [P2] AND THE MANUSCRIPT [P3]

Förg, M., Colombier, L., Patel, R. K., Lindlau, J., Mohite, A. D., Yamaguchi, H., Glazov, M. M., Hunger, D. & Högele, A. Cavity-control of interlayer excitons in van der Waals heterostructures. *Nature Communications* **10,** 3697 (2019)

Förg, M., Baimuratov, A. S., Kruchinin, S. Y., Vovk, I. A., Scherzer, J., Förste, J., Funk, V., Watanabe, K., Taniguchi, T. & Högele, A. Moiré excitons in $MoSe_2$-WSe_2 heterobilayers and heterotrilayers. *arXiv preprint.* arXiv: 2006.09105 (2020)

Based on the preceding overview of ML physics, we investigate TMD structures made of two or more layers in the following. Since the complex photophysics within heterostructures arises from the vertical arrangement of the individual layers, the subsequent section covers a geometrical analysis of HBLs and HTLs.

2.2.1 Stacking types of commensurate lattices

The first step in constructing TMD heterostructures is to stack individual layers on top of each other. In perspective of complex vertical arrangements with finite twist-angles and differing lattice constants (i.e. 0.1% for $MoSe_2$ and WSe_2 [56]) it is instructive to start with a simplified model of two commensurate and rotationally aligned lattices for basic considerations. In homobilayer systems, featuring equal lattice constants by default, there are five possibilities to align two layers on top of each other with the AA' atomic registry being the energetically most stable and therefore characteristic for the unit cell of bulk TMDs [56].

In HBL systems the number of possible alignments increases to six, which can be grouped into two stacking geometries. While for R-type stacking the in-plane crystalline axes of the two layers are along the same direction with $0°$ twist angle, the two layers exhibit a $60°$ twist for H-type stacking. Within both of these two groups, there are three possible arrangements, each accessible by a lateral translation of one layer with respect to the other [27, 28]. It is important to note, that for $MoSe_2$-WSe_2 HBLs the simplification of commensurate lattices is valid for CVD-grown systems, since the small lattice mismatch can be accommodated by atomic vacancies [29, 30]. Side and top views of corresponding atomic registries are presented as schematic drawings in Figure 2.3.

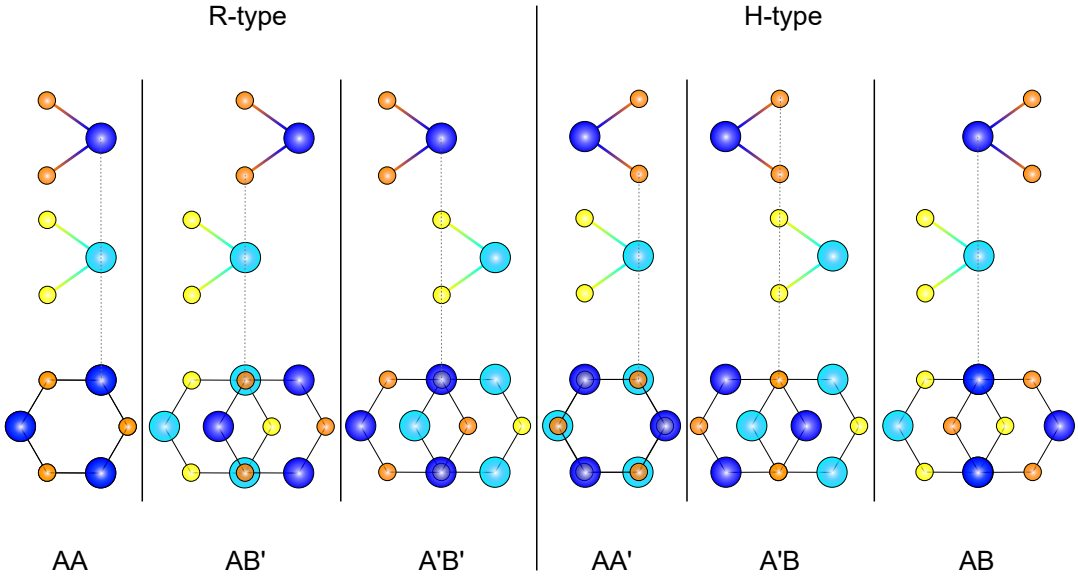

Figure 2.3: High symmetry atomic registries for H- and R-type TMD HBLs shown from side (upper two rows) and from top (lower row). Big and small spheres represent transition metal and chalcogen atoms, respectively. In order to discriminate the two layers they have a different color coding using a cyan-yellow combination for WSe_2 and a blue-orange one for $MoSe_2$. The vertical dashed lines are guidelines to distinguish the individual registries.

The two layers are distinguishable by their color coding (cyan-yellow for WSe_2 and blue-orange for $MoSe_2$) and show the positions of transition metal and chalcogen atoms indicated by big and small spheres, respectively. Vertical dashed lines help to identify the individual stacking. The nomenclature is close to labeling schemes introduced for homobilayers of TMDs [56] and hexagonal boron nitride [57, 58] and has the following step-by-step rules:

The starting layer is labeled with a capital letter A, which is denoting WSe_2 in our case. Subsequent layers are label with capital letters A or B, depending on their arrangement. In a first step, we differentiate between two types of arrangements using similar letters for eclipsed stackings (AA, AA', all atoms are on top of other atoms) and different letters for staggered stackings (AB, AB', A'B, A'B', atoms of one type are on top of hexagon centers). The second step is to fix an atom of the bottom layer, which has an atom of the second layer on top of it, by marking or not marking the first letter of notation with a dash. In our case, A (A') corresponds to the metal (chalcogen) atom, which is fixed for defining the registry. In a final step, we determine the type of atom positioned on top of the fixed bottom layer atom. If they are the same type (metal on top of metal or chalcogen on top of chalcogen) no dash is put to the second

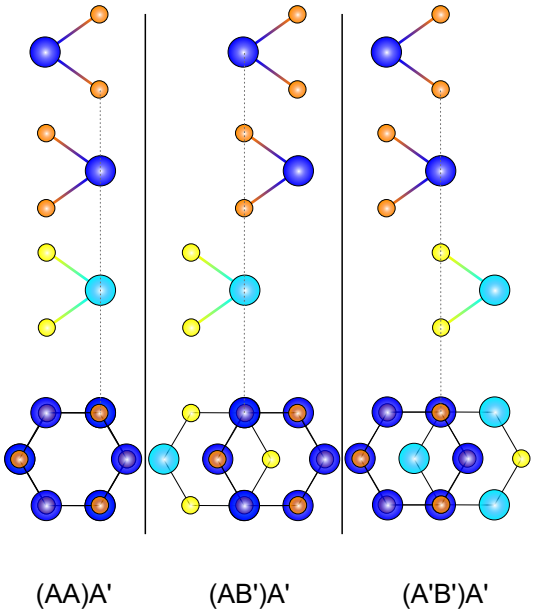

Figure 2.4: High symmetry atomic registries for TMD HTLs consisting of a $MoSe_2$-WSe_2 HBL in R-type arrangement with an additional layer of $MoSe_2$ on top, which is naturally aligned in H-type with the other $MoSe_2$ layer. The same color coding is used as in Figure 2.3.

capital letter. Likewise, a differing atom type is indicated with a dashed symbol.

The same labeling rules can be applied to structures of three or more layers in order to have a precise description of increasingly complex heterostacks. Figure 2.3 shows three examples of a trilayer $MoSe_2$-WSe_2 structure, where an additional layer of $MoSe_2$ was stacked on top of a HBL in R-type arrangement. The additional $MoSe_2$ layer is naturally aligned with respect to the subjacent one. Facilitating straightforward comparison with the previous figure, the three bilayer arrangements are put into brackets. The topmost layer adds an A' to the labels being in eclipsed H-type arrangement with the other $MoSe_2$ layer.

2.2.2 Electronic band structures and Landé g-factors

After analyzing the possible heterostructure arrangements in real space, it is instructive to investigate the reciprocal space of electrons and holes in the following. Starting with structures made of two dissimilar layers, calculations on band offsets show that there are different possible band alignments. While heterostacks made of $MoSe_2$ and tungsten disulfide (WS_2) can exhibit hybridization of CBs [59], $MoSe_2$-WSe_2 HBLs feature a type-II band alignment [18, 60] illustrated in

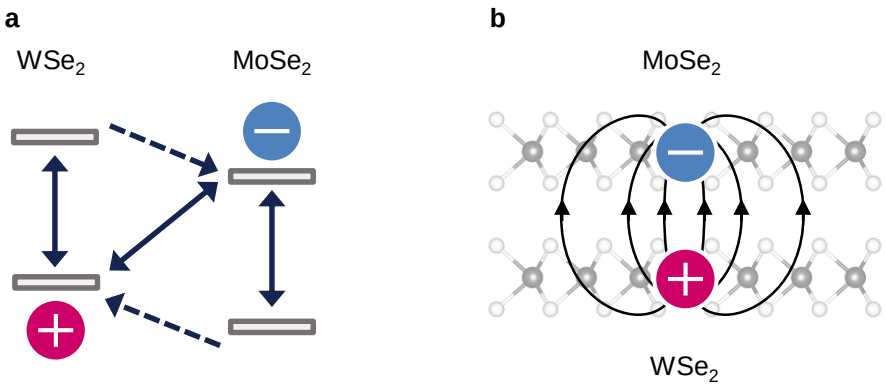

Figure 2.5: **a**, Schematic drawing for type-II band alignment in $MoSe_2$-WSe_2 HBL structures. Band extrema at K and K' are indicated as horizontal grey lines. Dashed lines indicate charge-transfer processes. Possible recombinations from intralayer and interlayer excitons are illustrated with vertical and diagonal arrows, respectively. **b**, Schematic drawing of the corresponding HBL in real space with electron and hole residing in different layers.

Figure 2.5a. Band extrema of the individual layers at K and K' are indicated as horizontal grey lines enabling the formation and recombination of intralayer (vertical arrows) as well as interlayer (diagonal arrow) excitons [19].

While the CB minimum stems from the layer of $MoSe_2$, the VB maximum resides in WSe_2, leading to an accumulation of electrons and holes in the different constituents after excitation. This charge-transfer process happens on femtosecond timescales for TMD heterostructures, thus conserving spin-valley information of the excitation [61]. The layer-separated electron-hole pairs form excitonic states with binding energies of several hundred meV [62] and a permanent dipole moment as schematically illustrated in Figure 2.5b. While the reduced overlap of electron and hole wavefunctions leads to prolonged exciton lifetimes up to several hundreds of nanoseconds [19–21, 26], the permanent dipole moment enables additional electrical control [25]. Inheriting the properties of the contributing MLs, the spin-splitting in the VB from WSe_2 is significantly larger than in the contributing $MoSe_2$ CB. Therefore, interlayer excitons can be formed between the upper VB and both spin-split CBs [19, 25] energetically separated by the $MoSe_2$ CB splitting of 25 meV [48].

So far, only the band offsets of the building block MLs were used, assuming weak interlayer coupling at K and K', in order to approximate the actual band alignment [61, 63]. Recent ab initio calculations on $MoSe_2$-WSe_2 band structures, however, suggest a high sensitivity of the Q valley in the CB as well as the Γ point in the VB to

hybridization effects and propose a lowest lying indirect band gap in these structures [27, 62, 64]. In order to get an insight into the actual band structures for heterostacks of two or more constituent layers we performed ab initio calculations using density functional theory (DFT). The following paragraph summarizes the most important input parameters in our DFT approach. More details are provided in Reference [P4] and Appendix A.

Our first-principle calculations were performed with the PBEsol exchange-correlation functional [65] as implemented in the Vienna ab initio simulation package (VASP) [66]. The van der Waals interactions were considered with the DFT-D3 method by Grimme, Antony, Ehrlich, *et al.* [67] with Becke-Johnson damping [68]. Moreover, spin-orbit interaction was included in all stages. Elementary cells with thickness of 35 Å in the z-direction were used in order to minimize interactions between periodic images. The atomic positions were relaxed with a cutoff energy of 400 eV until the total energy change was less than 10^{-6} eV. Calculations were performed for high-symmetry points of HBL and HTL moiré patterns in R-type stacking on the Γ-centered $\mathbf{k}$ grid of 6×6 divisions with the cutoff energy of 300 eV, with 600 bands for the HBL and 900 bands for the HTL structures. The results for energy gaps and effective masses (in units of free electron mass m_0) are summarized in Tables A.1 and A.2 for HBL and HTL. Based on these DFT results, we used the Wannier exciton model in the effective mass approximation [69] to calculate the exciton energies for the different spin-valley configurations.

Figure 2.6 shows two examples of resulting band structures for a HBL in AA registry (**a**) and a HTL in (AA)A' registry (**b**). In both structures, the VB maximum is at K with a clearly elevated Γ point in the HTL indicating the sensitivity of Γ to the layer number [63]. The CB minimum for the two examples lies at Q, suggesting an indirect band gap for the two registries. In case of the HBL, the energetic separation Δ_{KQ} is very small and can reverse its sign depending on the theoretical model [62]. Therefore, the actual nature of the band gap in HBLs is still under discussion [27, 62, 64] and might be a function of the local strain in the assembled structure [70]. So far, most experimental studies concentrated on the K-K transitions assuming a direct band gap [19, 21, 25, 26]. In contrast to this, the Q valley in Figure 2.6b is clearly lowered, indicating an indirect transition in this type of trilayer registry. Furthermore, the number of contributing CB states at K increases in the HTL due to the additional layer. For interpretation of interlayer exciton emission from HBLs in Chapters 5 and 6, we restrict our analysis upon transitions at K in accordance with precedent experimental studies [19, 21, 25, 26] validating this assumption in Chapter 7.

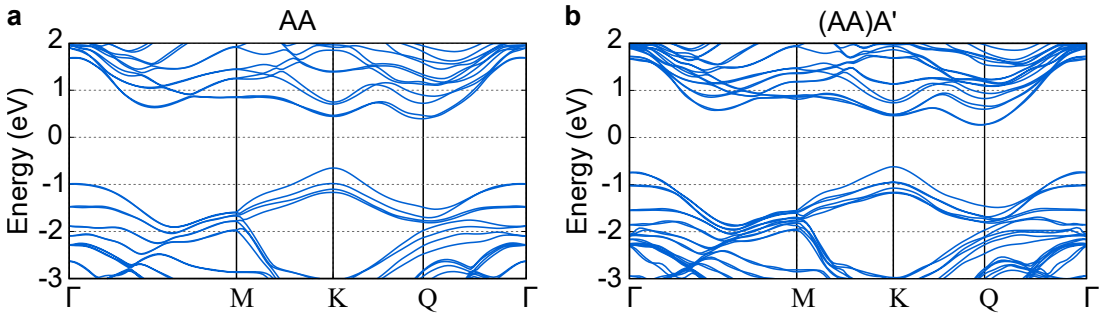

Figure 2.6: Band structure calculations for a $MoSe_2$-WSe_2 HBL in AA registry (**a**) and a HTL in (AA)A' registry (**b**) using density functional theory. In addition to conventional high symmetry points like Γ, K, and M, the position of the Q valley is also labeled. Both structures exhibit the VB maximum at K and the CB minimum at Q. While the separation of Δ_{KQ} is minor for the HBL, it gets pronounced in the trilayer structure, suggesting an indirect band gap for real assembled heterostacks of three layers.

Apart from determining the actual nature of the electronic band gap, DFT can also be used to determine the polarization of optical transitions and exciton g-factors. Examples on calculated excitonic transitions are presented in Chapter 7. Here, we focus on the derivation of the exciton g-factors from the conducted DFT calculations. For a detailed summary, we refer to Reference [P4], summarizing only major points of the analysis in the following.

The exciton is formed by Coulomb correlations between an occupied state in the CB c with the wave vector $\mathbf{k}_c$ and spin z-projection s_c and an empty state in the VB v with the wave vector $\mathbf{k}_v$ and spin z-projection s_v. In this spin-valley configuration, the exciton g-factors is given by

$$g^{(cv)}(\mathbf{k}_c, \mathbf{k}_v) = g_c(\mathbf{k}_c) - g_v(\mathbf{k}_v), \tag{2.1}$$

where the g-factor of the electron in band $n = c, v$ is

$$g_n(\mathbf{k}) = g_0 s_n + 2L_n(\mathbf{k}). \tag{2.2}$$

Here, $g_0 = 2$ is the free electron Landé factor, and the z-component of the orbital angular momentum [71–74] is

$$L_n(\mathbf{k}) = \frac{2m_0}{\hbar^2} \sum_{m \neq n} \mathrm{Im}\left[\xi^{(x)}_{nm}(\mathbf{k})\xi^{(y)}_{mn}(\mathbf{k})\right](E_{n\mathbf{k}} - E_{m\mathbf{k}}). \tag{2.3}$$

In the summation, the index m runs over all bands excluding the band of interest, $\boldsymbol{\xi}_{nm}(\mathbf{k}) = i\langle u_{n\mathbf{k}}| \partial/\partial\mathbf{k} |u_{m\mathbf{k}}\rangle$ is the interband matrix element of the coordinate

operator, also known as Berry connection [75]. $E_{n\mathbf{k}}$ and $u_{n\mathbf{k}}$ are the energy and periodic Bloch amplitude of the electron in band n with wave vector $\mathbf{k}$. Using the energy band structure and interband matrix elements of the coordinate operator obtained from DFT we calculated the g-factors for interlayer excitons in Chapter 7.

2.2.3 Optical selection rules in heterobilayers from symmetry analysis

Optical transitions for $MoSe_2$-WSe_2 HBLs can be inferred from numerical calculations using DFT as already mentioned in Section 2.2.2, but at the cost of high time and computational power consumption. In contrast, optical selection rules at K points can also be deduced from symmetry analysis of the individual atomic registries. In the following a short summary of the resulting selection rules is given, a detailed derivation of the corresponding symmetries is presented in the Supplement of Reference [P2] and Appendix B. In a first step, the symmetry of the individual stacking has to be identified in order to describe the electron Bloch functions at K and K' with the corresponding irreducible representations Γ_n ($\mathrm{n} = 1, ..., 6$) given in the Koster notation [76]. Together with the spin parts, the Bloch amplitudes can be recast as spinor representations (Γ_4, Γ_5, Γ_6) for the VB of WSe_2 and the two spin-split $MoSe_2$ CBs. Finally, the optical transitions are derived using $\Gamma_c \times \Gamma_v^*$ with Γ_c (Γ_v) being the irreducible representation of the conduction (valence) band [77] (The star denotes the time-reversed representation of the corresponding symmetry group), leading to three possible transitions: σ^+, σ^- and z-polarized light. Figure 2.7 and Figure 2.8 summarize the spinor representations and optical selection rules for all atomic registries in H- and R-type stacked HBLs.

While the $\mathrm{K_W}$ ($\mathrm{K'_W}$) and $\mathrm{K_M}$ ($\mathrm{K'_M}$) valleys of WSe_2 VB and $MoSe_2$ CBs, respectively, are at the same position in reciprocal space for R-type stacked HBLs, the situation changes for H-type stacking due to the π-rotation of the $MoSe_2$ layer with respect to the WSe_2 layer. Brillouin zones are also rotated by π resulting in K and K' valleys residing on top each other. Zero-momentum interlayer excitons can be formed by an unoccupied VB state together with two possible CB states leading to bright $\mathrm{IX_B}$ and grey $\mathrm{IX_G}$ excitons with different energetic ordering in the two stackings resulting from the π rotation. In contrast to bright excitons, $\mathrm{IX_B}$, where the parallel spin configuration promotes radiative decay, grey excitons, $\mathrm{IX_G}$, have smaller oscillator strength due to the antiparallel aligned spins [78]. The observation of bright and grey exciton manifolds along with their optical recombinations allows to identify

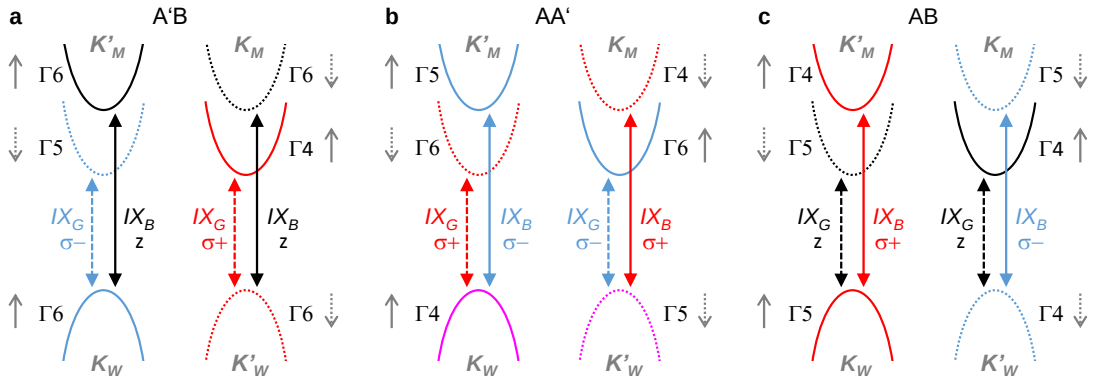

Figure 2.7: Band symmetries and optical selection rules for the case of H-type stacking. **a**, $MoSe_2$ CB and WSe_2 VB at K and K' forming the single-particle band diagram of a commensurate $MoSe_2$-WSe_2 HBL in A'B stacking including band symmetries (Γ_4, Γ_5 and Γ_6 are the spinor representations) and dipolar transitions with σ^+ (red), σ^- (blue) and z (black) polarization. **b** and **c**, Same for AA' and AB stacking, respectively. Solid (dotted) bands represent spin up (down) electron polarization; solid (dashed) arrows represent spin-allowed (spin-forbidden) optical transitions. The energy bands are colored according to the polarization of the respective optical transitions except for the bands in magenta supporting both σ^+ and σ^- transitions.

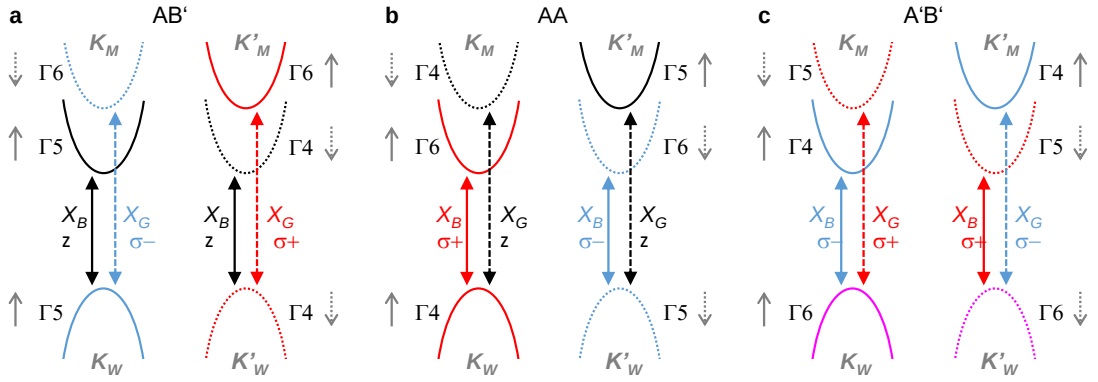

Figure 2.8: Band symmetries and optical selection rules for the case of R-type stacking. The three panels display the relevant properties for AB' (**a**), AA (**b**) and A'A' (**c**) stacking order. The pictorial representation of different spins and polarizations is similar to Figure 2.7

individual atomic registries in the experimental chapters.

2.2.4 Moiré effects in hexagonal systems

Introducing a twist angle between two commensurate hexagonal lattices leads to the formation of moiré superlattices with an infinite, but discrete distribution of possible rotation angles [79]. In case of incommensurate lattices, the formation of moiré

patterns is already present for aligned layers. The length $\mathrm{L_M}$ of the particular moiré supercell can be expressed as [80]

$$L_M(\theta) = \frac{a_1}{\sqrt{1 + \left(\frac{a_1}{a_2}\right)^2 - \frac{2a_1}{a_2}\cos(\theta)}}, \theta \in [-30°, 30°], \tag{2.4}$$

using the two lattice constants $\mathrm{a_1}$ and $\mathrm{a_2}$ as well as the corresponding twist angle θ. The whole range of twist angles can be accessed by a $60°$ rotation. Considering the two hexagonal lattices of $MoSe_2$ and WSe_2 in an aligned arrangement (i.e. $0°$ or $60°$) the small lattice mismatch [56] imposes an upper limit for $\mathrm{L_M}$ of 180 nm. Diffraction-limited confocal spectroscopy in the near infrared and visible spectral range therefore samples several moiré supercells in any unstrained exfoliation-stamped structure. Figure 2.9 shows a schematic illustration of a $MoSe_2$-WSe_2 HBL close to R-type arrangement with a $4°$ twist angle. The resulting structure features a moiré lattice with a periodic modulation of the three high symmetry atomic registries of R-type stacking. Depending on the magnitude of the twist angle the interplay of interlayer coupling and strain can lead to reconstruction effects with large areas of energetic favorable stackings separated by grain boundaries [81–83].

For small twist angles, the band structure of the corresponding heterostructures can be approximated by local bands stemming from the contributing atomic registries, which lead to a spatial modulation of interlayer exciton energies [78]. The excitons are confined in the potential minima of the moiré lattice resulting in a periodic arrangement of localized excitonic states. Recent experimental observations proved the existence of moiré excitons [84] for $MoSe_2$-WSe_2 HBLs [85, 86] as well as other TMD heterostructures [59, 87] and showed the emergence of correlated physical phenomena like Mott-insulating states in homo- [88, 89] and heterobilayer [32, 33] systems.

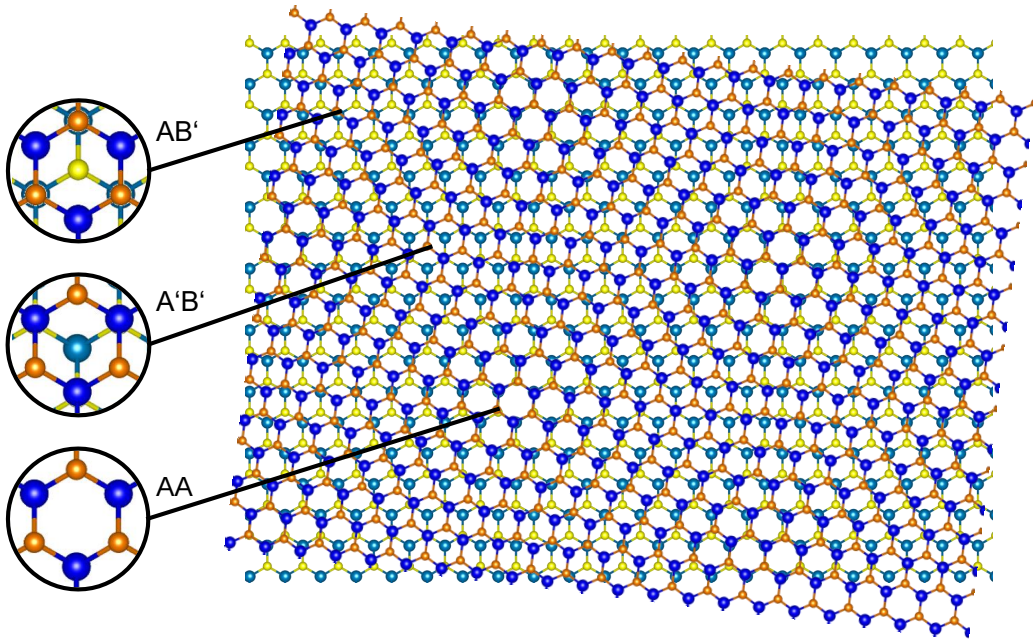

Figure 2.9: Schematic illustration of a moiré pattern within a twisted $MoSe_2$-WSe_2 HBL. Starting from an R-type arrangement the upper layer is twisted by 4° leading to a periodic modulation of the three atomic registries AA, A'B' and AB'. The color coding is similar to Figure 2.3.

Chapter 3

Fundamentals of optical resonators

This chapter gives a short introduction to optical resonators, listing their properties most relevant for this work. Starting point are two planar mirrors forming a stable resonator for a propagating plane wave. Quantities like Q-factor, finesse and transmission are discussed in this simple framework, before introducing fiber-based microcavities used for the experiments. A plane-concave resonator configuration leads to a lateral mode confinement for these systems and enables two-dimensional scanning capabilities. The derived formulas allow to calculate the lateral mode extent from the geometric properties of the fiber end-facet as well as the accurate mirror separation from a broadband transmission spectrum. In the last section, a two-level system is added to the cavity investigating the possible interaction with the resonator mode. In the regime of weak coupling, the Purcell factor is introduced and all contributing rates are expressed as a function of the cavity length.

3.1 General properties

More than 120 years ago, the potential of optical resonators was described by a pioneering work of Fabry & Perot [90]. Since then, a plethora of applications and phenomena have been studied using this simple principle of confining light between reflective surfaces. We give a short review on general properties of optical resonators following the textbooks by Saleh & Teich [91], Zinth & Zinth [92] and Hodgson & Weber [93].

Although optical resonators can be of different geometries, starting with two opposing mirrors is sufficient for a derivation of their main characteristic properties. Each mirror is characterized by its transmission ($\mathrm{T_i}$), reflection ($\mathrm{R_i}$) and loss ($\mathrm{L_i}$) coefficient ($i \in \{1, 2\}$) regarding the propagating field intensity. Here, the coefficients have to fulfill the condition $\mathrm{T_i} + \mathrm{R_i} + \mathrm{L_i} = 1$. A schematic drawing of such a simplified system is illustrated in Figure 3.1.

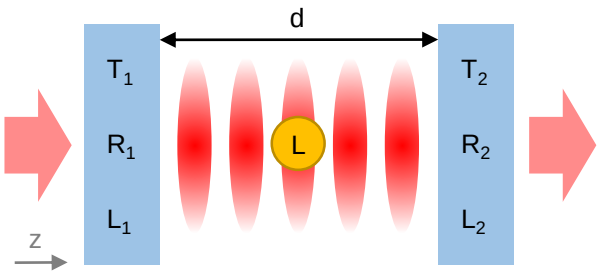

Figure 3.1: Schematic drawing of an optical cavity consisting of two opposing plane mirrors. Inside the resonator standing waves form dependent on the frequency of the circulating light and the mirror distance d. Both mirrors are characterized by their transmission ($\mathrm{T_i}$), reflection ($\mathrm{R_i}$) and loss ($\mathrm{L_i}$) coefficients. An additional particle can interact with the electomagnetic waves leading to the loss rate L.

In the next step, the system is assumed to interact with an incoming plane wave $E(z) = E_0 exp(iwt - ikz)$ with amplitude E_0 traveling along the cavity axis z. The confinement along the propagation direction imposes boundary conditions on the electromagnetic waves leading to the formation of standing waves with discrete frequencies:

$$\nu_q = q\frac{c}{2d}, \qquad q \in \mathbb{N}. \tag{3.1}$$

In this equation, d is the distance between the mirrors, c is the speed of light and q denotes the longitudinal mode number. The separation between two resonances in

frequency space is called free spectral range and can be written as

$$\Delta\nu = \frac{c}{2d}. \tag{3.2}$$

The individual resonances will also have a finite width depending on the accessible decay mechanism for the confined photons. Assuming an empty cavity ($L = 0$) leads to a total loss rate of $L_{tot} = T_1 + T_2 + L_1 + L_2$, which can be used to express the cavity decay rate as

$$\kappa = \frac{cL_{tot}}{4\pi d} = \frac{c}{2d\mathcal{F}}. \tag{3.3}$$

Here, $\mathcal{F}$ is the cavity finesse describing the number of round-trips for a photon inside the resonator. Using the above definitions the cavity finesse reads

$$\mathcal{F} = \frac{\Delta\nu}{\kappa} = \frac{2\pi}{L_{tot}}. \tag{3.4}$$

We find that the cavity finesse for an ideal system is independent of its length and is therefore in general a reliable number when comparing different length-tunable resonator systems. Nevertheless, details of real systems can lead to a length dependence of the finesse. For an elaborate description of such phenomena we refer to Reference [94]. Another important quantity of an optical resonator is the so called Q-factor:

$$Q = \frac{2\mathcal{F}d}{\lambda} = q\mathcal{F}. \tag{3.5}$$

Q is directly proportional to the cavity length and denotes the ratio of the stored energy to the energy losses per roundtrip.

So far, the system was assumed to be empty in order to describe the intrinsic properties of the resonator. Introducing a scatterer inside the resonator (see Figure 3.1) leads to a finite interaction of it with the circulating light field. The most simple interaction is a scattering or absorption process with the photon leaving the resonator mode. This finite loss can be introduced as $0 < L < 1$. Additionally, we assume the cavity to be on resonance in order to express the maximum transmission of the whole system as

$$T_{max} = \frac{T_1 T_2 (1 - L)}{(1 - \sqrt{R_1 R_2}(1 - L))^2}. \tag{3.6}$$

It might be interesting to note that for symmetric and loss-less cavities on resonance ($T_1 = T_2,\ L_1 = L_2 = L = 0$ and therefore $R_1 = R_2$) the maximum transmission becomes unity due to the constructive interference in forward direction and destructive interference in reflection.

For high finesse cavities, even small absorption and scattering losses can lead to a significant drop in the transmitted intensity, making them a powerful tool in detecting weakly interacting particles or transitions. More details on sensing and spectroscopy with cavities are presented in Reference [95].

3.2 Fiber-based Fabry-Pérot resonators

In the last section, the description focused on a system of two planar mirrors. The relevant systems throughout this work are microcavities using the end-facets of optical fibers. A reflective coating on the fiber tip makes it deployable as a mirror, forming a stable resonator when facing another mirror surface. The photons can be easily guided to the resonator via the optical fiber. Although the end-facet can have a planar geometry, imprinting a concave shape leads to the advantage of having a laterally confined mode and opens up two-dimensional scanning capabilities. A schematic drawing of such a system is depicted in Figure 3.2a. More details on fiber based cavities can be found in Reference [96]. The following section will give a general description of plane-concave cavity systems as can be found in References [91, 93]. Afterwards, relevant properties of fiber-based systems are introduced.

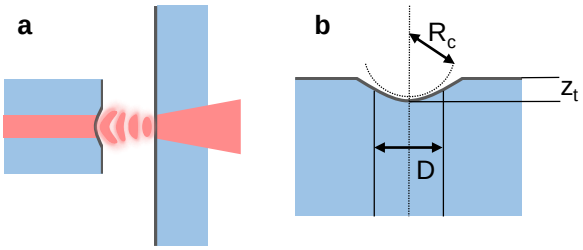

Figure 3.2: a, Schematic drawing of a fiber-based optical cavity. The concave shape imprinted in the fiber tip forms a stable resonator when opposing a planar mirror. The plane-concave configuration leads to a mode confinement perpendicular to the propagation direction. **b**, Schematic drawing of the optical fiber tip with a central depression displaying its important geometrical properties. D denotes the full width at $1/e$ of the Gaussian profile. The inner part can be approximated by a sphere with radius R_c. z_t is the depth of the imprinted depression.

Given a plane-concave cavity geometry, the wavefront of the stable resonator mode has to match the spherical mirror geometry. In the paraxial approximation, this condition is fulfilled by Gaussian beams. The free space intensity distribution I of a

Gaussian beam reads

$$I(x,y,z) = I_0 \left(\frac{W_0}{W(z)}\right)^2 exp\left(\frac{-2(x^2+y^2)}{W^2(z)}\right), \tag{3.7}$$

with $W(z)$ being the lateral intensity distribution also denoted as beam waist. It can be expressed the following way:

$$W(z) = W_0 \left(1 + \left(\frac{z}{z_0}\right)^2\right)^{1/2}. \tag{3.8}$$

Here, z_0 is the distance at which the beam wavefronts are most strongly curved. It is also known as Rayleigh range. $W(z)$ has a minimum at $z = 0$, which has a value of W_0 and lies, in our example, on the planar mirror surface (see Figure 3.2a). Therefore, this minimum mode waist influences the scanning capabilities of the cavity system by restricting the lateral resolution. In the following, the minimum mode waist is related to the geometric properties of the cavity fiber. In a first step, the radius of curvature (ROC) of the Gaussian beam wave fronts $R_g(z)$ can be related to the Rayleigh range z_0 as

$$R_g(z) = z + \frac{z_0^2}{z}. \tag{3.9}$$

Additionally, z_0 can also be expressed in relation to the minimum beam waist:

$$z_0 = \frac{\pi W_0^2}{\lambda}. \tag{3.10}$$

Here, λ is the wavelength of the resonator mode. In the case of the illustrated plane-concave resonator, the wave fronts have to match the curvature of the concave fiber tip R_c by fulfilling the condition $R_g(z = d) = R_c$. Therefore, the minimum mode waist can be expressed as

$$W_0 = \sqrt{\frac{\lambda d}{\pi}\sqrt{\frac{R_c}{d} - 1}}, \tag{3.11}$$

where R_c and d are the geometric properties of the cavity and λ is the wavelength of the light. For a high spatial resolution, small values of R_c are favorable. Simultaneously, R_c also defines the maximal stability range for a confined resonator mode ($d \leq R_c$). In experiments, high spatial resolution and length-tunability have to be balanced by an adaption of R_c.

Imprinting the depression into the fiber end-facet is done in a laser-machining process. Hereby, the imprinted shape is not perfectly spherical but has a Gaussian

shape (see Figure 3.2b). Nevertheless, it is possible to approximate the inner part with a sphere using the following relation:

$$z_t \approx \frac{D^2}{8R_c}. \tag{3.12}$$

This allows to calculate the ROC of the fiber tip R_c with the knowledge of its imprinted depth z_t and diameter D. In combination with a known wavelength λ this can be used to calculate the mode waist from the fiber geometry and the cavity length.

For microcavity experiments, the mirror separation is not a directly accessible quantity, but can be calculated from the spectrally resolved transmission of broadband in-coupled light. Such a transmission spectrum displays individual resonances separated by the free spectral range. Spectroscopic experiments in the visible and near infrared range usually refer to the wavelength of the corresponding light. Using Equation 3.2 and the relation between frequency and wavelength ($\nu = c/\lambda$) leads to the following equation:

$$d = \frac{\lambda_1 \lambda_2}{2\Delta\lambda}, \tag{3.13}$$

which enables a calculation of the actual cavity length from neighboring resonance wavelengths λ_1 and λ_2 of a transmission spectrum.

In addition to the above summary of the most relevant quantities, it might be important to note that higher order modes also solve the boundary condition of a plane-concave cavity system. While Laguerre-Gaussian modes would be the solution of a cylindrical symmetry, small imperfections in the imprinted depression impose a Cartesian symmetry. Therefore, typical experiments show Hermite-Gaussian higher order modes with resonant frequencies that are blue-shifted with respect to the TEM_{00} mode. For a more detailed description of higher order modes, their coupling, and the influence on the scanning capabilities we refer to References [94, 97, 98].

3.3 Cavity-emitter coupling

So far, the description of any particle inside the optical resonator focused on a pure dissipative system. This section will give a short review on the coupling of two-level systems to optical resonators. General descriptions of light-matter interactions in cavities can be found in textbooks from Loudon [99] or Scully & Zubairy [100]. Parts of this section will follow the derivation from Hinds [101]. If a two-level system is placed in an optical resonator, both components will decay with their individual rates (see Figure 3.3). As already mentioned, the cavity decays with a rate κ. The two-level

system can decay with a rate γ, but can also dephase with a rate γ^*. Finally, it is also possible to exchange excitations in a coherent way with a rate g. The derivations in this section concentrate on the regime of weak coupling, where the coherent coupling rate is smaller than all loss and dissipation pathways ($g < \kappa, \gamma, \gamma^*$).

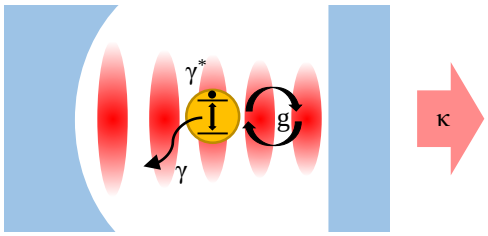

Figure 3.3: Schematic drawing of a plane-concave cavity configuration with a coupled two-level system. It is characterized by the decay rates of the individual components, i. e. κ and γ for the resonator and the two-level system, respectively. Additionally, the two-level system can dephase with a rate γ^* and coherently exchange excitations with a rate g.

Starting with a bare two-level system, one can compute its decay rate by using Fermi's golden rule:

$$\gamma = \frac{2\pi}{\hbar^2} \sum_k |\langle g, k \mid H_I \mid e, 0\rangle|^2 \delta(\omega_k - \omega_0), \tag{3.14}$$

with e and g being the excited and ground state, respectively. H_I describes the interaction of the emitting dipole with the electromagnetic field, $\hbar$ is the reduced Planck constant and ω_0 is the transition resonance. The interaction can be expressed as $H_I = \mu_{12} E$ with μ_{12} being the dipole matrix element. In free space this leads to the spontaneous decay rate

$$\gamma_{fs} = \frac{\mu_{12}^2 \omega_0^3}{3\pi\epsilon_0 \hbar c^3}, \tag{3.15}$$

with ϵ_0 being the vacuum permittivity. As mentioned for the first time in a theoretical work by Purcell [102], the decay rate of the transition can be influenced by the surrounding resonator. We assume a broad resonator compared to the intrinsic transition ($\kappa > \gamma$) and the emitting dipole placed at a field antinode in the maximum of the spatial mode function. In this case, the decay rate in the resonator is given by

$$\gamma_{cav} = \frac{2Q\mu_{12}^2}{\epsilon_0 \hbar V_m}. \tag{3.16}$$

Here, V_m denotes the effective mode volume of the resonator. Combining the two emission rates γ_{fs} and γ_{cav} leads to an expression for the emission enhancement into

the cavity mode given by

$$\frac{\gamma_{cav}}{\gamma_{fs}} = F_P = \frac{3}{4\pi^2}\frac{\lambda^3 Q}{V_m}, \tag{3.17}$$

with F_P being the Purcell factor. In the context of broad emitters, the quality factor is not solely dependent on the cavity parameters anymore, but can be expressed as $Q_{eff}^{-1} = Q_c^{-1} + Q_{em}^{-1}$, with Q_c and Q_{em} being the quality factors of cavity and emitter, respectively [103]. A quality factor for the emitter can be derived with the knowledge of the transition frequency ν and its linewidth $\delta\nu$: $Q_{em} = \nu/\delta\nu$.

In a real system, the emitting dipole can radiate into the cavity mode as well as into spatially non-confined modes. Therefore, the total decay rate of the system can be written as $\gamma_{tot} = \gamma_{fs} + \gamma_{cav} = \gamma_{fs}(1 + F_P)$. Dipole and cavity mode can also exchange an excitation in a coherent way with a rate g. This type of coupling is elaborated in the Jaynes-Cummings model with the coupling rate being [99, 104]:

$$g = \frac{\mu_{12}E}{\hbar} = \mu_{12}\sqrt{\frac{\omega_0}{2\hbar\epsilon_0 V_m}}. \tag{3.18}$$

In case of an ensemble of N equally coupling emitters the collective coupling rate can be expressed as $g_{tot} = \sqrt{N}g_s$ with g_s being the coupling rate of a single emitter [105, 106].

The family of layered 2D materials studied in the scope of this thesis can be modeled as quantum wells confining the excitonic transitions. Therefore, the individual decay rates can be simplified using the framework of a quantum well coupled to a two-dimensional cavity. According to Reference [107] the cavity decay rate can be expressed as

$$\kappa = 2 \cdot \frac{1-\sqrt{R}}{\sqrt{R}}\frac{c}{n_c d}, \tag{3.19}$$

using only material and cavity parameters like the mirror reflectivity R, the reflective index inside the cavity n_c and the cavity length d. Introducing an oscillator strength per unit area f, the coherent coupling rate g becomes [108, 109]

$$g = \left(\frac{\hbar^2}{4\pi\epsilon_0}\frac{2\pi e^2 f}{m d_{eff}}\right)^{1/2}, \tag{3.20}$$

with m being the electron mass and d_{eff} being the effective length of the resonator accounting for the refractive index inside the cavity. In this 2D framework, the coupled system becomes translationally invariant in the lateral dimensions, leading to the fact that instead of the mode volume V_m, only the cavity length d is relevant for the coupling. Since all material parameters are constant in the subsequent

experiments, tuning only the cavity length, it is reasonable to express decay rate and coupling strength in the following way:

$$\kappa(d) = \kappa_0 \cdot \frac{\lambda}{2d}, \tag{3.21}$$

$$g(d) = g_0 \cdot \sqrt{\frac{\lambda}{2d}}. \tag{3.22}$$

Here, κ_0 and g_0 are the cavity decay rate and the coupling rate at a mirror separation of $\lambda/2$, respectively. Following Reference [103], it is possible to derive a generalized form of the Purcell factor in the context of broad emitters:

$$F_p = \frac{4g^2/\gamma_{fs}}{\kappa + \gamma_{fs} + \gamma_d}. \tag{3.23}$$

Together with Equation 3.21 and Equation 3.22 the enhancement of the coupled system can be described as a function of the cavity length.

Chapter 4

Experimental methods

THIS CHAPTER IS PARTLY BASED ON THE PUBLICATION [P2]
Förg, M., Colombier, L., Patel, R. K., Lindlau, J., Mohite, A. D., Yamaguchi, H., Glazov, M. M., Hunger, D. & Högele, A. Cavity-control of interlayer excitons in van der Waals heterostructures. *Nature Communications* **10,** 3697 (2019)

Starting with the optical setup this chapter describes the experimental methods used in the scope of this thesis. Hyperspectroscopy was performed in a confocal microscope under ambient and cryogenic conditions. It was used to detect PL, DR as well as SHG features of the individual samples. Distinct modifications to the setup made it deployable for scanning-cavity operation in order to investigate the light-matter coupling of interlayer excitons.

The second part of this chapter focuses on two possible ways of sample preparation. The process of growth via CVD as well as the method of dry viscoelastic stamping are explained giving examples of fabricated samples.

4.1 Experimental setup

The samples were investigated with different optical methods. On the one hand, confocal microscopy is a powerful tool to obtain the intrinsic optical properties of the samples. The photonic environment is well-defined and is comparable to other free-space emitting samples. Modifications of the optical transitions can be introduced via external mechanisms like doping, electric or magnetic fields. On the other hand, an optical cavity can directly influence the radiative pathway and is therefore a complementary tool for testing the electro-optical properties. In the following, the experimental setups for both types of optical analysis are introduced.

4.1.1 Confocal cryogenic spectroscopy

Measurements were performed in a lab-built fiber-based confocal microscope operated in backscattering geometry (Figure 4.1). The system is similar to confocal systems used in References [P5] and [110]. Excitation was performed with different light sources ranging from broadband emitting sources for reflection measurements[1] to pulsed[2,3] and continuous wave[4] lasers for PL and SHG measurements. All excitation sources were coupled to an optical fiber making them easily connectable to the setup. A set of two linear polarizers (LPs) and wave plates (WPs) enabled full control over excitation and detection of polarization features in photoluminescence experiments. A variety of filters were used for the individual experiments. For typical PL experiments a shortpass filter in the excitation path was used to eliminate Raman-generated photons from the optical fiber. In the detection path a complementary longpass filter was mounted blocking the excitation laser. For SHG experiments, long- and shortpass filters were exchanged. The collected signal was coupled to an optical fiber and connected to the detection optics. In case of time-resolved measurements and SHG this was an avalanche photodiode (APD)[5] with a temporal resolution of 0.4 ns. For spectroscopy, the emitted light was dispersed by a monochromator[6] and recorded with a thermo-electric[7] or nitrogen-cooled[8] silicon charge-coupled device (CCD). The sample was mounted on piezo-stepping[9] and

[1] Ocean optics HL-2000-HP
[2] NKT Super K Varia and Super K Extreme
[3] Coherent Mira 900 pumped by a Verdi-V10 laser diode
[4] Helium Neon Laser LHRP-1701
[5] Excelitas SPCM-AQRH or PicoQuant τSPAD
[6] Princeton Instruments Acton SP 2500, SP2558, SP750i or SP300i
[7] Andor iDus 416
[8] Princeton Instruments PyLoN and Spec-10:100BR

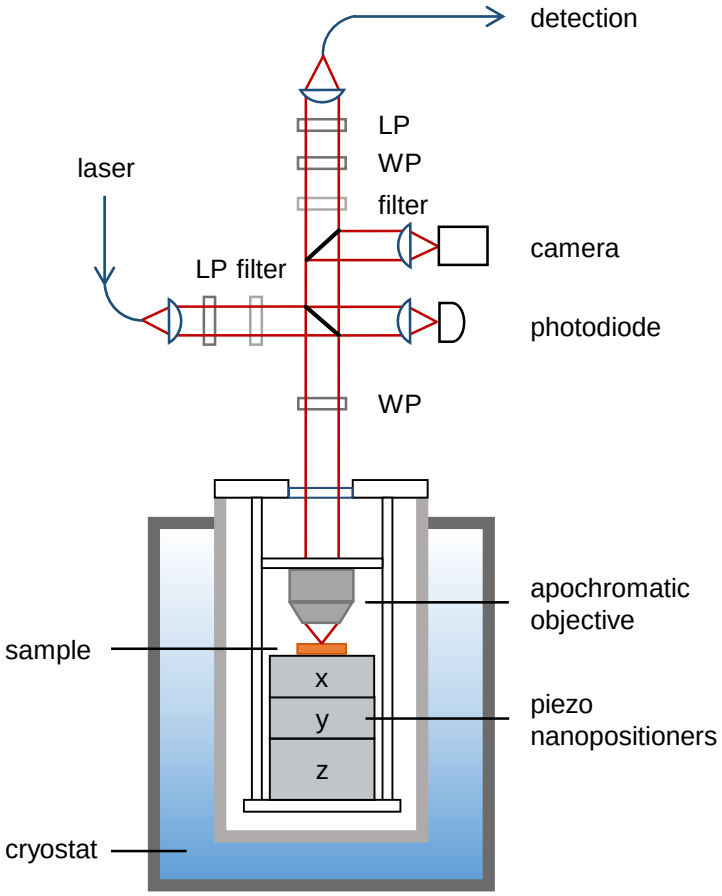

Figure 4.1: Optical setup for confocal microscopy. The fiber-coupled excitation laser was connected to the setup and passing a linear polarizer (LP) and a filter before it was partially reflected off a beam sampler. The reflected beam was guided towards the sample passing a wave plate (WP) and a focusing objective, whereas the transmitted beam is focused on a photodiode as feedback for laser stabilization. Backscattered laser light and signal were collected with the objective and coupled to the detection fiber. In between, a second beam sampler was partially reflecting the light onto a camera, which was used for orientation in an imaging configuration. A second set of optical components, consisting of filter, wave plate and linear polarizer, was used before coupling the light into the detection fiber. Positioning of the sample was accomplished via piezo nanopositioners. The whole microscope was immersed in a cryostat.

scanning units[10] for positioning with respect to a low-temperature objective[11]. The microscope was placed in a dewar with an inert helium atmosphere at a pressure of

[9] attocube systems ANPxy101 and ANPz102
[10] attocube systems ANSxy100/lr
[11] attocube systems LT-APO/NIR/0.81 or LT-APO/LWD/NIR/0.63

20 mbar and either immersed in a liquid helium cryostat at 4.2 K[12] or a closed-cycle dry cryostat at 3.1 K[13]. The closed-cycle system was additionally equipped with a superconducting solenoid allowing to apply magnetic fields up to 9 T in Faraday geometry.

4.1.2 Scanning cavity microscopy and spectroscopy

Modifications to the confocal setup allowed to operate in a scanning-cavity geometry. A detailed description of fiber-based optical resonators is presented in Reference [111], a comparable system to the following one, operated at room temperature, is employed in Reference [P6]. A schematic drawing of the modified system is shown in Figure 4.2a. The laser light was directly coupled to the cavity fiber leading to a simplified optical pathway. Since operation in an imaging mode was not possible in this configuration, the inspection camera is also removed from the system. The photodiode was used to monitor the transmitted laser light. Signal from the sample was spectrally filtered and guided to the same set of detection optics as in the confocal configuration. The apochromatic objective was replaced by an aspheric lens[14]. The cavity was composed of a fiber micro-mirror and a macroscopic sample mirror. A schematic drawing of the cavity part is shown in Figure 4.2b. Both components were silver (Ag)-coated with a protective layer of silicon dioxide (SiO_2). By design, the sample mirror had lower reflectivity to control the decay channel of the resonator and enhance the collection efficiency. The whole system was again placed in a dewar with inert helium atmosphere and immersed in a liquid helium cryostat at 4.2 K.

One central part of the cavity system was the laser-machined optical fiber end-facet. In order to increase the coupling of the sample dipole with the optical resonator small mode volumes are favorable. Therefore, it was crucial to reduce the cavity length down to a minimum. In order to reduce limitations on the minimal cavity length stemming from angular misalignment the lateral dimensions of the tip were decreased in a tapering process. Hereby, the planar end-facet of an optical single mode fiber[15] was processed in a home-built laser machining setup. In a second step, the central depression was imprinted in alignment with the fiber core. Finally, the structure was analyzed with a white light interferometer enabling a reconstruction of the height

[12] Cryo Industries SYS-2870-ATT
[13] attocube systems attodry 1000
[14] Thorlabs AL 1210-B
[15] Thorlabs S630-HP

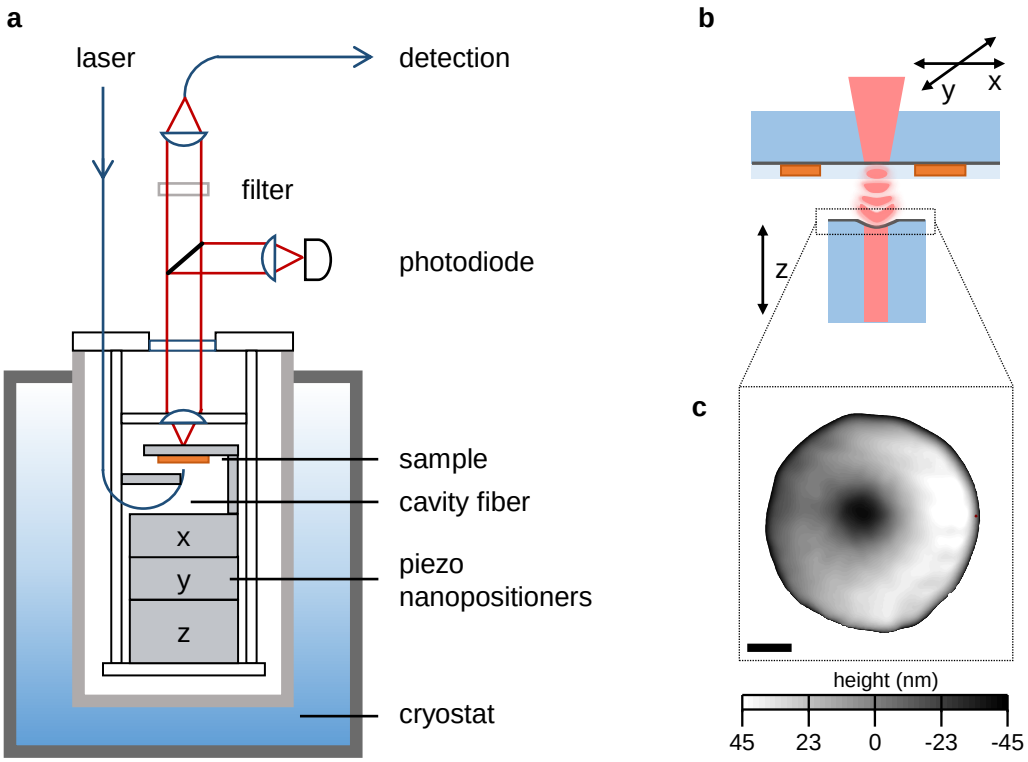

Figure 4.2: a, Schematic drawing of scanning-cavity setup. The excitation laser was directly coupled to the cavity fiber. Facing the fiber micro-mirror, the sample was mounted in an upside-down configuration. Transmitted laser light as well as signal were collected by a lens and guided towards the detection optics. In between, it was partially reflected and focused on a photodiode monitoring the transmission intensity. Before coupling into an optical fiber, a filter was blocking the excitation laser. **b**, Schematic drawing of the microcavity. Two translational degrees of freedom allow precise positioning of the desired sample position. Additional vertical translation enables to control the cavity length. A front view on the tapered and structured fiber tip is shown in **c**. The picture is a reconstruction from an white light interferometric image. The central depression of only several tens of nanometers in height was aligned with the fiber core and forms a stable cavity configuration when facing a planar mirror. Scalebar is 2 μm

profile with nanometer resolution. Such a reconstruction is shown in Figure 4.2c. The lateral extent was decreased to several micrometers, whereas the imprinted depression is only a few tens of nanometers in height. Defining the properties of the cavity mode in terms of mode waist and symmetry a detailed analysis of the profile is essential and is given in Chapter 6

In addition to the fiber geometry, the design of the macro-mirror also has an

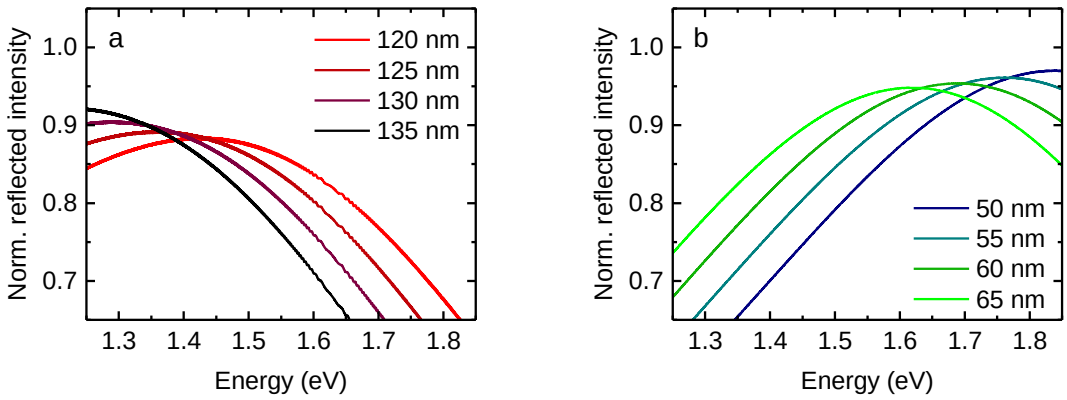

Figure 4.3: a, Simulation for a multilayer system of macroscopic suprasil, 30 nm Ag and SiO_2 with variable thickness. The simulation calculated the field intensity on the surface of SiO_2 as a function of photon energy and layer thickness. Aiming towards field enhancement for interlayer exciton emission layer thicknesses of 120 nm to 135 nm are displayed. **b**, Simulation for a multilayer system of macroscopic suprasil, 60 nm Ag, a variable SiO_2 layer and 30 nm hexagonal boron nitride (hBN). The simulation calculated the field intensity on the surface of hBN as a function of photon energy and SiO_2 layer thickness. In order to enhance the field intensity for intralayer excitons in the experiment, layer thicknesses of 50 nm to 65 nm are displayed.

extensive influence on the light-matter coupling. As already indicated by Figure 4.2b, photons inside a resonator form standing waves with nodes and anti-nodes of the corresponding electric field intensity. Since the light-matter interaction is dependent on the field intensity the emitting dipole has to be placed at a field anti-node. This was achieved by adjusting the spacer layer thickness above the reflective surface. Even in absence of a second mirror, the interference of incoming and reflected light can strongly modulate the intensity above a reflective surface. Thus, radiative lifetime of excitonic recombination can be controlled by simple changes in spacer layer thickness [112]. In order to have an adequate analysis of the field intensity, transfer matrix method simulations were performed. Within this analysis, plane waves propagate through a multilayer system described by characteristic matrices. More details on corresponding calculations can be found in Reference [113]. Simulated results were input parameters for designing the sample macro mirrors and are presented in Figure 4.3.

The intensity above the mirror surface was calculated as a function of photon energy and thickness of the SiO_2 spacer layer. Both simulations assume a

macroscopic suprasil substrate with a thickness of 2 mm. Figure 4.3a shows results for 30 nm Ag and a variable spacer layer of SiO_2. Trying to optimize the field intensity for interlayer exciton emission from around 1.25 eV up to 1.45 eV, different layer thicknesses are plotted. Based on this analysis, the sample presented in Chapter 5 had 30 nm Ag coating and a spacer layer of $\sim$ 125 nm SiO_2. Since encapsulation of TMDs into hBN improves the optical properties, Figure 4.3b shows simulated results for an additional layer of 30 nm hBN on top of the SiO_2 surface. The Ag layer thickness was set to 60 nm increasing the total reflected intensity. The field intensity was calculated on top of the hBN surface with a variable spacer of SiO_2 underneath. The design was optimized for an enhancement of intralayer exciton emission in the range from 1.6 eV up to 1.8 eV. The presented parameters for Ag and hBN thickness were used, together with a 60 nm spacer layer SiO_2, for the sample studied in Chapter 7. Changes of SiO_2-layer thickness on the order of several 5 nm have a large influence on the intensities within both examples highlighting the benefits of transfer matrix simulations when used for sample design.

4.2 Sample fabrication

The investigated samples were prepared with different methods leading to their individual advantages and drawbacks. One way of producing individual MLs and resulting heterostructures is to grow them via CVD. Facilitating a very fast and efficient production, CVD-growth is interesting for potential applications. The main drawback remains the sample quality which is still not competitive with exfoliated samples. Hereby, individual layers of the van der Waals crystal are detached from the bulk material using mechanical forces. This exfoliation technique allows precisely building TMD-stacks from scratch at the cost of a very high time consumption. In the following both methods are introduced in more detail.

4.2.1 Synthesis via chemical vapor deposition

The growth of TMDs via CVD features not only a high sample throughput and therefore a cost-efficient production, in the case of heterostructures it realizes inherently aligned layers with atomically sharp interfaces both in lateral and vertical geometries [114, 115]. Nevertheless, dissimilar lattice constants of incommensurate layers can lead to moiré effects [116–120]. The resulting physical phenomena are comparable to twisted HBL systems made via exfoliation stacking [121]. Unlike

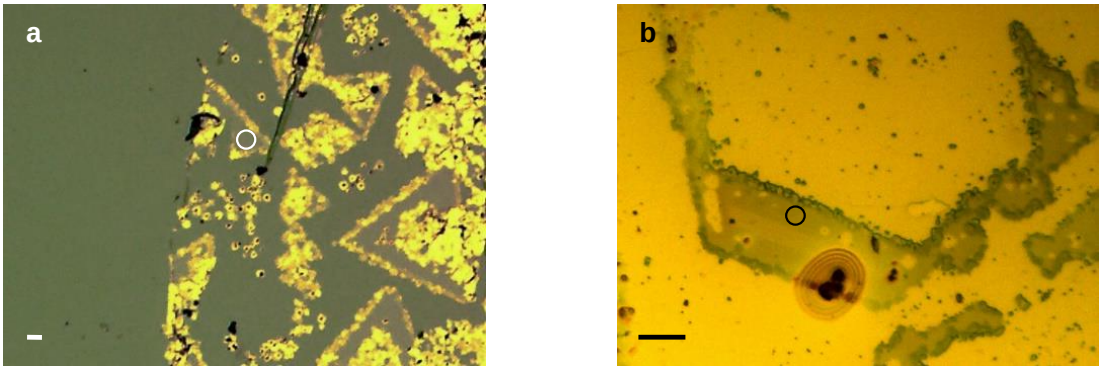

Figure 4.4: Optical images of CVD-grown vertical $MoSe_2$-WSe_2 heterostructures. The heterostructures were transferred onto a dielectric (**a**) or metallic (**b**) mirror leading to a different color scaling in the two images. The scale bar in both images is 20 μm. Typical heterostructure regions are present within the structures and are marked with a circle.

heterostructures of $MoSe_2$ and WS_2 where a lattice mismatch of a few percent features moiré patterns with a period of ~ 10 nm [118], structures made of $MoSe_2$ and WSe_2 can exist in moiré-free geometries [29, 30]. The small lattice mismatch of only 0.1 % can be accommodated by atomic vacancies to yield a fully commensurate HBL system in nearly ideal R- and H-type stacking geometries [56]. The following paragraph describes the method which was used to fabricate the moiré-free samples studied in Chapter 5 and Chapter 6.

In a first step $MoSe_2$ MLs were grown by selenization of molybdenum trioxide (MoO_3) powder. Therefore a CVD furnace was used. A substrate of SiO_2 on silicon (Si) along with a MoO_3 powder boat were placed at its center. It was heated to 750 °C in 15 min and held for 20 min. The substrate was facing down in close proximity to the MoO_3 powder. In a next step, selenium (Se) powder was vaporized at 200 °C, and a mixture of argon and hydrogen (15% hydrogen) at 50 SCCM was used as carrier gas leading to the growth of $MoSe_2$ MLs. The as-grown structure of $MoSe_2/SiO_2/Si$ was then transferred to a separate CVD setup for subsequent WSe_2 growth. The method was similar to the growth of $MoSe_2$. Specifically, the selenization of tungsten trioxide (WO_3) was performed at 900 °C in the presence of 100 SCCM carrier gas. The growth of WSe_2 occurs happen on top of $MoSe_2$ starting from its edges. Thereby, $MoSe_2$-WSe_2 vertical heterostructures were created. Due to thermal removal of possible physisorbed molecule gases on $MoSe_2$ during the transfer in air no additional treatment prior to WSe_2 growth was needed.

The as-grown heterostructures were transferred to the particular target substrate

using polymer-supported wet method. To this end polymethyl methacrylate (PMMA) was spin-coated on the structures and lifted off in 1M potassium hydroxide in water. The floating films with heterostructures were then deposited on the target substrate. Finally, the sample was rinsed in three cycles of water at room temperature to remove possible residues. Resulting heterostructures are shown in Figure 4.4.

Differences in size and shape of the structures stem from the individual growth process. The hexagonal lattice symmetry of the TMD MLs leads to growth in either triangular (Figure 4.4a) or hexagonal (Figure 4.4b) shaped structures. The lateral extent of CVD-grown heterostructures is in the range of several tens up to hundreds of micrometers. Although this outcompetes any exfoliation technique and makes CVD-growth interesting for applications like device fabrication, Figure 4.4 reveals also the inhomogeneity of grown samples. Bulk material is accumulated at the structural edges and residues of the growth process cover a large amount of the surface.

4.2.2 Exfoliation and dry viscoelastic stamping

The top-down approach for sample fabrication uses exfoliated MLs that are precisely arranged on a vertical stack via dry viscoelastic stamping. Starting with the first successful exfoliation of ML graphene [2], building samples from scratch has developed continuously, being a reliable source of high quality samples [9, 122]. Encapsulation of mono- and multilayer TMD structures in hBN has improved sample quality due to its passivating dielectric environment [53, 121, 123–125]. Finally, the possibility of twisting individual layers with respect to each other opened up a very rich field of moiré physics [59, 85–87, 116–120]. The method used to make the sample of Chapter 7 is taken from Reference [126] and described in the following paragraph.

In the first step, individual MLs of $MoSe_2$ and WSe_2 were exfoliated on Si substrates for the consecutive pick-up process. The same was done for multilayer systems of hBN which were used as encapsulation layers. Subsequently, polydimethylsiloxane (PDMS) and polypropylene carbonate (PPC) were deposited on a transparent glass slide serving as a stamp. The polymers are soft and adhesive layers with Van-der-Waals forces strong enough to overcome those between Si and hBN. Furthermore, the strength of the van der Waals forces can be adjusted with temperature. With a process of controlled heating and cooling, the individual components were then picked up. Within this work, the first one was a multilayer of hBN followed by a thin film of $MoSe_2$ featuring mono- and bilayer regions.

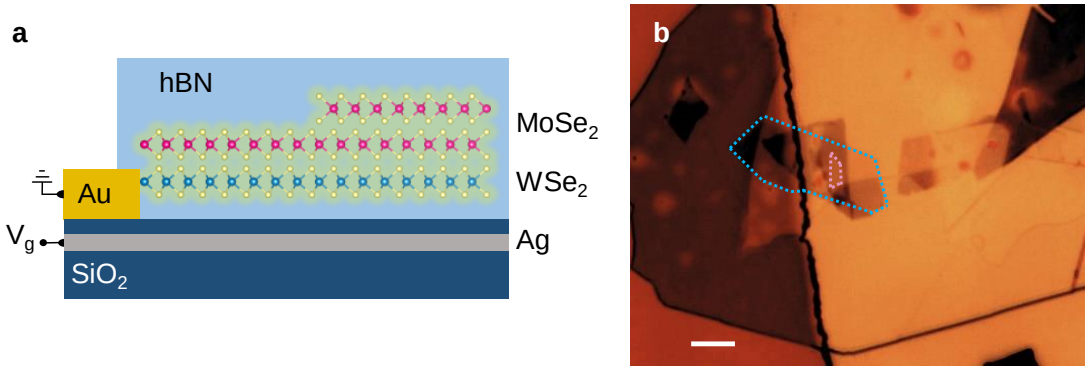

Figure 4.5: a, Schematic drawing of the sample made via dry viscoelastic stamping. **b**, Optical image of the sample. ML regions of $MoSe_2$ and WSe_2 contributing to the HBL are marked with light pink and blue dashed lines, respectively. The scale bar is 5 μm

Afterwards, a ML of WSe_2 was picked up and finally a multilayer of hBN. Each component was lifted by the previous one leading to clean interfaces on the heterostructure, which do not encounter any contact with polymers or wet chemistry. The whole stack can be released onto any desired target substrate. In this case, it was deposited onto a silver mirror with an additional gate structure. The ML of WSe_2 was in contact with a top gate of gold (Au). The Ag layer served as back gate. A schematic drawing of the assembled structure as well as an optical image are shown in Figure 4.5.

The target substrate was prepared via evaporation of Ag and SiO_2 onto a glass substrate. The gate structure was added via photolithography. It can be used to vary the charge carrier density in consecutive experiments. Figure 4.5b shows an optical image of the assembled structure. The gold structure is responsible for the dark color on the left side of the image. ML regions contributing to the HBL are marked with dashed lines. Since the mono- and bilayer regions of $MoSe_2$ are in direct vicinity the HBL is surrounded by a trilayer consisting of one layer of WSe_2 and a bilayer of $MoSe_2$. In this case, the lateral extent of the resulting HBL region is only 1.5 μm. Although the structures made by exfoliation stacking are more limited in their lateral extent, the introduction of a controlled twist angle between the two components can lead to new phenomena. Careful image analysis reveals that the individual layers are twisted by an angle of 4° with respect to each other. A distinction between 4° and 56° twist angle, and thereby a determination of the stacking (R-type or H-type, respectively), is only possible by analyzing the intensity of second harmonic generated photons. This type of analysis is shown in Chapter 7.

Chapter 5

Optical properties of as-grown $MoSe_2$-WSe_2 heterobilayers

THIS CHAPTER IS BASED ON THE PUBLICATION [P2]
Förg, M., Colombier, L., Patel, R. K., Lindlau, J., Mohite, A. D., Yamaguchi, H., Glazov, M. M., Hunger, D. & Högele, A. Cavity-control of interlayer excitons in van der Waals heterostructures. *Nature Communications* **10,** 3697 (2019)

The following chapter describes the results of spectroscopic studies on CVD-grown $MoSe_2$-WSe_2 HBLs. Beginning with an investigation of the second order susceptibility, spatially resolved detection of two-photon processes was employed to discriminate between H- and R-type registry. Subsequent measurements of cryogenic PL with variations in excitation power and wavelength revealed differences between intralayer and interlayer transitions and indicated a more complex transition mechanism for the interlayer exciton. An interpretation of the HBL PL is introduced supported by measurements of DR and polarization-resolved PL. The analysis of spectrally resolved exciton decay dynamics confirmed our assumptions on different interlayer exciton species. In a final step, the model was used to decompose the HBL PL, revealing a very self-consistent picture.

5.1 Introduction

The possibility of building functional devices by a combination of individual two-dimensional layers [10] promotes together with their valleytronic properties [17, 127, 128] the high level of interest in these promising material systems. Combining individual layers of $MoSe_2$ and WSe_2, both direct band gap semiconductors [41, 129], leads to a type II band alignment and thereby to the formation of interlayer excitons with electrons and holes residing in different layers [18]. These Coulomb-correlated electron-hole pairs give rise to a permanent exciton dipole moment along the stacking axis, and extended lifetimes up to several hundreds of nanoseconds [19–21, 26]. Such long lived bosonic systems inherit great potential for fundamental studies of dipolar gases with intriguing polarization dynamics upon expansion [24] and condensation phenomena [23].

In our studies, we employed continuous wave and time-resolved photoluminescence (TRPL) spectroscopy to reveal the intrinsic properties of CVD-grown $MoSe_2$-WSe_2 HBLs. Compensating the small lattice mismatch of $0.1\ \%$ by atomic vacancies, these heterostructures can exist in moiré-free compositions [29, 30] promoting nearly ideal R- and H-type stacking geometries [56]. Complemented by measurements of second harmonic generation and differential reflectance, we interpret our observations in the framework of interlayer excitons in various spin and valley configurations consistent with theoretical predictions of bright and dark excitons in commensurate HBLs. In addition, our measurements provide first insights on the oscillator strength of the individual transitions being a crucial element for subsequent coupling to optical resonators.

5.2 Second harmonic generation microscopy

In order to determine the stacking of the grown structure, second harmonic generation measurements were performed. This allows to discriminate between H- and R-type stacking geometries and reduces the number of possibilities down to three (actual geometries are illustrated in Figure 2.3). The second order susceptibility changes with the number of layers for naturally aligned multilayer systems in H-type registry [130]. Much more important, for a fixed layer number, the intensity of the detectable signal can be either lower (H-type) or higher (R-type) with respect to the ML making it possible to distinguish between the two possibilities [131].

For the measurement, the sample was illuminated with a picosecond pulsed laser at

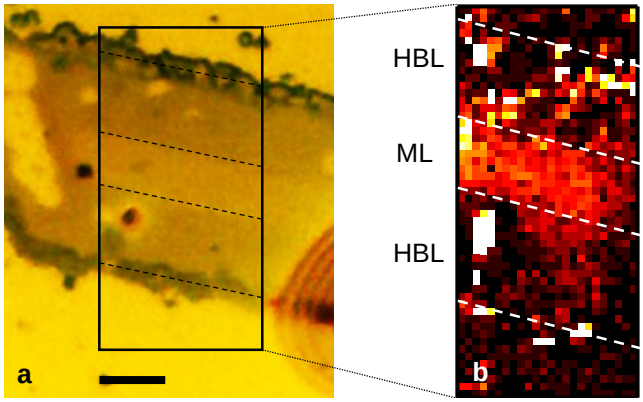

Figure 5.1: a, Optical image of a CVD grown $MoSe_2$-WSe_2 heterostructure, adapted from Figure 4.4b. The HBL regions at the structural edges have different absorption properties than the ML $MoSe_2$ in the interior part, enabling a distinction of both regions by their color and brightness. The scale bar is 10 μm. **b**, SHG raster-scan of the area indicated in **a**. Dashed lines in both images indicate structural edges as well as the intersections of HBL and ML regions.

a wavelength of 980 nm and a repetition rate of 78 MHz. The average laser power was 1.4 mW, focused to a diffraction limited spot size of the apochromatic corrected objective. The second harmonic generated photons at 490 nm were recorded with an avalanche photodiode. Lateral translation of the sample and simultaneous detection of the emitted signal enabled 2D SHG raster-scanning. Figure 5.1a,b show part of the sample and the corresponding SHG map, respectively.

Since the growth of the second layer is starting at the outer structural edges, a ML $MoSe_2$ might remain in the interior part. An example of such a structure is presented in Figure 5.1a. The interior part displays a change of image brightness, indicating the layer number difference. Figure 5.1b shows a spatially resolved SHG map sampling mono- and bilayer regions. The ML exhibits a higher signal intensity compared to the HBL identifying the grown structure to be in H-type registry. According to the analysis of Section 2.2.3, this type of stacking features energetically higher bright interlayer excitons $\mathrm{IX_B}$ and lower lying spin-forbidden transitions $\mathrm{IX_G}$. Subsequent measurements of PL and DR were analyzed regarding this energetic ordering.

5.3 Photoluminscence spectroscopy

Photoluminescence spectra of the CVD-grown structures were recorded at cryogenic temperatures of 4.2 K and an example spectrum is shown in Figure 5.2a. The $MoSe_2$

ML contributes a pair of peaks around 1.65 eV stemming from neutral and charged intralayer excitons [132]. Consistent with previous studies of exfoliation-stacked heterostructures [19, 20, 133, 134], the cryogenic PL shows vanishingly small emission from intralayer WSe_2 excitons and a strong low-energy peak of interlayer excitons around 1.40 eV. This HBL peak arises from photo-generated electrons and holes that relax over the CB and VB offsets of approximately 310 and 230 meV, respectively, to form interlayer excitons [19]. Efficient relaxation into interlayer exciton states results in the intense PL emission compared to the intralayer excitons. Therefore, interlayer excitons are an interesting candidate for coupling them to optical resonators.

Figure 5.2b shows spectral variations of the interlayer exciton emission at different sample positions. The topmost gray line is adapted from Figure 5.2a and serves as a reference. The second spectrum from top was recorded on the same flake in direct vicinity to the first one. Both positions lie within a spectrally homogenous area with a lateral extent of 100 μm^2. Moving to the structural edges results in a blueshift, shown in the third spectrum from top. The lowest lying spectrum stems from a different flake and is similarly blue-shifted. Subsequent measurements focused on the topmost spectrum stemming from an extended area of small spectral variations.

Another way of identifying the intrinsic properties of optical transitions is to probe their PL emission upon variations of the excitation power and wavelength. Figure 5.2c shows integrated PL intensities as a function of the excitation power for the $MoSe_2$ intralayer exciton, the interlayer exciton as well as a quantum dot feature. Interlayer excitons can be trapped in a local potential minimum due to disorder resulting in a narrow emission line observable only at a distinct position. The following description refers to such an emission feature energetically close to the interlayer exciton emission. While the PL intensity of the $MoSe_2$ intralayer exciton as well as the intensity of the interlayer exciton grow continuously with excitation power, quantum dot emission saturates at an excitation power of ~ 400 nW. Below this threshold quantum dot emission and intralayer exciton emission increase linearly with the excitation power due to the direct excitonic recombination. The slope of interlayer exciton emission is sublinear but does not saturate implying a different recombination mechanism for this optical transition. The blue shaded area indicates the range of excitation powers used for measurements throughout this Chapter as well as Chapter 6.

Photoluminescence excitation (PLE) spectroscopy is a powerful tool to reveal transition resonances within photoactive systems [135]. Hereby, PL emission is

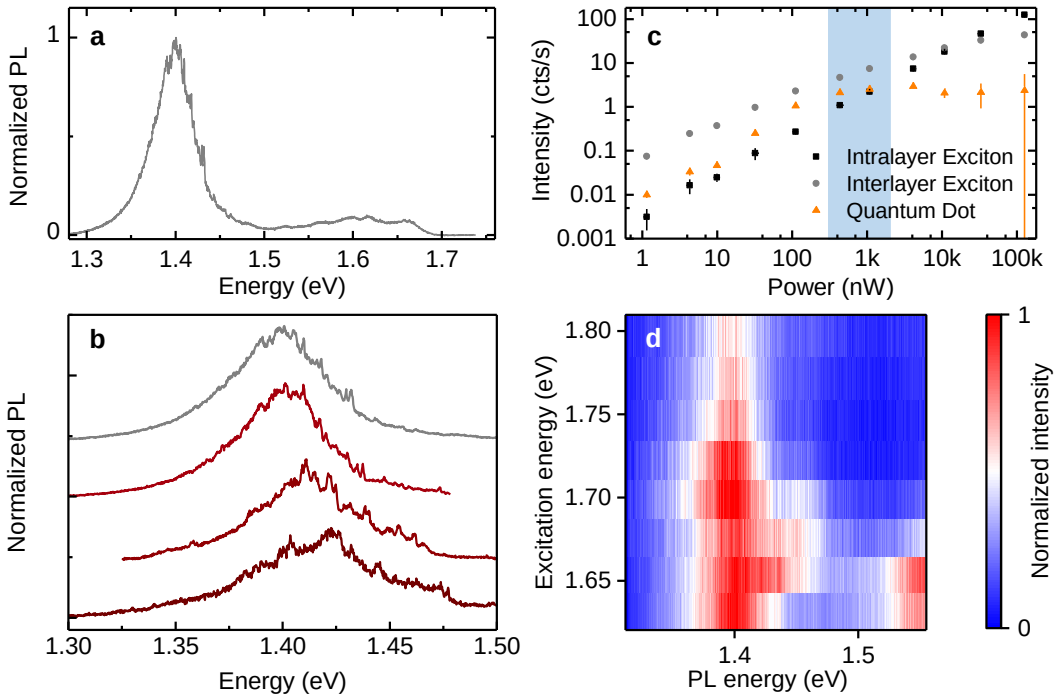

Figure 5.2: **a**, PL spectrum of CVD-grown $MoSe_2$-WSe_2 HBL recorded at 4.2 K with emission stemming from intra- and interlayer excitons at 1.65 eV and 1.4 eV, respectively. **b**, Spectral variations of interlayer exciton PL for different sample positions. **c**, Power dependent PL emission from the intra- and interlayer excitons as well as emission from a quantum dot. All three transitions show a different power dependence. **d**, Photoluminescence excitation spectroscopy of the interlayer exciton feature.

recorded for different excitation wavelengths. By direct comparison of the individual spectra in terms of intensity and shape, it is possible to denote excitation resonances of the system. An according PLE measurement for excitation energies ranging from 1.63 eV up to 1.80 eV is shown in Figure 5.2d. Excitation at intralayer exciton resonances of 1.72 eV for WSe_2 and 1.66 eV for $MoSe_2$ resulted in an enhancement of interlayer exciton PL at 1.4 eV. Apart from variations in the emission intensity we identify changes in the spectral shape. Emission at around 1.55 eV for low excitation energies stems from an enhanced red wing on the intralayer exciton emission due to the resonant excitation. Closer to the interlayer emission at 1.4 eV a small feature on the blue shoulder is observable when exciting resonantly. It can be attributed to emission from the higher lying bright interlayer exciton state $\mathrm{IX_B}$ enhanced by the resonant excitation. The resulting transition energy for $\mathrm{IX_B}$ is approximately 1.44 eV. However, contributions of Raman generated photons can change the spectral shape depending on the excitation energy. Since the overall contribution of Raman

processes to the PLE data set is unclear, we performed subsequent measurements to reveal the intrinsic excitonic properties.

5.4 Differential reflectance and degree of circular polarization

While intensities of PL spectra are a convolution of oscillator strength and exciton population, measurements of DR probe the direct radiative transition pathway. Therefore, DR spectroscopy is a complementary tool in identifying the zero-momentum radiation processes used for ML [136] as well as for HBL [137] TMDs. A corresponding DR spectrum of the investigated HBL is shown in Figure 5.3a. The DR spectrum at 1.65 and 1.75 eV is dominated by intralayer excitons in $MoSe_2$ and WSe_2, respectively. For low energies the absorption decreases. A zoom-in (Figure 5.3c) reveals a small but finite absorption on the high energy side of the interlayer exciton emission. Consistent with the energetic position of IX_B deduced from PLE spectroscopy in the previous section, the blue-shifted onset of interlayer absorption connotes that bright IX_B and grey IX_G interlayer excitons have only a minor contribution to the HBL PL. Their energetic positions are indicated in Figure 5.3c using values determined in Section 5.6.

Before giving an interpretation of the HBL emission, probing the valley photophysics is a crucial step for a discrimination between the stacking possibilities. This is usually done by PL polarimetry [138] with the degree of circular polarization defined as $P_C = (I_{Co} - I_{Cross})/(I_{Co} + I_{Cross})$ [110]. Here, the emission intensities are detected in co-polarized (I_{Co}) and cross-polarized (I_{Cross}) configurations using a circularly polarized excitation laser. Figure 5.3b displays P_C for the corresponding HBL. Starting with the intralayer transitions, WSe_2 displays a high degree of circular polarization [139], whereas intervalley scattering suppresses polarization conservation in $MoSe_2$ [140]. For interlayer excitons, P_C is zero or slightly negative above 1.44 eV , switching to a positive value for lower energies. In the context of a weakly contributing transition from IX_B competing with a high population in IX_G symmetry analysis qualifies the structure to be in AA' stacking [30] (see Figure 2.7b). The information collected from PL, DR and P_C measurements can now be interpreted and summarized in the following way:

We obtain from our symmetry analysis two optically active zero-momentum interlayer excitons. Bright excitons, IX_B, involve an unoccupied spin-up (spin-down)

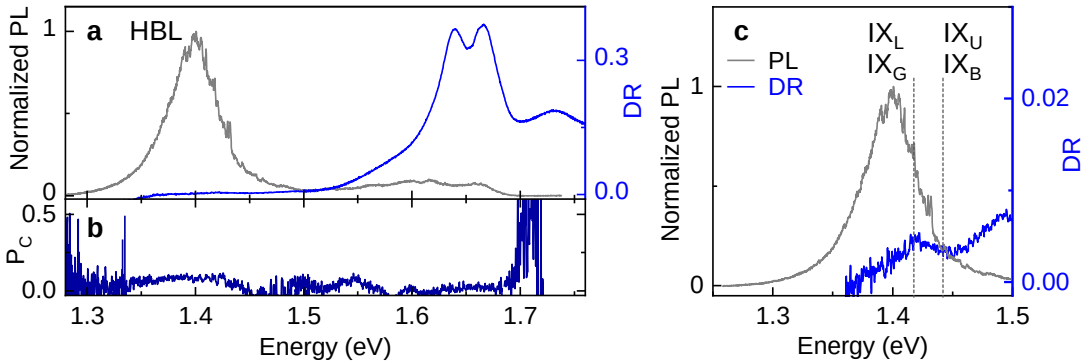

Figure 5.3: a, Cryogenic PL (grey) and DR (blue) spectra of a vertical $MoSe_2$-WSe_2 stack with dominant features of the HBL peak in emission and intralayer excitons in absorption. **b**, Degree of circular PL polarization, P_C, under circularly polarized excitation. **c**, Zoom-in to the intralayer exciton emission and absorption with energies of zero-momentum bright and grey excitons, IX_B and IX_G, and momentum-dark spin-like and spin-unlike excitons, IX_L and IX_U, indicated by dashed lines. The onset of absorption in the DR spectrum at $\sim$ 1.37 eV stems from the inhomogeneously broadened grey interlayer exciton state IX_G.

VB state in WSe_2 at K (K') and an occupied spin-up (spin-down) CB state in $MoSe_2$ at K' (K). The grey exciton manifold with a smaller oscillator strength due to its antiparallel spin configuration [78], IX_G, involves an unoccupied spin-up (spin-down) VB state in WSe_2 at K (K') and an occupied spin-down (spin-up) CB state in $MoSe_2$ at K' (K). These bright and grey exciton states, split by the CB spin-orbit splitting of $MoSe_2$ [25] and degenerate with their respective time-reversal counterparts, contribute through their corresponding radiative decay channels to the HBL peak in Figure 5.3.

In addition to zero-momentum interlayer excitons with dipolar-allowed optical transitions, finite-momentum interlayer excitons result from spin-like (IX_L) combinations of unoccupied spin-up (spin-down) VB states in WSe_2 at K (K') and occupied spin-up (spin-down) CB states in $MoSe_2$ at K (K'), as well as spin-unlike (IX_U) combinations of unoccupied spin-up (spin-down) VB states in WSe_2 at K (K') and occupied spin-down (spin-up) CB states in $MoSe_2$ at K (K'). These two doubly degenerate states IX_U and IX_L with non-zero center-of-mass momentum are resonant with IX_B and IX_G, respectively, yet void of direct radiative decay pathways due to momentum conservation constraints.

With this notion of interlayer excitons, we interpret the HBL peak in Figure 5.3 as arising from dipolar-allowed recombination of IX_B and IX_G excitons as well as from phonon-assisted emission from momentum-dark excitons IX_L. The IX_U

reservoir is assumed to be empty due to relaxation of the photoexcited population into energetically lower-lying states. Bright and grey excitons contribute zero phonon line (ZPL) emission at their bare energy. Momentum-indirect excitons, on the other hand, contribute to the PL spectrum as phonon sidebands downshifted from their bare energy $\mathrm{IX_L}$ by the energy of acoustic or optical phonons (and their higher order combinations) that compensate for momentum-mismatch in the light-matter coupling and thus promote radiative decay [P1, P5].

5.5 Exciton decay dynamics

To substantiate the interpretation of the HBL peak as a convolution of $\mathrm{IX_B}$ and $\mathrm{IX_G}$ ZPLs and $\mathrm{IX_L}$ phonon sidebands, we carried out TRPL experiments. Previous cryogenic studies of exfoliation-stacked $MoSe_2$-WSe_2 heterostructures reported interlayer exciton lifetimes in the range of $1-100$ ns with single- or multi-exponential decay dynamics [19, 20, 24, 133, 134]. The spectrally broad interlayer HBL peak of our sample exhibited similar PL decay characteristics. The best approximation to the total HBL peak was obtained with three exponential decay channels with lifetimes of ~ 6, 44 and 877 ns. A more detailed description of the fitting procedure is given in Section 6.5 on a large data set of cavity-assisted measurements confirming three exponential channels as best converging model. Consistent with our understanding of the HBL emission, the contributions of the individual decay channels to the total radiated PL energy varied significantly across the HBL peak. By performing PL decay measurements in narrow spectral windows at variable energies shown in Figure 5.4a, we found that the relative weight of the slowest decay component with 877 ns decay constant increased at the expense of the more rapid components with 6 and 44 ns lifetimes as the spectral band of the measurement window was shifted to lower energies (Figure 5.4b). In the red-most wing, interlayer PL was significantly delayed (note the prolonged rise-time of the PL traces in Figure 5.4a recorded in the red wing) and dominated by the longest decay constant.

The cross-over from short to long PL lifetimes upon progressive red-shift provides support for our interpretation of the HBL peak. Our model predicts a decrease for the PL contribution from the momentum-bright exciton $\mathrm{IX_B}$ upon increasing red-shift from its ZPL, and this trend is consistently supported by the data in the upper panel of Figure 5.4b. In this framework, the shortest decay channel is attributed to bright excitons $\mathrm{IX_B}$ (data in the upper panel of Figure 5.4b), the intermediate

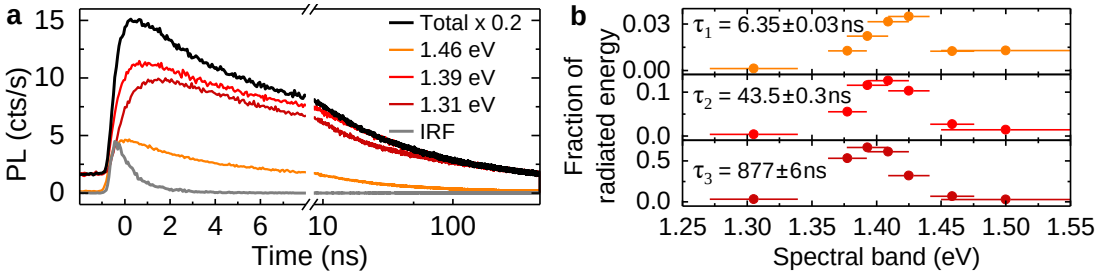

Figure 5.4: a, Confocal PL decay measured in different spectral bands of the HBL peak in Figure 5.2. Decay traces are shown in different colors for three spectral bands centered at 1.46, 1.39 and 1.31 eV together with the total decay trace in black (scaled by $\times$ 0.2) and the instrument response function (IRF) in grey. The decay of the total spectrally unfiltered PL was approximated best by three exponential decay channels with time constants of $\sim$ 6, 44 and 877 ns. **b**, Relative contributions of the three decay channels in discrete spectral windows with central energies and widths represented by dots and bars, respectively. For each spectral window, the contributions were extracted from triple-exponential fits with decay constants fixed to the characteristic timescales of the total HBL emission.

timescale to grey excitons IX_G (central panel of Figure 5.4b), and the long lifetime to phonon-assisted decay channels at larger red-shifts (lower panel of Figure 5.4b). Alternatively, one could assign the fast and intermediate decay components to IX_B and IX_G decay channels, respectively, and the long decay component to defect-localized interlayer excitons trapped in disorder potentials. Within this notion of disorder-assisted emission, the main emission intensity would be related to defects, showing no saturation behavior within the measured excitation power range (Figure 5.2c). Therefore, we interpret phonon-assisted decay to be the dominating and most likely process, however, not discarding contributions from defect-localized emission.

5.6 Spectral decomposition of interlayer exciton photoluminescence

Our interpretation of HBL emission as ZPLs stemming from IX_B, IX_G and phonon sidebands can be underpinned by spectrally decomposing the PL peak into these individual components. To model the total PL spectrum, we follow the procedure introduced for MLs [P1] and homobilayer [P5]. On the blue side of the HBL PL peak in the spectral range of $1.30 - 1.45$ eV, bright and gray excitons contribute with their

respective ZPL emission. The red side of the peak is composed of phonon sidebands of momentum-dark $\mathrm{IX_L}$ excitons that decay with the assistance of acoustic, optical and higher-order phonon processes [P1, P5].

In order to simplify the analysis and reduce the number of relevant phonon modes, we employ the hole valley locking approximation [141–143] where the intervalley scattering of VB states is neglected and only CB scattering is considered. In this approximation, phonon-assisted radiative decay processes involve electron scattering with $MoSe_2$ phonons. The energies of optical and acoustic phonons with Γ-momentum and K-momentum in ML $MoSe_2$ were adapted from [43] and are displayed in Table 2.1. In our sample, inhomogeneous broadening with a full-width at half-maximum (FWHM) of about 50 meV dominates the PL linewidth and therefore the ZPLs of $\mathrm{IX_B}$ and $\mathrm{IX_G}$ exciton transitions as well as the phonon sidebands of $\mathrm{IX_L}$ and $\mathrm{IX_U}$ states were modeled by Gaussians. Due to large inhomogeneous broadening, we neglect the expected deviations of ± 2 meV for $MoSe_2$ phonon energies in $MoSe_2$-WSe_2 HBLs. Moreover, since the energy differences between longitudinal optical (LO) and transverse optical (TO) as well as longitudinal acoustic (LA) and transverse acoustic (TA) phonons are negligible on the scale of the inhomogeneous broadening, we use in our decomposition analysis only one energy for acoustic phonons (18.3 meV) and one for optical phonons (32.8 meV) obtained as averages of LA and TA mode energies and LO, TO and A_1 mode energies, respectively.

With these simplifications, we decompose the HBL peak in a best-fit procedure into individual contributions of $\mathrm{IX_B}$ and $\mathrm{IX_G}$ ZPLs and phonon sidebands of $\mathrm{IX_L}$ momentum-dark excitons. The results of two different fitting procedures are shown in the left and right panels of Figure 5.5. In both approaches, we used a linear function to fit the background on the high energy side of the PL spectrum and allowed the fit procedure to determine the energy of $\mathrm{IX_B}$ as well as the amplitudes of Gaussians representing ZPLs of $\mathrm{IX_B}$ and $\mathrm{IX_G}$ and phonon sidebands of $\mathrm{IX_L}$ with a joint FWHM inhomogeneous linewidth. In the first approach, we impose no constraints on the Gaussian amplitudes and perform best-fit decomposition with first order phonon processes only. The resulting best fit is presented in Figure 5.5a. The fit yields a predominant contribution of $\mathrm{IX_G}$ (red solid line) to the total HBL peak which decreases when we take into account second order processes as shown in Figure 5.5b. The contribution of $\mathrm{IX_L}$ phonon sidebands to the spectrum (brown solid line) in turn increases at the expense of $\mathrm{IX_G}$ ZPL in qualitative agreement with our TRPL data shown in section 5.5.

In the second approach, a quantitative agreement with TRPL data in Figure 5.4 can

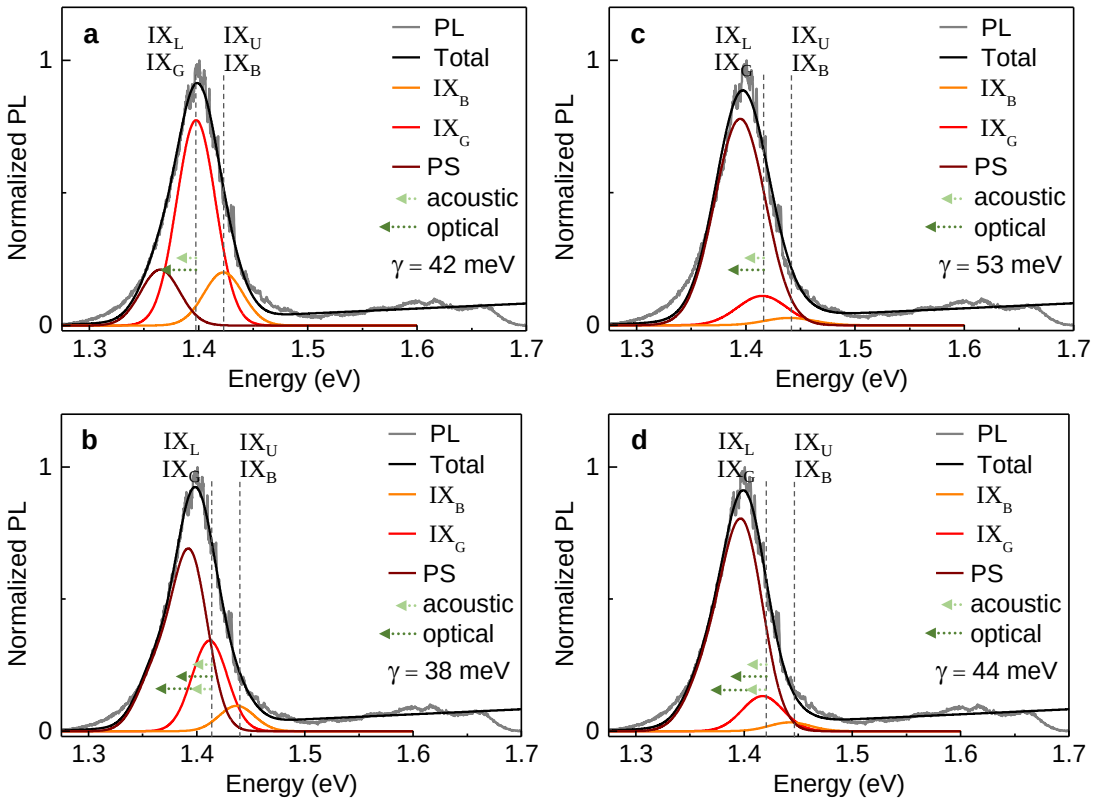

Figure 5.5: Photoluminescence spectrum of $MoSe_2$-WSe_2 interlayer excitons (gray) with best fit (black solid line). Individual fit contributions zero-phonon lines of bright IX_B and gray IX_G excitons are shown as solid orange and red lines, respectively, and the sum of phonon sidebands of momentum-dark excitons IX_L are shown in brown. The reservoir of momentum-dark excitons IX_U is assumed to be void of population and thus does not contribute to the spectrum. First order acoustic and optical phonon processes are represented by light green and green arrows. **a**, Resulting fit with an un-constraint model and first order phonon processes. **b**, Same for first and second order phonon processes. **c**, Resulting fit with a constraint model and first order phonon processes. **d**, Same for first and second order phonon processes.

be established by constraining the amplitudes of IX_B and IX_G, as shown in the right panel of Figure 5.5. Using the fractions of the radiative energy from Figure 5.4, we decompose the PL spectrum with first order (Figure 5.5c) and second order (Figure 5.5d) phonon processes. Note that both approaches yield similar energies for IX_B and IX_G excitons at ~ 1.440 eV and 1.415 eV, respectively, and the FWHM linewidths are in good agreement with the inhomogeneous broadening of 55 meV determined from Figure 5.4. These energies are used in Figure 5.3c to indicate the energetic positions of IX_B and IX_G. More important, for these constrained

approaches $\mathrm{IX_B}$ emission becomes the dominant contribution for energies above 1.44 eV, matching the change of polarization in Figure 5.3b. The presented model results in a self-consistent picture of the investigated HBL emission.

5.7 Conclusion

In summary, we identified the presented HBL to be in AA' stacking according to SHG mapping and polarization-resolved measurements. Based on measurements of PL and DR we introduced a model to interpret the observed interlayer emission as a convolution of the ZPLs of bright $\mathrm{IX_B}$ and grey $\mathrm{IX_G}$ interlayer excitons as well as phonon-assisted processes. Time-resolved PL supports this interpretation and simultaneously provides decay times for the three contributing transition pathways. Finally, a spectral deconvolution was performed revealing the contributions of the individual channels to the total HBL emission. The detected absorption properties and decay time scales quantify the free space emission rate of interlayer excitons, which proves to be useful for analyzing the coupling rate to optical resonators in Chapter 6.

Chapter 6

Coupling of $MoSe_2$-WSe_2 heterobilayers to optical resonators

THIS CHAPTER IS BASED ON THE PUBLICATION [P2]
Förg, M., Colombier, L., Patel, R. K., Lindlau, J., Mohite, A. D., Yamaguchi, H., Glazov, M. M., Hunger, D. & Högele, A. Cavity-control of interlayer excitons in van der Waals heterostructures. *Nature Communications* **10,** 3697 (2019)

Based on the preceding confocal studies of CVD-grown $MoSe_2$-WSe_2 HBL systems, this chapter focuses on the interaction of interlayer excitons with an optical microcavity. Starting with a basic characterization of our cryogenic cavity system, relevant parameters are summarized. 2D scanning capabilities were employed to allocate the resonator mode at the same positions as studied in the previous chapter. Before demonstrating cavity control of the HBL peak PL dynamics, decay traces were analyzed regarding the minimal number of contributing channels. Subsequently, we investigate the Purcell enhancement of the coupled system stating absolute numbers for light-matter interaction of the individual interlayer exciton decay mechanisms. In the last section, the potential of cavity-enhanced absorption microscopy is illustrated by applying a highly reflective scanning cavity system.

6.1 Introduction

ML TMDs integrated in optical microcavities host exciton-polaritons as a hallmark of the strong light-matter coupling regime [34–38]. While this limit of new bosonic eigenstates of half-matter and half-light quasiparticles is routinely achieved for ML systems, cavity-control of van der Waals heterostructures has been elusive so far. Analogous concepts for hybrid light-matter systems employing spatially indirect excitons with a permanent electric dipole moment in HBL crystals promise realizations of exciton-polariton gases and condensates with inherent dipolar interactions. While their extended lifetimes [19, 20, 133, 134] are beneficial for providing sufficient time scales for thermalization, finite exciton dipole moments ensure mutual interactions in exciton-polaritons gases and condensates. In the following, we coupled $MoSe_2$-WSe_2 HBL crystals to a tunable micro-cavity system enabling two-dimensional scanning capabilities along with Purcell enhancement of the corresponding interlayer exciton PL. A detailed analysis of the decay dynamics allowed us to extract the light-matter interaction strength for the individual contributing channels. The study of this coherent exchange process is complemented by highly sensitive measurements of interlayer exciton absorption in a dedicated cavity system.

6.2 Cavity characterization

Before introducing an interaction between the light field inside an optical resonator and the previously discussed interlayer excitons, it is instructive to characterize the bare cavity system composed of a fiber micro-mirror and a macroscopic mirror. This section describes the properties of the cryogenic microcavity which is shown in Figure 4.2 and is used for 2D scanning (Section 6.3) and emission enhancement (Section 6.5) of the interlayer excitons studied in Chapter 5. Section 6.6 describes a different cavity system operated at room temperature. A short summary of its important quantities is given along with the measurements.

The macro-mirror of the cryogenic system was coated with ~ 30 nm of silver and a spacer layer of SiO_2 with thickness designed to place the HBL at a field antinode (for details see Figure 4.3). The effective radius of curvature of the central depression in the laser-machined fiber end facet was 136 μm, as deduced from white light interferometric measurements of the fiber tip. According to Equation 3.11 this radius defines the geometrical properties of the cavity mode and thereby imposes restrictions

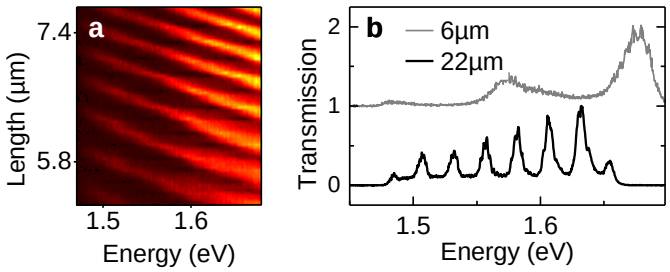

Figure 6.1: Transmission characteristics of the cavity. **a**, Heatmap of the cavity transmission as a function of the cavity length. **b**, Transmission spectrum for a cavity length of 6 μm and 22 μm, offset for clarity.

on the lateral resolution of 2D scans. The facet was coated with ~ 50 nm silver and a protection layer of SiO_2. Three translational degrees of freedom of the sample on the mirror were accessible by cryogenic positioners to provide both lateral scans and coarse-tuning of the cavity length. Cavity fine-tuning was achieved by displacing the fiber-mirror with an additional piezo. Transmission characteristics of the bare cavity (i.e. off $MoSe_2$-WSe_2 flakes) as a function of cavity length, shown in Figure 6.1, were recorded with a supercontinuum laser. The cavity length was calibrated by using the transmission maxima and Equation 3.13 to calculate the distance between the two mirrors.

Figure 6.1a displays the possibility of continuously changing the cavity length in order to bring the cavity system in resonance with the transition of interest. The envelope of the broadband excitation laser leads to a more intense signal for higher energies. In Figure 6.1b transmission spectra for 6 μm and 22 μm are displayed. The reduced free spectral range for a high mirror separation is beneficial for scanning applications of the spectrally broad interlayer exciton emission.

Additionally, the transmission spectra allow to extract the FWHM linewidth of the system as a function of the cavity length. Using Equation 3.19 and the determined values of the decay rate κ we infer a reflectivity coefficient of $R = 0.87$. This matches the expected behavior calculated from the deposited Ag layer thickness. In the simplified framework of Equation 3.21 we obtain a value of $\kappa_0 = 410$ meV for the decay rate at a mirror separation of $\lambda/2$. Equipped with a calibrated cavity length, it is possible to deploy the system for 2D scanning applications. Furthermore, the extracted decay rate can be used to model the decay dynamics of the interlayer excitons in the subsequent experiments.

6.3 Scanning cavity imaging

As already mentioned in Section 4.1.2, lateral displacement of the sample mirror enabled 2D positioning and profiling of the sample. For PL spectroscopy, excitation by a supercontinuum laser at 635 nm was provided via the optical fiber and both transmission and PL were detected through the planar macro-mirror with the heterostructures on top. Using Equation 3.11, we calculate the expected mode waist of the resonator for the excitation laser (W_{ex}) and of the detected PL emission at 880 nm (W_{PL}) as a function of the cavity length. The calculated dependencies are plotted in Figure 6.2a. 2D scans were performed with a cavity length of ~ 22 μm resulting in mode-waists of 3.2 μm and 3.7 μm for W_{ex} and W_{PL}, respectively. The corresponding cryogenic cavity transmission and PL maps of the HBL flake with confocal PL data in Figure 5.3 and Figure 5.4 are shown in Figure 6.2b, c.

The transmission map in Figure 6.2b, recorded with the excitation laser at 635 nm, quantifies both absorption and scattering inside the cavity. The sizeable ML absorption in the range of several percent [136] facilitated the detection of individual MLs and HBLs via the cavity transmission. Scattering contrast at structural defects such as edges or transfer-related cracks provided additional guides to the identification of individual flakes. Sharp edges were also useful to estimate the actual mode waist of the scanning cavity system from the recorded 2D transmission maps. A line-scan, when passing a structural edge, is a convolution of the mode waist and an ideally step-like change in transmission. Therefore, the first derivative of the corresponding data has a Gaussian profile with the equivalent waist. An average of the extracted values is shown in Figure 6.2a as light blue data point. The experimentally measured waist W_m of 3.3 ± 0.8 μm, is in agreement with the theoretically predicted waist of the excitation light W_{ex} . The error bar of W_m stems from limitations in the positioner accuracy as well as discrepancies between an ideal step-like function and the actual sample edges.

Compared to diffraction limited spot sizes achievable in confocal spectroscopy the measured spatial resolution is not competitive. The performance can be improved by using smaller mirror separations during the scans as well as a smaller ROC imprinted in the fiber. A smaller ROC, however, limits the maximal stable resonator length. Spatially resolved transmission of higher order modes can even lead to a diffraction limited mode waists for scanning cavity systems [97]. Since the lateral extent of the grown heterostructures far exceeds the measured mode waist, the presented lateral resolution is not a limiting factor for scanning and positioning.

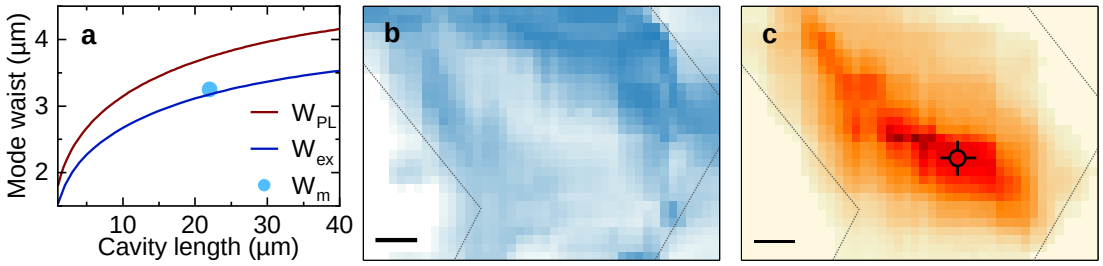

Figure 6.2: a, Calculated mode waist for excitation light (W_{ex}) and detected PL signal (W_{PL}) as a function of cavity length. The blue dot indicates the measured mode waist (W_m) extracted from the transmission map shown in **b**. **b**, Transmission map recorded through the cavity with laser excitation at 635 nm (blue color corresponds to reduced transmission due to local variations in absorption and scattering). **c**, Map of integrated PL intensity recorded simultaneously with the transmission map (dark red color represents maximum intensity). The cross indicates the position on the flake used in the measurements of Figure 5.3 and Figure 6.4, the grey dashed lines indicate the boundaries of the flake. The scale bar is 10 μm in both maps.

Equipped with the combined scanning capabilities and the data from transmission, it was straight forward to position the cavity to any point of interest on the HBL flake. In addition, by recording PL spectra at each raster scan-point of the cavity simultaneously with the transmission, PL intensity maps were obtained within the spectral band of interest, as shown for the interlayer exciton PL map of Figure 6.2c. By monitoring both transmission and PL, we positioned the cavity on the spot indicated by the cross in Figure 6.2c where the data of Figure 5.3 and Figure 5.4 were recorded with confocal spectroscopy, and performed PL decay measurements as a function of the cavity length. The following sections focus on the analysis of these time-resolved measurements.

6.4 Temporal analysis of exciton decay dynamics

Starting with the analysis of TRPL measurements from the cavity system, Figure 6.3a displays typical decay dynamics at a representative cavity length of 30 μm. These PL decay traces were recorded with an APD and modeled as a summation of the instrument response function and multi-exponential decay functions as follows:

$$I(t) = I_0 + A_0 \cdot e^{-2\cdot[(t-t_0)/w]^2} + \sum_{k=1}^{N} A_k \cdot e^{(-t/\tau_k)}, \tag{6.1}$$

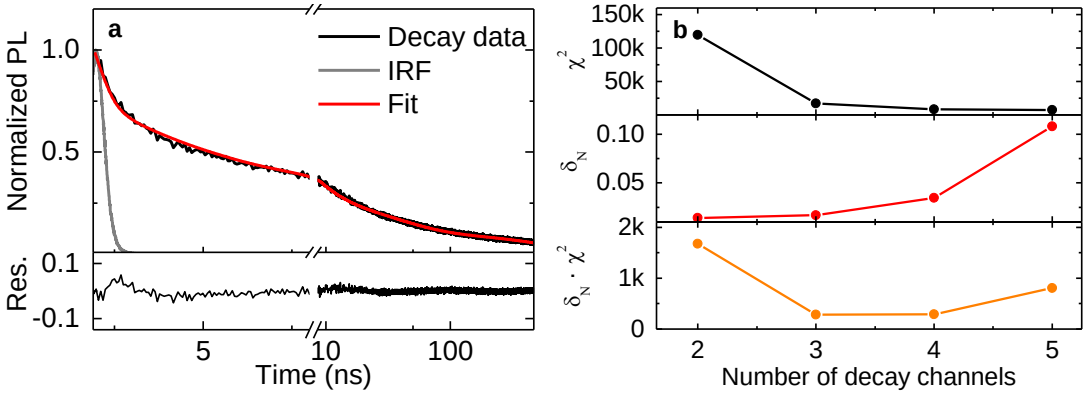

Figure 6.3: a, Upper panel: Normalized time-correlated PL decay at a cavity length of 30 μm (black), experimental APD instrument response function (IRF) measured with a picosecond-pulsed laser (gray), and model fit with three exponential decay channels (red solid line with $\tau_1 = 4.3$ ns, $\tau_2 = 33$ ns, $\tau_3 = 660$ ns). Lower panel: Residuum of the fit. **b**, Upper panel: Best-fit χ^2 average, obtained by averaging χ^2 values of multi-channel best-fits for all measurements at variable cavity lengths, as a function of the number of decay channels. Middle panel: Averaged and normalized parameter errors δ_N for the corresponding data. Lower panel: Product $\delta_N \cdot \chi^2$ of both error types. The minimum of the product at $N = 3$ indicates that three decay channels are best suited to approximate the multi-channel decay characteristics of the HBL peak in Figure 5.2a.

where the first term I_0 quantifies the APD dark counts, the second term is the APD instrument response approximated by a Gaussian with the temporal resolution w, and the third is the sum of N individual exponential decay channels k with amplitude A_k and characteristic decay time τ_k. The dark counts and the response times w of the APD were calibrated experimentally as shown in Figure 6.3a. The time t_0, set to the maximum of each TRPL trace, was an input parameter to the fits with the amplitudes A_k and the decay times τ_k as free fit parameters. A representative model fit to a TRPL trace obtained with three decay channels is shown in Figure 6.3a as red solid line.

As already discussed in Chapter 5 multiple transition pathways can contribute to the interlayer exciton decay dynamics in HBL systems. To identify the minimum number of channels required to approximate the multi-exponential decay of the HBL emission, the TRPL traces were fitted with a varying number of channels using Equation 6.1. The number of possible channels was increased from two up to five. For each number this analysis was applied to the whole set of TRPL measurements ranging from 35 μm down to 5 μm cavity length. The quality of each fitting procedure was assessed by the χ^2-value. An average χ^2-value for all analyzed cavity lengths is

shown in the upper panel of Figure 6.3b, where it decreased down to the measurement noise level for an increasing number of possible channels.

The χ^2-value restricts the analysis to the quantity of the overlap of the best-fit function with the measured data, neglecting the possible errors of the individual free fit parameters. According to Equation 6.1, each fitting procedure is characterized by a set of free fit parameters with respective errors. For best approximation of the TRPL data, these errors should be minimized. Therefore, an averaged error was calculated for each fit using the errors of the individual free fit parameters. A mean value for all corresponding lifetime traces results in an overall error of the free fit parameters, δ_N. The corresponding errors are shown in the middle panel of Figure 6.3b. The more possible decay channels contribute, the higher is the overall error δ_N of the free fit parameters. To establish a quantity that respects both types of errors, the product $\delta_N \cdot \chi^2$ was calculated. The result is shown in the lower panel of Figure 6.3b. This product has its minimum for three decay channels, indicating that this description is best suited to approximate the dynamics of the HBL emission both in confocal (Chapter 5) and cavity-assisted TRPL spectroscopy.

6.5 Purcell enhancement of interlayer exciton photoluminescence

Based on the preceding analysis, we extracted the characteristic time scales of interlayer exciton recombination from TRPL measurements as a function of the cavity length. Respective decay traces are shown in Figure 6.4a for cavity lengths of 35, 17 and 6 μm. Clearly, the PL decay speeds up with decreasing cavity length. This reduction of the characteristic lifetimes with decreasing cavity length was accompanied by an increase of the total PL intensity by a factor of 2.6 (Figure 6.4b) as a hallmark of cavity-induced Purcell enhancement. For a more quantitative analysis of Purcell enhancement, we applied our previously discussed model to the data set of cavity-assisted TRPL using three contributing decay channels. The corresponding model fits, shown as red solid lines in Figure 6.4a, were used to extract the functional dependence of the short, intermediate and long decay time components with the cavity length.

The respective data, shown in Figure 6.4c, clearly demonstrate cavity-control of all three characteristic decay channels. The evolution of the lifetime shortening with decreasing cavity length is quantified by the ratio of the total decay rate in the cavity

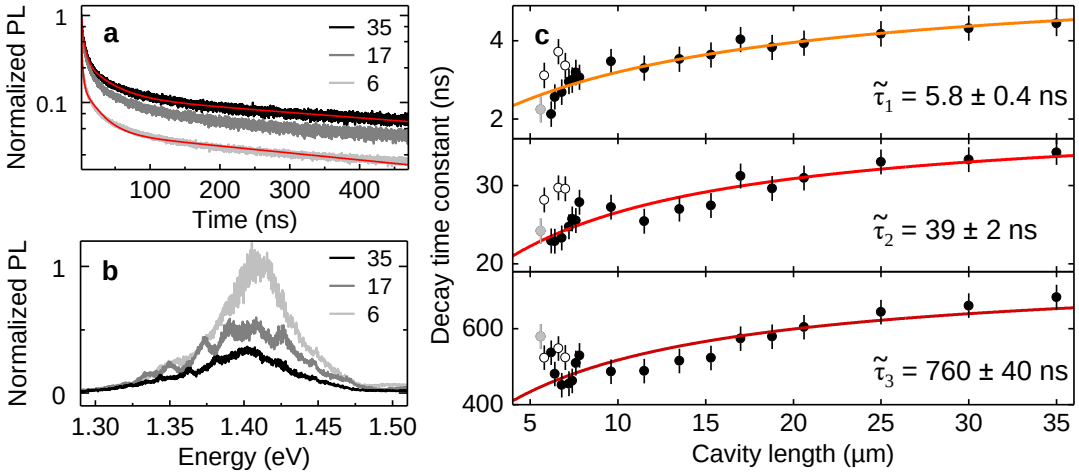

Figure 6.4: a, Traces of interlayer exciton PL decay shown for three selected cavity lengths of 35, 17 and 6 μm. The solid lines are fits to the data with three exponential decay constants. Note the speed up in the decay upon the reduction of the cavity length. **b**, Spectra of interlayer exciton PL for the corresponding cavity lengths. **c**, The evolution of the characteristic decay constants with the cavity length is shown by closed circles (error bars: least squares from best fit with three exponential decay channels). The solid lines show model fits according to the theory of generalized Purcell enhancement. Open circles represent data where the cavity mode was spectrally detuned from the resonance with the interlayer peak; data shown in light grey were discarded from the fit procedure due to presumable physical contact between the fiber and the mirror.

system $\gamma_{tot} = \gamma_{fs} + \gamma_c$ to the bare free-space decay rate γ_{fs} as $\gamma_{tot}/\gamma_{fs} = 1 + F_p$, where $F_P = \gamma_c/\gamma_{fs}$ is the Purcell enhancement factor due to the cavity-modified decay rate γ_c [101] (More details in Section 3.3). An estimate for the cavity-mediated Purcell enhancement can be obtained by identifying the values obtained from confocal PL dynamics with free-space lifetimes. Taking the smallest lifetime values for each decay channel from the data of Figure 6.4c, this yields maximum measured Purcell factors F_P of 1.8 ± 0.3, 0.8 ± 0.1 and 0.9 ± 0.1 for the short, intermediate and long lifetime components, respectively.

The difference in the Purcell factors is consistent with the different nature of the coupling between the corresponding decay channels and the cavity field, with bright interlayer excitons $\mathrm{IX_B}$ exhibiting higher coupling efficiency than grey excitons $\mathrm{IX_G}$ and phonon-assisted decay channels of momentum-dark excitons. In AA' stacking $\mathrm{IX_B}$ emission is collinear with the cavity which optimally enhances the respective decay channel. Exhibiting a similar out-of-plane emission, the recombination of grey excitons $\mathrm{IX_G}$, however, requires a spin-flip process. Facilitated by an interaction with

defects, grey excitons emit into a higher solid angle decreasing the mode overlap with the cavity. Similar considerations are possible for phonon-assisted momentum-dark excitons explaining the lower Purcell enhancement for the latter two decay channels.

All three decay channels responded consistently to cavity length detuning, as shown in Figure 6.4c. At a cavity length of 35 μm, several cavity modes were resonant with the HBL emission peak thus enhancing all possible emission channels simultaneously. For cavity lengths smaller than 9 μm, however, the free spectral range of the cavity exceeded the linewidth of the HBL emission peak, rendering cavity-coupling sensitive to the spectral resonance condition. Open circles in Fig. 6.4c show the results for off-resonant configurations in accord with cavity-inhibited radiative decay. In contrast, the on-resonance data (measured with a dense spacing of data points for $\sim 6-8$ μm cavity lengths in Figure 6.4c) reflect the effect of cavity-enhancement with anti-correlated trends for short and long decay components at smallest cavity lengths consistent with spectrally distinct channels. At a nominal separation of ~ 5 μm (grey circles), physical contact between the fiber and the extended mirror was presumably reached, preventing further reduction of the cavity mode volume.

The data recorded in contact of the fiber and the macro-mirror as well as all off-resonance data were discarded from the following analysis of the cavity-induced Purcell enhancement in the presence of pure dephasing [103]. On resonance, the generalized Purcell factor is $F_P = (4g^2/\gamma_{fs})/(\kappa + \gamma_{fs} + \gamma_d)$, where g is the coupling rate of the emitter to the cavity, κ is the cavity decay rate, and γ_d is the dephasing rate of the emitter.

In the next step, we use $\gamma_{tot}/\gamma_{fs} = (\gamma_{fs} + \gamma_c)/\gamma_{fs} = 1 + F_p$, the ratio of the total decay rate in the cavity system γ_{tot} to the free-space decay rate γ_{fs}, together with the expression for the generalized Purcell factor F_p to obtain the equation for the individual decay channels:

$$\gamma_{tot,k} = \gamma_{fs,k} \cdot \left(1 + \frac{4g_k^2/\gamma_{fs,k}}{\kappa + \gamma_{fs,k} + \gamma_d}\right), \tag{6.2}$$

In Section 6.2 we inferred the cavity decay rate κ from transmission spectra. According to Equation 3.21 it can be simplified to a constant κ_0 scaled by the cavity length. A similar behavior is attributed to the coupling g in Equation 3.22. In a final step, the rate enhancement is converted into a lifetime change via $\tau_{tot,k} = 1/\gamma_{tot,k}$ and $\widetilde{\tau}_k = 1/\gamma_{fs,k}$. The resulting fitting function takes $g_{0,k}$ and $\widetilde{\tau}_k$ as free fitting parameters.

By taking the inhomogeneous linewidth $\gamma = 55$ meV deduced from the data in Figure 5.4b as an upper bound to the dephasing rate in our system (i. e. using

$\gamma_d \leq \gamma$), we fitted each data set of Figure 6.4c according to this model. The resulting best fits, shown as solid lines in Figure 6.4c, were obtained with free-space lifetimes of 5.8 ± 0.4, 39 ± 2 and 760 ± 40 ns for the three sets of data in the respective panels of Figure 6.4c. These asymptotic values at infinite cavity length extracted from the model fit agree well with the decay times determined in confocal PL spectroscopy (data in Figure 5.4c).

With this strong confidence in the correspondence between the free-space lifetime values extracted from the model of generalized Purcell enhancement and the decay times obtained in the absence of the cavity with confocal PL spectroscopy, the model allows now to extrapolate the maximum Purcell enhancement $F_P^{\max}$ that can be achieved at the peak wavelength of the HBL emission λ for a mirror separation of $\lambda/2$. The model yields $F_P^{\max}$ of 2.9 ± 0.2 for the short and 1.7 ± 0.1 for both the intermediate and long lifetime channels, respectively. For the same limit of the intermirror spacing of $\lambda/2$ and a cavity volume of $\sim \lambda^3$, the model also quantifies the light-matter coupling strength g_0 as 195 ± 9, 58 ± 3 and 13 ± 0.9 μeV for $\mathrm{IX_B}$, $\mathrm{IX_G}$ and phonon-assisted decay of momentum-dark excitons, respectively. These values, in good quantitative agreement with the absorption contrast in Figure 5.3, are quite robust against variations in the dephasing rate, with g_0 changing by less than 25 % for γ_d in the range of $10 - 70$ meV. At the same time light-matter coupling was sensitive to material and environmental characteristics with up to 50 % changes in g_0 and about 30 % variations in the free-space PL lifetimes at different positions of the same flake and different flakes.

The values for the light-matter coupling strength g of interlayer excitons in our CVD-grown $MoSe_2$-WSe_2 HBL sample are two to three orders of magnitude smaller than the coupling rates reported for MLs TMDs [35–38]. This striking difference in light-matter coupling, fully consistent with the spatially indirect nature of interlayer excitons in HBL systems, yields tight constraints on the observation of interlayer exciton-polariton phenomena in the strong-coupling regime of HBL – cavity hybrids.

In a final step, it is instructive to calculate how an ideal emitting dipole would couple to the given cavity system. Using Equation 3.17 for an ideal Purcell enhancement of a narrow emitter coupled to a broad cavity yields an enhancement factor of 0.06 at a mirror separation of $\lambda/2$. This is a drastic reduction of the Purcell enhancement compared to the previous measurements. The difference can be explained by the description of the emitter within the two models. While the ideal Purcell factor assumes a single particle inside the resonator, the fitted model of a generalized Purcell enhancement describes a free fitting parameter g_0. This coherent

exchange rate is not necessarily attributed to a single exciton, but can also stem from collective effects induced by high exciton densities in the given HBL systems. As mentioned in Section 3.3, this coupling scales as $g \propto \sqrt{N}$ with N being the number of equally coupling excitons. Therefore, the fitted model becomes proportional to N:

$$F_{p,fit} \propto g^2 \propto N. \tag{6.3}$$

Dividing $F_{p,fit}$ by the Purcell enhancement of a single exciton $F_{p,single}$ yields

$$F_{p,fit}/F_{p,single} = N, \tag{6.4}$$

and allows to estimate N for the three contributing decay channels. We used an effective Q-factor Q_{eff} for the calculation of $F_{p,single}$ in order to account for the spectrally broad emission and calculated N for a mirror separation of $\lambda/2$. From this analysis we infer 52, 31 and 31 collectively coupling excitons for the short-lived, intermediate and long-lived decay channel, respectively.

This collective spontaneous emission, in the context of a broadened ensemble of emitters, can be expressed as a superradiant decay mechanism [144]. In recent years, experimental studies observed superradiance in conventional solid state systems like laterally arranged quantum dots [145, 146]. Our findings support observations on bulk TMD absorption [147] and suggest that interlayer excitons in the novel class of 2D material systems are a promising platform to study collective excitonic effects, giving new insights into the interpretations of observations like spatial expansion of valley polarization [24] or lasing [148].

6.6 Cavity-enhanced absorption microscopy

After probing the emission of HBL systems, the last experimental section of this chapter focuses on the absorption and scattering properties detectable with scanning cavity systems. Due to the charge carrier separation, the oscillator strength of interlayer exciton transitions is much weaker than for intralayer excitons. Therefore, detecting absorption features of these transitions remains a very delicate task, when using conventional methods like differential reflection measurements in a confocal configuration. It might be interesting to note that in the DR spectrum of Figure 5.3, 200 spectra were averaged, using the illumination limitations of the nitrogen-cooled CCD, in order to resolve the interlayer exciton absorption.

To overcome these limitations, while keeping the ability of spatially resolved measurements, we deployed a fiber-based cavity system with highly reflective

mirrors. As mentioned in Section 3.1, highly reflective resonator systems are a powerful tool for detecting weakly scattering particles. In a very pictorial view, the photon interacts with the particle multiple times due to the confinement within the resonator. The number of round-trips which a photon performs inside the resonator is given by the cavity finesse. Our cavity system had finesse values of up to 14000, enabling an increase of the sensitivity in absorption and scattering by several orders of magnitude compared to confocal spectroscopy. Both fiber and sample mirror were coated with a distributed Bragg reflector for high reflectivity values. The coating was optimized for a wavelength of 890 nm (~ 1.395 eV). The HBL sample was grown and transferred onto the mirror with the same technique as described in Section 4.2.1. An optical wide field image is shown in Figure 4.4a (the white circle indicates the area measured in Figure 6.5b, c). In this case, the PMMA used for the transfer was removed before the measurements. For more details on the scanning cavity system as well as the subsequent measurements we refer to Reference [149].

Our system allowed only measurements under ambient conditions, preventing a direct comparison of the collected data with the confocal DR spectra which were recorded at cryogenic temperatures. Nevertheless, the absolute value of the interlayer exciton absorption is not expected to be a sensitive function of the temperature, facilitating a direct comparison of this quantity. 2D transmission maps of the sample were recorded as a function of laser energy. In a second step, the extinction values for each energy were inferred from the transmission maps. The corresponding spectra as well as spatially resolved maps are presented in Figure 6.5.

The confined cavity mode interacts with the material via absorption and scattering processes, both reducing the absolute transmission. This extinction of excitation light is position dependent. Structural edges are supposed to have a higher scattering rate, whereas the inner HBL regions predominantly absorb the photons. Therefore, the two extinction spectra in Figure 6.5a can be directly related to absorption. The spectra were recorded with two orthogonal polarizations stable in the resonator due to the Cartesian symmetry of the laser-ablated depression [150]. The polarization axis was not recorded within these measurements, thus prohibiting a relation of it to the crystal axis. Interestingly, the two spectra differ not only in the absolute values of the absorption but also regarding their shape. Starting with vanishing absorption for low energies, both spectra display a rising absorption from 1.36 eV up to 1.40 eV with a strong anti-correlation at a peak (dip) close to 1.39 eV. For energies above 1.40 eV the absorption settles close to 5×10^{-3} with an offset between the polarizations. This value is consistent with the measured DR spectrum from Figure 5.3c exhibiting a

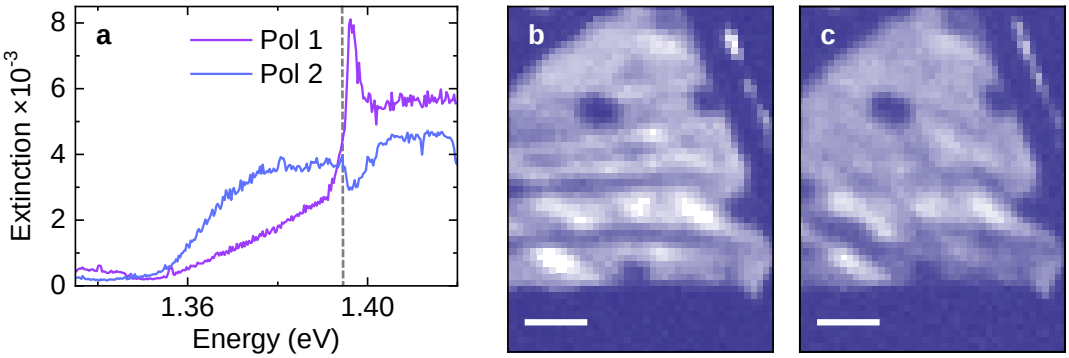

Figure 6.5: a, Cavity-enhanced extinction spectra for a CVD-grown $MoSe_2$-WSe_2 HBL structure recorded under ambient conditions. The two spectra display the different orthogonal linear polarizations, that can be excited in the optical resonator. Spatially resolved extinction maps for these polarizations are shown in **b** and **c**, recorded with an excitation at 1.395 eV indicated in **a** with a vertical dashed line (blue color in the maps corresponds to a reduced transmission value). The differences in the two images suggest that the polarization resolved measurements are sensitive to transfer-induced strain and surface irregularities. The scale bar in both images corresponds to 5 μm.

value of 0.005 (5×10^{-3}) for bright and grey interlayer exciton absorption. While this consistency with confocal measurement methods proves the validity of our scanning cavity approach, the increased sensitivity reveals additional new and unexpected phenomena like polarization dependent change of the interlayer exciton absorption.

A recent experimental study [151] reported on linearly polarized emission from corrugated $MoSe_2$-WSe_2 HBLs. The spatially resolved maps of Figure 6.5b and c indicate a similar dependence of interlayer exciton absorption upon local structural variations. Recorded at the same energy of 1.395 eV, but with two orthogonal polarizations, they display another region on the sample with the outer structural edges visible as dark blue areas. The interior part of the images stems from HBL absorption and shows different features for the two scans. While Figure 6.5b shows horizontal lines of high absorption, this contrast is suppressed in Figure 6.5c. These lines result presumably from surface irregularities and strain induced by the transfer process, which in turn affect the local properties of the HBL. Therefore, the cavity-assisted absorption spectra can be used as highly sensitive tool for detecting local strain or defects. Another polarization sensitive process that is possible within such layered materials is the generation of second harmonic photons. Facilitated by high laser powers inside the resonator two near infrared photons can be converted

to one in the visible range. In this spectral range HBLs display much stronger absorption. Being confined in the resonator, these photons have therefore a high probability to be absorbed by the heterostack. Both explanations need further investigations, but display the broad capabilities of cavity-enhanced absorption microscopy.

6.7 Conclusion

Emission and absorption properties of $MoSe_2$-WSe_2 interlayer excitons were investigated with optical resonator systems. After characterizing our cryogenic cavity system, we used its scanning capabilities as well as its length-tunability to probe the exciton decay dynamics investigated in Chapter 5. Our analysis suggests three main decay channels that we attribute to bright, grey and momentum-dark interlayer excitons. Purcell enhancement was demonstrated for all three channels, yielding values for the maximum light-matter interaction strength of 195 ± 9, 58 ± 3 and 13 ± 0.9 μeV, respectively. Finally, a highly sensitive scanning cavity system was used to measure interlayer exciton absorption of CVD-grown $MoSe_2$-WSe_2 HBLs. Spectrally resolved measurements do not only show high consistency with DR measurements in a confocal configuration, they also reveal a dependency on the orientation of the linear polarized cavity photons. 2D maps suggest an influence of transfer-induced strain and irregularities.

Chapter 7

Moiré excitons in twisted $MoSe_2$-WSe_2 heterostructures

THIS CHAPTER IS BASED ON THE MANUSCRIPT [P3]
Förg, M., Baimuratov, A. S., Kruchinin, S. Y., Vovk, I. A., Scherzer, J., Förste, J., Funk, V., Watanabe, K., Taniguchi, T. & Högele, A. Moiré excitons in $MoSe_2$-WSe_2 heterobilayers and heterotrilayers. *arXiv preprint.* arXiv: 2006.09105 (2020)

Expanding the survey of heterostructures made of $MoSe_2$ and WSe_2 this chapter presents the results of comprehensive confocal studies of corresponding HBL and HTL regions in a twisted configuration. Distinct optical signatures for both regions were observed and compared to theoretical calculations of excitons in high-symmetry stackings of the corresponding moiré superlattices. A field effect device ensured a controlled doping level of the sample. Power-dependent measurements of PL and polarization were used along with external magnetic fields to identify the dominant direct and indirect optical transitions within the two regions.

7.1 Introduction

In agreement with the result presented in Chapter 5 the majority of experimental studies interpret the HBL emission in terms of zero-momentum KK (in R-type stacking) or KK' (in H-type stacking) interlayer excitons with K or K' valley electrons and holes in $MoSe_2$ and WSe_2 [19, 25, 30, 85, 86, 152–156]. Theoretical band structure calculations, however, suggest that hybridization of Q conduction and Γ valence bands of $MoSe_2$ and WSe_2 gives rise to strong energy renormalization upon HBL formation [27, 62, 64] which might turn either QK or $Q\Gamma$ interlayer excitons into the lowest energy states. Additional complication arises in the presence of moiré effects. In moiré-modulated HBLs, electronic states exhibit valley-contrasting energy shifts upon interlayer hybridization, with states in K and K' valleys being less susceptible to energy reducing interactions than the CB states at Q or the VB states at Γ. This effect, analogous to the origin of the direct-to-indirect band gap cross-over in TMD mono- and bilayers [157–159], should also impact the band structure of HBLs [27] yet has been mostly neglected in the context of moiré excitons [31, 78, 120, 160]. Interlayer hybridization is expected to play an even more prominent role in HTL systems with native homobilayers. For the explicit case of $MoSe_2$-WSe_2 HTLs shown in Section 2.2, one would expect sizable hybridization effects between the $MoSe_2$ bilayer band edge states at Q and their counterparts in ML WSe_2, rendering the overall heterostructure an indirect band gap semiconductor.

Motivated by the contrasting behavior anticipated for momentum direct and indirect band edge interlayer excitons in $MoSe_2$-WSe_2 HBL and HTL, we performed optical spectroscopy studies of a corresponding moiré heterostructure. Confocal inspection methods like SHG, PL and DR spectroscopy were employed within a charge-controlled environment to infer the stacking along with a comprehensive characterization of the optical transitions. Exciton g-factors were determined from magneto-luminescence experiments and suggest, together with theoretical predictions, momentum direct and indirect transitions of HBL and HTL PL, respectively.

7.2 Basic optical characterization

In order to minimize structural differences of HBL and HTL regions, same stacking type and twist-angle have to be ensured. To this end, a $MoSe_2$ crystal with mono- and bilayer regions was stacked onto a WSe_2 ML by dry viscoelastic stamping [126] and encapsulated from both sides by hexagonal boron nitride. The $MoSe_2$ crystal with a

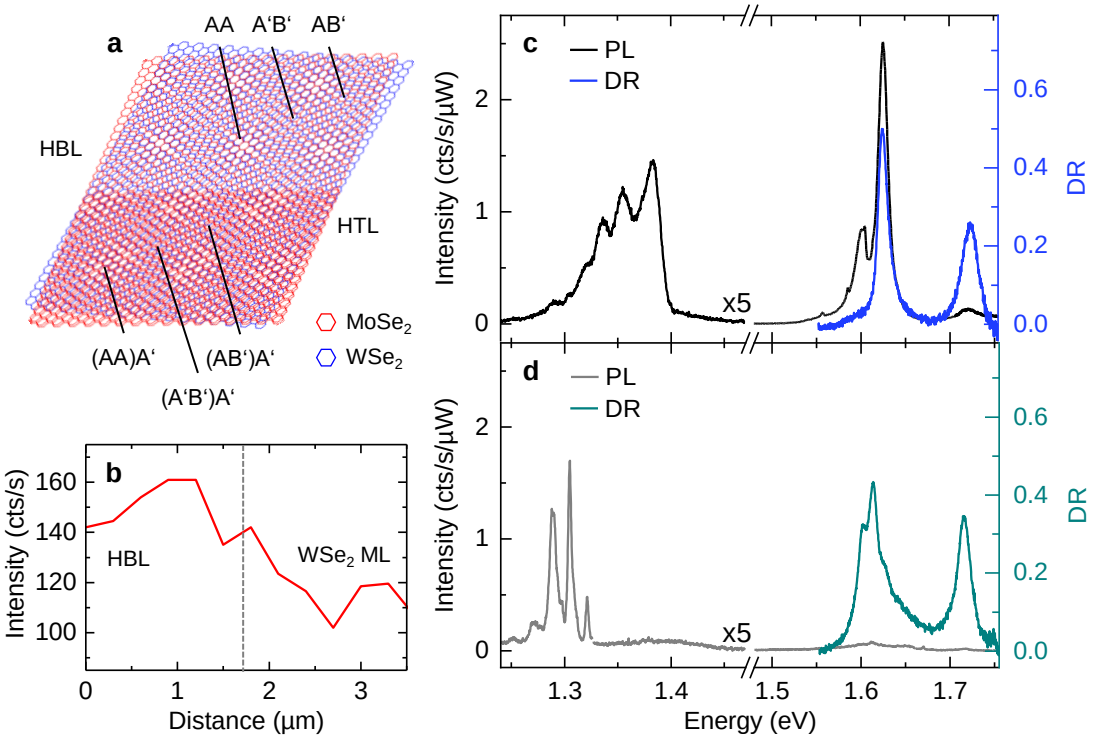

Figure 7.1: **a**, Schematics of twisted HBL and HTL $MoSe_2$-WSe_2 with different high-symmetry stackings. **b**, Second harmonic intensity as as a function of sample position. Scanning from the HBL region to the ML of WSe_2 displays a drop in intensity documenting the R-type stacking geometry. The interface is marked with a dashed line. **c** and **d**, Photoluminescence (black and grey) and differential reflectivity (blue and dark cyan) spectra of twisted HBL and HTL $MoSe_2$-WSe_2 at 3.2 K. The luminescence was excited with linearly polarized excitation at 1.85 eV and scaled in intensity below 1.47 eV by a factor of 5 in both graphs.

native bilayer region in 2H or AA' stacking was twisted by about 4° with respect to the WSe_2 ML. A schematic drawing of both regions is shown in Figure 7.1a, a more detailed description of sample fabrication is presented in Section 4.2.2. The actual stacking of the resulting structure was inferred from SHG measurements by scanning from the HBL region to the ML of WSe_2. Figure 7.1b illustrates the drop in SHG intensity when probing the ML and identifies the sample to be in R-type registry. At the relatively large twist angle of 4°, we expect the moiré heterostructure to be robust against reconstruction [81, 82] and thus to contrast previous studies of $MoSe_2$-WSe_2 HBLs carefully aligned for zero twist angle in R-type stacking [25, 155] as well as moiré-free HBLs obtained from chemical vapor deposition with lattice-mismatch relaxation and inherent alignment [30, P2].

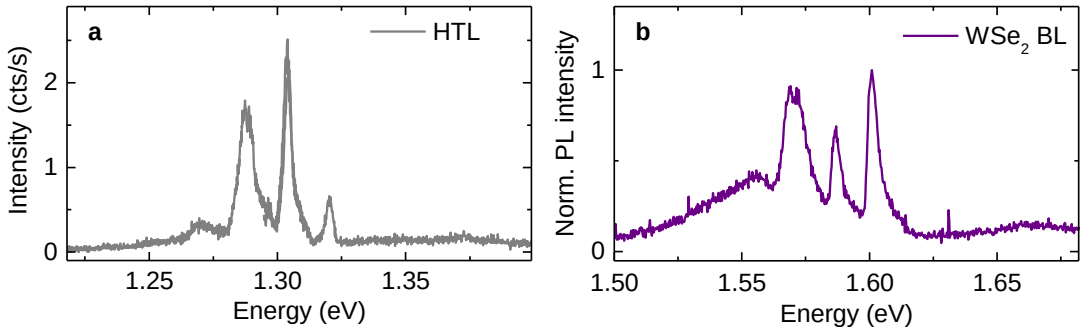

Figure 7.2: a, Photoluminescence of twisted HTL $MoSe_2$-WSe_2 **b**, Photoluminescence from an exfoliated bilayer WSe_2 adapted from Reference [P5]

Cryogenic PL and DR spectra of the HBL and HTL regions at zero gate voltage are shown in Figure 7.1c and d, respectively. The DR features in the spectral range between 1.55 eV and 1.75 eV are consistent with absorption characteristics of intralayer excitons. Whereas the two dominant DR peaks of the HBL spectrum in Figure 7.1c essentially reflect the respective $MoSe_2$ and WSe_2 ML transitions around 1.6 and 1.7 eV, the HTL spectrum in Figure 7.1d is different. Compared to the HBL spectrum, it exhibits a red-shift of the WSe_2 intralayer exciton peak by 8 meV because of Coulomb screening by the additional $MoSe_2$ layer, and a rich structure around the $MoSe_2$ absorption peak with possible contributions from interlayer excitons of bilayer $MoSe_2$ [161] as well as moiré miniband effects [160] in the twisted HTL.

Within the same energy range, the cryogenic PL is consistently dominated by intralayer excitons. Remarkably, the intralayer $MoSe_2$ and WSe_2 peaks in the HBL spectrum of Figure 7.1c are nearly completely quenched in the HTL spectrum of Figure 7.1d, indicating for the latter drastically suppressed hot luminescence due to enhanced population relaxation into lowest-energy interlayer exciton levels. This observation is in accord with the theoretical prediction of increased charge transfer efficiency via hybridized Q and Γ states in heterostructures [27]. Another striking difference in the PL from HBL and HTL is evident for interlayer excitons with emission around 1.35 and 1.30 eV in the spectra of Figure 7.1c and d, respectively. Consistent with finite twist angle, the multi-peak PL of the HBL around 1.35 eV is reminiscent of rich $MoSe_2$-WSe_2 moiré spectral features [85] rather than of simple spectra from aligned HBLs [25, 152–156]. The PL of the HTL shows a red-shift of $\sim$ 80 meV upon the addition of an extra $MoSe_2$ layer and exhibits a different spectral structure that is strikingly similar to the cryogenic PL from bilayer WSe_2 [P5] shown in Figure 7.2.

Apart from the shifted energy range due to the band offset and variations in the relative intensities the two spectra in Figure 7.2a and b show high similarity. The four peaks in both spectra display an almost equal energy-spacing, linewidth and shape. This spectral resemblance indicates indirect excitonic transitions for the HTL akin to phonon-sidebands of QK, $K\Gamma$ and $Q\Gamma$ excitons in bilayer WSe_2 [P4, P5].

7.3 Voltage-controlled doping

To provide a well-defined doping environment for subsequent measurements, we monitored the evolution of PL and DR as a function of an external gate-voltage. Figure 7.3 shows the optical response of different sample regions upon external doping. Using the voltage-dependent response of ML PL, which was subject of various studies [14, 162–164], as a reference we can identify different doping regimes. The ML of $MoSe_2$ shows a significant change of the PL when the gate-voltage is close to -2.5 V (Figure 7.3a). The neutral $MoSe_2$ intralayer exciton (X_M) dominates at voltages below -2.5 V with a simultaneous suppression of the lower lying trion feature indicating the transition from the negatively charged to the neutral regime. A similar doping dependence is observed for ML WSe_2 in Figure 7.3b supporting the notion of a small electron doping for 0 V gate voltage. The observed residual n-doping is consistent with experimental results of other exfoliated crystals [P4, P5, 162, 163].

In addition, intralayer excitons of $MoSe_2$ and WSe_2 were probed on the HBL region using DR spectroscopy. Figure 7.3c shows the observed voltage dependence. While the intralayer exciton of WSe_2 (X_W) is robust against the doping variation, X_M exhibits a higher intensity when reaching charge neutrality at -2.5 V. The false-color plot of DR spectra from the HTL (Figure 7.3e) reveals similar trends upon doping variations. Consistent with measurements on individual MLs, HBL and HTL regions exhibit the same small n-doping for 0 V gate voltage as a global sample characteristic.

Finally, interlayer exciton PL was recorded as a function of the external voltage. The according false-color plots are shown in Figure 7.3d and Figure 7.3f for HBL and HTL, respectively. The interlayer exciton features display variations in their transition energy and intensity as a function of the doping regime. Compared to charge neutrality, the emission intensity gets blue-shifted and quenched in the n-doped regime for all peaks in Figure 7.3d and f. The blue-shift is consistent with other studies of gate-tunable HBLs [19, 25] resulting from the interaction of

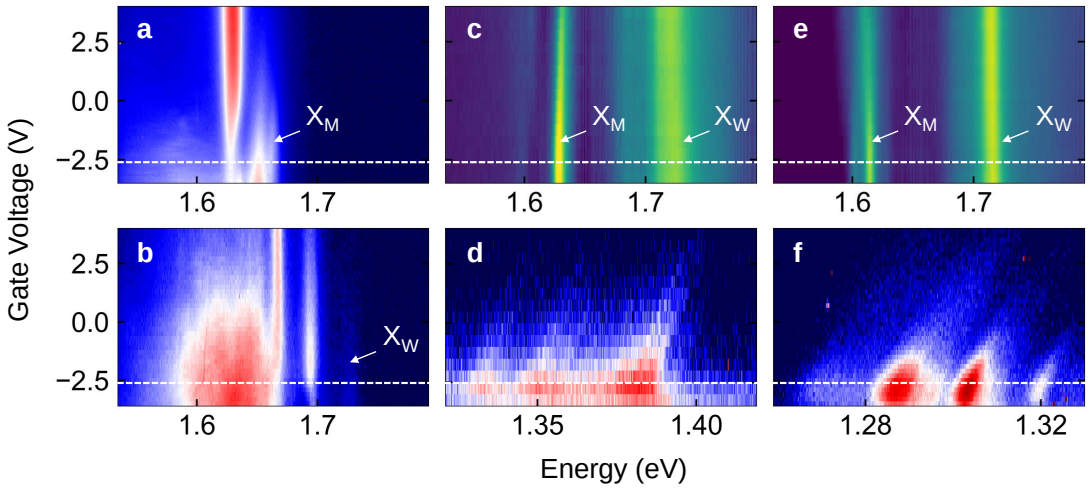

Figure 7.3: Optical response of different sample regions upon external doping. False-color plots of ML PL as a function of gate-voltage are shown in **a** and **b** for $MoSe_2$ and WSe_2, respectively. Voltage-dependent measurements probing the HBL are shown in **c** and **d**. While **c** displays a voltage-dependent plot of DR featuring intralayer optical transitions, **d** presents interlayer exciton PL. The similar set of measurments is shown in **e** and **f** for the HTL. Energetic positions of intralayer excitons of $MoSe_2$ and WSe_2 are labeled as X_M and X_W in **a**,**b**,**c**,**e**. The intersection from charge neutrality to a negative doping level is indicated in all graphs with a horizontal dashed line.

the interlayer exciton dipole moment with the external electric field. Furthermore, excess electrons in the negative regime can serve as scatterers for interlayer excitons reducing the radiative recombination. In contrast to these spectral variations, the overall spectral shape is conserved. Therefore, we expect no significant changes of the interlayer exciton properties when measuring at charge neutrality (-2.5 V) or with a small electron doping (0 V). In order to prevent the sample from a breakdown of the field effect device, measurements in Section 7.2, Section 7.5 and Section 7.6 were performed at 0 V.

7.4 Optical transitions from density functional theory

The differences in the PL spectra of Figure 7.1c and d suggest different origins for the interlayer exciton PL in $MoSe_2$-WSe_2 HBL and HTL. To provide a basis for the interpretation of our observations, we performed numerical calculations of the band structure and exciton g-factors with DFT in generalized gradient approximation (see Section 2.2.2 and Appendix A for details). Assuming that the twist angle

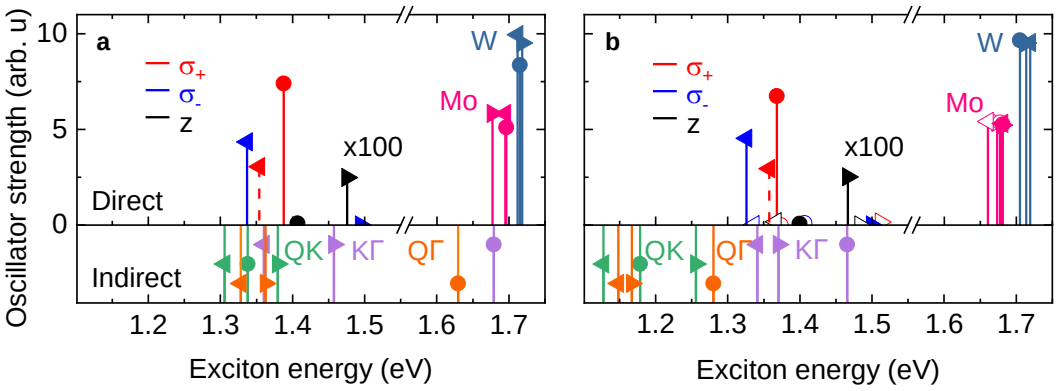

Figure 7.4: Energy and oscillator strength calculated for intralayer and interlayer excitons in **a** HBL and **b** HTL for three different stackings. The symbols ◀, ●, and ▶ denote A'B', AA, and AB', and (A'B')A', (AA)A', and (AB')A' stackings in HBL and HTL, respectively. Empty symbols ◁, ○, and ▷ indicate HTL excitons with electrons residing in the top-most $MoSe_2$ layer. The oscillator strength of interlayer excitons was scaled by a factor of 100. For zero-momentum KK interlayer excitons (top panels) we indicate the spin configuration by solid and dashed lines for spin-like and spin-unlike states, and the polarization of the respective exciton emission by red (σ^+), blue (σ^-) and black (in-plane z) colors. The bottom panels show the energy of finite-momentum interlayer excitons in QK (green), $Q\Gamma$ (orange) and $K\Gamma$ (violet) configurations without direct radiative transitions.

is sufficiently small to employ the local band structure approximation [120, 121], we restrict our analysis to three high symmetry points of the moiré superlattice in each heterostructure with stackings indicated in Figure 7.1a (see Section 2.2.1 for a detailed representation of the stackings). Using the band structure results from DFT, we employed the Wannier exciton model in the effective mass approximation [69] to calculate the energies of intralayer and interlayer excitons in different spin-valley configurations.

In the top panels of Figure 7.4a and b we plot the oscillator strength of direct KK exciton transitions in different R-type stackings of HBL and HTL. For all stackings, interlayer excitons exhibit at least two orders of magnitude lower oscillator strengths than their intralayer counterparts [62] with dipolar selection rules in agreement with the group theory analysis of R-type HBL [P2, 78]. In accord with previous calculations for HBLs, we find the lowest-energy KK interlayer exciton for A'B' [62, 120] and energetically higher excitons for AA and AB' stackings. In all HBL stackings of R-type registry considered here, the lowest KK interlayer exciton is spin-like, ~ 20 meV below its spin-unlike counterpart. In AA stacking, the spin-like

state has largest oscillator strength, whereas for spin-unlike states only the KK exciton in A'B' stacking has a sizable oscillator strength in agreement with previous DFT results [62, 64].

For the HTL, our calculations predict an increase in the number of CBs associated with lowest energy excitons due to the additional $MoSe_2$ layer. As such, interlayer KK excitons can be grouped according to the localization of the CB electron in one of the $MoSe_2$ layers. For electrons localized on the $MoSe_2$ with immediate proximity to WSe_2 (full symbols in Figure 7.4b), the corresponding interlayer excitons feature similar energies (with a small red-shift due to modified screening) and oscillator strengths as in the HBL system. Additional interlayer states arise from excitons with the electron localized in the upper $MoSe_2$ layer (open symbols in Figure 7.4b). Their energetic ordering, with spin-unlike configuration again being lowest, and dipolar selection are identical to KK interlayer excitons in HBLs of H-type registry [P2, 78]. However, the corresponding transitions have a drastically inhibited oscillator strengths due to a reduced wavefunction overlap between the electron and hole in the topmost $MoSe_2$ and the bottom WSe_2 layer and thus should not contribute sizably to the PL of HTL [165].

In addition to KK excitons, our calculations yield the energies of momentum-indirect QK, $Q\Gamma$ and $K\Gamma$ excitons (bottom panels of Figure 7.4a and b) composed from electrons in Q or K valleys and holes at K or Γ. Note that the notion of oscillator strength is meaningless for momentum-indirect excitons without direct radiative decay pathways. The energetic ordering of interlayer excitons with zero and finite center-of-mass momentum differs substantially in HBL and HTL systems: whereas our calculations predict energetic proximity for KK, QK and $K\Gamma$ states in HBLs, finite-momentum QK and $Q\Gamma$ states in HTLs are energetically well below the direct KK states, with an energy difference in the order of 200 meV. This trend is well known for mono- and bilayer TMDs, where the states at K are much less sensitive to the addition of one layer than the states at Q and Γ [70, 157–159].

7.5 Power-dependent photoluminescence

We find experimental support for our theoretical description of HBL and HTL excitons by probing the PL and the degree of circular polarization (P_C) at increasing excitation powers. The corresponding results are shown in Figure 7.5a, b and c, d for HBL and HTL, respectively. Upon increasing excitation power from 0.1 to 100 μW, the HBL spectrum develops a pronounced shoulder above 1.40 eV in

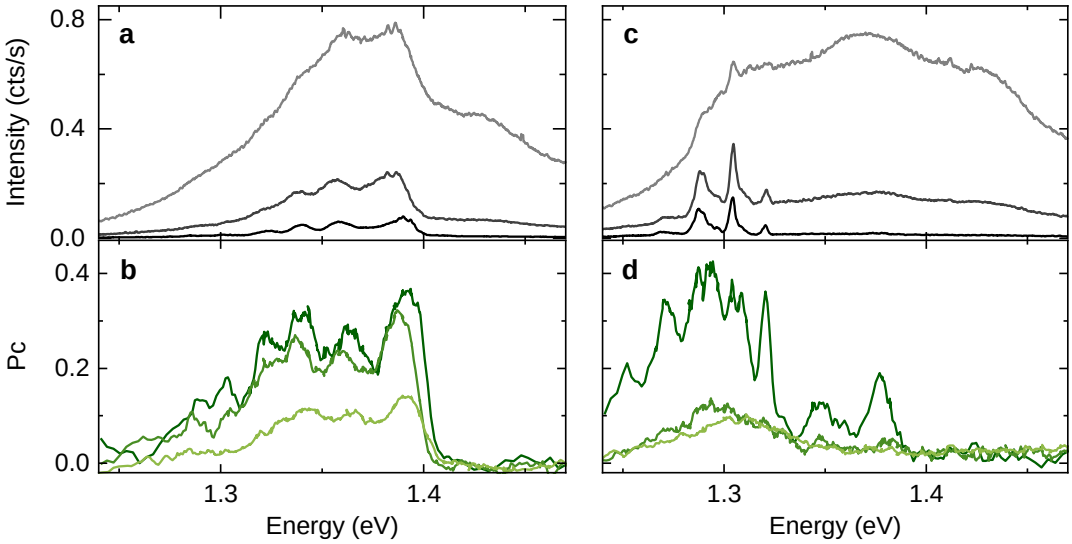

Figure 7.5: a, c Photoluminescence spectra and **b, d** degrees of circular polarization ($\mathrm{P_C}$) for twisted HBL and HTL $MoSe_2$-WSe_2, respectively, at different excitation powers. Photoluminescence and $\mathrm{P_C}$ are color-coded from black to grey and dark green to light green for increasing excitation powers of 0.1, 10 and 100 μW. Both HBL and HTL exhibit photoluminescence brightening above 1.40 eV accompanied by an overall decrease in the degree of circular polarization with increasing excitation power. Note the peaks in HTL $\mathrm{P_C}$ at 1.35 and 1.38 eV.

Figure 7.5a with vanishing $\mathrm{P_C}$ in Figure 7.5b. This feature is consistent with PL from interlayer excitons in AB' stacking with in-plane linear polarization (z-polarized states in Figure 7.4a) collected by our high-NA objective. It requires sufficiently high excitation powers to be observed as hot luminescence from energetically higher states.

In contrast, the brightest PL peaks around 1.40 eV with a positive degree of circular polarization are present down to lowest excitation powers. They can be assigned to spin-like or spin-unlike KK interlayer excitons in AA and A'B' stacking, respectively (states in Figure 7.4a with σ^+ polarization). However, since the sign reversal in $\mathrm{P_C}$ for the lowest-energy spin-like KK interlayer exciton in A'B' stacking (state in Figure 7.4a with σ^- polarization) is missing at the low-energy side of the structured HBL PL spectrum [85], strong contribution from A'B' stacking seems unlikely. Instead, the spectrum appears to be dominated by KK interlayer excitons from AA regions, with PL energies modulated by moiré miniband effects.

Our theory also provides means to understand the differences in the HBL and HTL PL spectra. The data in Figure 7.5c highlight the presence of circularly polarized

KK interlayer exciton transitions in HTL via power-activated hot luminescence at energies above 1.35 eV. This scenario is corroborated further for the lowest excitation power (dark green data in Figure 7.5d) by two peaks with finite P_C at 1.35 and 1.38 eV stemming from KK interlayer excitons with σ^+ polarization in both (A'B')A and (AA)A stackings. Moreover, as for the HBL, the HTL spectrum at 100 μW excitation power in Figure 7.5c exhibits a strong highest-energy PL shoulder around 1.45 eV from z-polarized states in (AB')A stacking with vanishing P_C. The low-energy peaks around 1.30 eV, on the other hand, can be interpreted as phonon sidebands of momentum-dark QK or $Q\Gamma$ interlayer exciton reservoirs (lowest states in Figure 7.4b). Without removing the ambiguity in the assignment of the lowest-energy reservoir to QK or $Q\Gamma$, this scenario explains the similarity in the spectral shape of HTL PL and the PL of native bilayer WSe_2 originating from momentum-indirect excitons [P4, P5].

7.6 Exciton g-factors from experiment and theory

To clarify the origin of the HTL PL and to provide further insight into the multi-peak structure of the HBL emission, we performed magneto-luminescence experiments in Faraday configuration and compared the results with theory. The dispersion of the PL peaks in external magnetic field applied perpendicular to the heterostructure is shown in Figure 7.6. The solid black lines indicate linear energy shifts recorded for σ^+ (σ^-) circularly polarized PL at positive and negative magnetic fields. From this set of data, we determine the respective g-factors using the relation $\Delta E = g\mu_B B$, where ΔE is the energy splitting between σ^+ and σ^- polarized peaks proportional to the interlayer exciton g-factor, μ_B is the Bohr magneton, and B is the magnetic field. For the HBL, the extracted g-factors range between -4.2 and -6.2 with the same sign as for WSe_2 intralayer excitons, whereas the HTL peaks exhibit g-factors between -12 and -13.

The experimental g-factors determined for the HBL peaks from the data of Figure 7.6a and b (-6.2 ± 0.8, -4.2 ± 0.8 and -5.5 ± 0.8) are consistent with previous studies of aligned $MoSe_2$-WSe_2 heterostructures in R-type registry with absolute values in the range from 6.1 to 8.5 [25, 86, 155]. They contrast the g-factors between 15 and 16 of interlayer excitons in HBL of H-type registry [21, 86, 153, 156]. For the respective KK interlayer excitons in R-type HBLs, our calculations predict (see Table 7.1) an absolute g-factor value close to 6 and opposite signs for the degrees of circular polarization in AA and A'B' stackings (with negative and positive P_C,

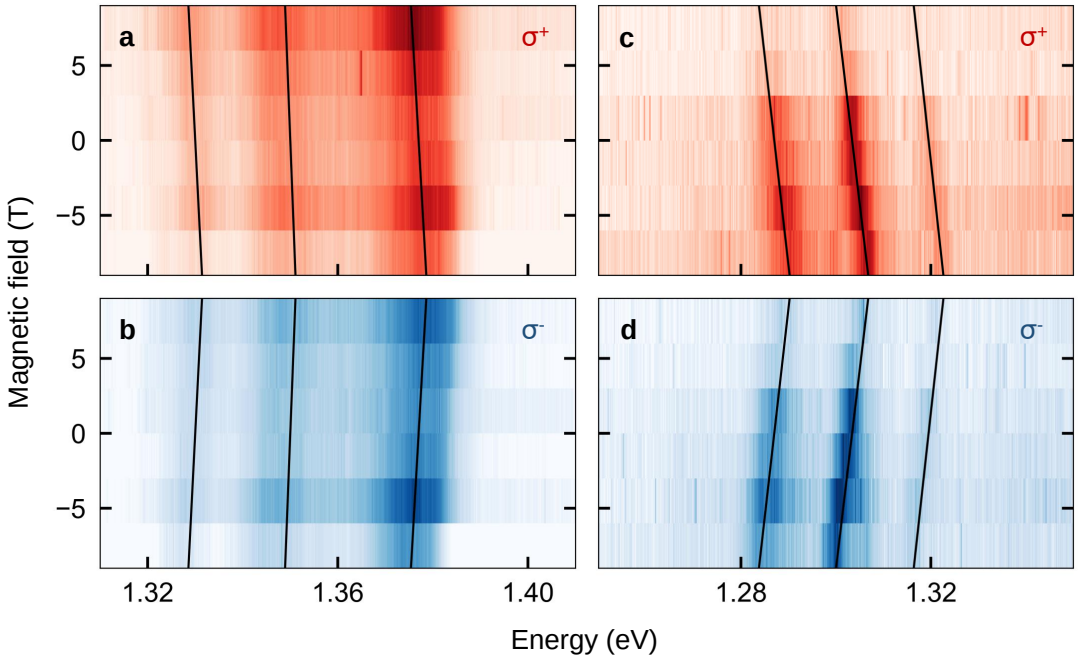

Figure 7.6: **a** and **b**, Magneto-luminescence of HBL $MoSe_2$-WSe_2 for linear excitation and σ^+ (red) and σ^- (blue) circularly polarized detection, respectively. **c** and **d**, Same for HTL $MoSe_2$-WSe_2. The solid lines show magneto-induced energy shifts of HBL and HTL peaks with g-factors (from high to low energy) of -6.2 ± 0.8, -4.2 ± 0.8 and -5.5 ± 0.8, and -12.0 ± 2.0, -12.0 ± 0.8 and -13.0 ± 0.8, respectively.

respectively), in agreement with a similar theoretical analysis of interlayer exciton g-factor values and signs [166, 167]. The negative sign of the g-factor determined for all HBL peaks supports their assignment to interlayer excitons of AA stacked regions. This finding implies that AA domains dominate the PL from rigid HBL moiré supercells, although A'B' regions should be at least of comparable size [81]. In the presence of reconstruction effects at small twist angles, in contrast, one would expect the spectra to be dominated by interlayer excitons from energetically favored A'B' and AB' triangular domains of comparable area [81–83].

For the HTL peaks of Figure 7.6, the g-factor of about -12 helps to discriminate the QK interlayer exciton reservoir from $K\Gamma$ and $Q\Gamma$. According to our theory analysis, the latter exhibit small g-factors due the vanishing valley Zeeman terms in the Γ valley. The experimentally observed g-factor values suggest spin-unlike $Q'K$ interlayer excitons as the main reservoir for the lowest-energy HTL emission. The theoretical calculated g-factor of 14 is likely overestimating the actual value due to

	KK		K'K		QK		Q'K	
Stacking	↑↑	↓↑	↑↑	↓↑	↑↑	↓↑	↑↑	↓↑
AA	**−6.4**	11.0	13.0	**17.6**	**9.0**	13.3	10.7	**15.0**
A'B'	**+5.8**	−10.5	13.1	**17.8**	**8.6**	13.0	10.6	**14.9**
AB'	**6.3**	+10.9	13.0	**17.6**	**8.7**	12.9	11.0	**15.3**
(AA)A'	**−6.3**	11.6	12.6	**17.9**	**9.9**	14.1	10.1	**14.3**
(A'B')A'	**+5.9**	−10.8	13.1	**17.9**	**9.5**	13.8	10.1	**14.4**
(AB')A'	**6.3**	+12.2	12.0	**18.0**	**9.6**	13.9	10.4	**14.6**
(AA)A'	+12.8	**−18.1**	**6.1**	11.4	9.1	13.3	10.9	15.1
(A'B')A'	13.1	**+18.0**	**5.9**	10.7	8.8	12.9	10.9	15.1
(AB')A'	−12.9	**18.8**	**5.5**	11.4	9.1	12.9	11.3	15.1
	KΓ		K'Γ		QΓ		Q'Γ	
Stacking	↑↑	↓↑	↑↑	↓↑	↑↑	↓↑	↑↑	↓↑
AA	**3.6**	1.0	3.0	**7.6**	**1.0**	3.3	0.7	**5.0**
A'B'	**4.0**	0.7	3.3	**8.0**	**1.1**	3.2	0.8	**5.1**
AB'	**3.7**	1.0	3.0	**7.7**	**1.3**	2.9	1.1	**5.3**
(AA)A'	**3.8**	1.5	2.5	**7.8**	**0.2**	4.0	0.0	**4.2**
(A'B')A'	**4.0**	0.8	3.2	**8.0**	**0.4**	3.8	0.2	**4.4**
(AB')A'	**3.8**	2.1	1.9	**7.8**	**0.5**	3.7	0.3	**4.5**
(AA)A'	2.7	**8.0**	**4.0**	1.3	1.0	3.2	0.8	5.0
(A'B')A'	3.2	**8.0**	**4.0**	0.8	1.2	3.0	1.0	5.2
(AB')A'	2.8	**8.7**	**4.7**	1.2	1.0	2.8	1.2	5.0

Table 7.1: Calculated g-factors of interlayer excitons in R-type $MoSe_2$-WSe_2 HBL and HTL in spin-like (↑↑) and spin-unlike (↓↑) configurations of CB electrons in K, K', Q or Q' valleys of $MoSe_2$ and empty VB states at K in WSe_2 or at Γ in the hybrid band of $MoSe_2$-WSe_2. For each spin-valley configuration, the g-factors corresponding to the lower-energy state are shown in bold. For the HTL, the upper (lower) blocks shows KK, K'K, KΓ, and KΓ excitons with the CB electron localized in the lower (upper) $MoSe_2$ layer, as well as QK, Q'K, QΓ, and QΓ excitons with small (large) hybridization with WSe_2 CB states. The sign convention for KK interlayer exciton g-factors is the same as for the intralayer excitons in WSe_2; only absolute values are given for momentum-indirect interlayer excitons and direct KK excitons with z-polarized in-plane emission.

the highly delocalized charge carriers in the trilayer structure [168]. KK or KK' phonon sidebands are also consistent with the observed g-factor, but can be excluded due to the energetic ordering. Lowest excitations in K and K' valleys have g-factors

of 6 or 18. The HBL, in contrast, exhibits no signatures of the respective states with similar g-factors despite their energetic proximity. This allows us to conclude that KK interlayer excitons dominate the PL of twisted $MoSe_2$-WSe_2 HBL, whereas its HTL counterpart exhibits PL due to phonon-assisted emission from finite-momentum $Q'K$ states.

7.7 Conclusion

In conclusion, we carried out experimental and theoretical studies of excitons in twisted $MoSe_2$-WSe_2 HBL and HTL of R-type registry. To interpret our observations from optical spectroscopy experiments, we performed DFT calculations of the band structures, exciton states and g-factors for $MoSe_2$-WSe_2 HBL and HTL. Our results suggest that the PL of twisted R-type HBLs stems from momentum-direct interlayer excitons with emission energies modulated by moiré effects. In contrast, the HTL spectra of the $MoSe_2$-WSe_2 heterostructure are dominated by momentum-indirect interlayer excitons, highlighting the role of hybrid interlayer states for the relaxation and formation of excitons in twisted van der Waals heterostructures.

Chapter 8

Summary and perspectives

Within this thesis, heterostructures made of $MoSe_2$ and WSe_2 were studied employing comprehensive spectroscopic methods. In HBL systems, the staggered band alignment [18] facilitates the formation of interlayer excitons. We focused on the optical properties of these long-lived bosonic quasiparticles with a permanent and fixed dipole moment. Starting with two inherently aligned layers, CVD-grown HBLs were investigated with a confocal microscope under cryogenic conditions inferring the actual atomic registry from optical properties. While spatially resolved SHG signals characterized the sample to exhibit an R-type stacking, the onset of absorption from DR measurements along with a polarization switching of PL identified the grown structure to be in AA' atomic registry. In this context, the interlayer exciton emission was modeled as a convolution of three contributing channels. ZPLs of bright and grey interlayer excitons contribute to the high energy side of the emission peak, whereas the low energy side is governed by phonon-assisted processes. Finally, TRPL revealed distinct recombination times for the individual channels supporting the presented spectral deconvolution.

Equipped with the free-space decay rates of interlayer excitons from confocal spectroscopy we deployed a fiber-based microcavity system to investigate the light-matter interaction of interlayer excitons. After characterizing the decay rate of the resonator, we used its imaging capabilities to probe the same sample position as in the initial confocal studies. An accurate tuning of the intermirror distance was utilized to monitor the decay dynamics of bright, grey and momentum-indirect intelayer excitons upon a decreasing cavity length. Employing a model of collective Purcell enhancement, we deduced the maximum ligh-matter interaction strength g for the individual channels to be 195 ± 9, 58 ± 3 and 13 ± 0.9 μeV, respectively. These values are two to three orders of magnitude smaller than the coupling rates of intralayer excitons in ML TMDs [35–38] in accordance with the reduced wavefunction overlap of the layer-seperated electron-hole pairs. In addition to the coherent

exchange rate, interlayer exciton absorption was probed with a complementary scanning-cavity setup at room temperature. While the absolute value of absorption is consistent with confocal DR spectroscopy, the high sensitivity allowed to detect polarization-dependent features. The indicated strain-susceptibility can be used for sensing applications and lays the foundations for subsequent experiments.

The origin of lowest energy PL in $MoSe_2$-WSe_2 HBLs remains a subject of debate [169] rendering the band gap of the assembled structures to be either of direct [19, 25, 30, P2, 85, 86, 152–156] or indirect [20, 27, 62, 64, 170, 171] nature. The unknown strength of interlayer hybridization leads to this inconclusive scenario in HBL systems and is expected to play an even more important role in systems of three or more layers. In order to remove this ambiguity, we investigated a twisted $MoSe_2$-WSe_2 heterostructure featuring HBL and HTL regions. A global twist-angle ensured the same structural behavior for both positions, which displayed distinct PL signatures. The spectroscopic experiments were conducted within a controlled doping environment and complemented by numerical DFT calculations. Based on measurements of power-dependent PL we attributed the contributions of the individual stackings in the moiré-modulated structure. Furthermore, the exciton g-factors were inferred from magneto-luminescence experiments. In comparison with the resulting g-factors from DFT calculations, it is possible to distinguish the momentum-direct KK transitions in HBLs from the momentum-indirect $Q'K$ transitions in HTL spectra. Our results highlight the role of exciton g-factors for the assignment of hybrid interlayer states in van der Waals heterostructures.

In addition, the optical response upon external magnetic fields can be used to detect signatures of strongly-interacting particles in twisted van der Waals heterostructures [33]. Motivated by the observation of superconducting and Mott-insulating states in twisted bilayer [172, 173] and trilayer [174, 175] graphene, recent experimental studies report on correlated phenomena in TMD homobilayers [88] and HBLs [32, 33]. The moiré superlattice in these heterostacks gives rise to spatial variations of the electronic band structure , thus providing a realization of the triangular Hubbard model [176]. Therefore, these artificially arranged semiconductors are a promising platform for the simulation of correlated many-body ground states like spin-liquids and chiral d-wave superconductors in solid-state-based materials. Beside intriguing transport phenomena, van der Waals heterostructures exhibit promising optical properties. Our experimental results suggest a collective recombination mechanism of interlayer excitons. Entering the regime of strong coupling was, however, inhibited by high dephasing rates in the presented sample. Combining highly reflective

cavities [177] with narrow band emission from moiré excitons [86] can pave the way towards dipolar exciton-polariton gases. Such systems promise the observation of condensation phenomena [23, 178] or unidirectional robust transport of edge states in topological insulators [179]. While the well-conceived assembly of known layered materials displays promising physical phenomena, the majority of potential 2D components has not yet been studied experimentally [180]. Therefore, van der Waals heterostructures are likely to remain a topic of focused research in condensed matter physics for many years.

Appendix A

Numerical results from density functional theory

THIS CHAPTER IS BASED ON THE SUPPLEMENTARY INFORMATION OF THE MANUSCRIPT [P3]

Förg, M., Baimuratov, A. S., Kruchinin, S. Y., Vovk, I. A., Scherzer, J., Förste, J., Funk, V., Watanabe, K., Taniguchi, T. & Högele, A. Moiré excitons in $MoSe_2$-WSe_2 heterobilayers and heterotrilayers. *arXiv preprint.* arXiv: 2006.09105 (2020)

Based on our DFT calculations (details in Section 2.2.2), we used the Wannier exciton model in the effective mass approximation [69] to calculate the exciton energies E_X for different spin-valley configurations shown in Figure 7.4, obtained as

$$E_X = E_{\mathrm{g}}^{\mathrm{DFT}} + E_{\mathrm{g}}^{\mathrm{offset}} - E_{\mathrm{b}}, \tag{A.1}$$

from the DFT quasiparticle band gap energy $E_{\mathrm{g}}^{\mathrm{DFT}}$ corrected by an offset $E_{\mathrm{g}}^{\mathrm{offset}}$ that accounts for an underestimated band gap, and the exciton binding energy E_{b}. $E_{\mathrm{g}}^{\mathrm{offset}} = 480$ meV was used as a global energy offset for all exciton configurations by placing experimental and theoretical energy positions of KK interlayer excitons of WSe_2 in resonance.

To determine the exciton binding energy we solved the stationary Schrödinger equation of the electron–hole relative motion

$$\left[-\frac{\hbar^2}{2\mu}\nabla^2 + V(\rho)\right]\psi(\rho) = E_n\psi(\rho), \tag{A.2}$$

where $\psi(\rho)$ is the radial wave function, $\mu = m_{\mathrm{e}}m_{\mathrm{h}}/(m_{\mathrm{e}} + m_{\mathrm{h}})$ is the reduced effective mass, m_{e} and m_{h} are the effective masses of the electron and the hole, ε is the effective dielectric constant, and $V(\rho)$ is the Rytova–Keldysh potential [181, 182] of the form

$$V(\rho) = -\frac{\pi e^2}{2\varepsilon\rho_0}\left[H_0\left(\frac{\rho}{\rho_0}\right) - Y_0\left(\frac{\rho}{\rho_0}\right)\right]. \tag{A.3}$$

Stacking	k-point	Electron Layer	m_e (m_0)	k-point	Hole Layer	m_h (m_0)	Energy gap $E_g(eV)$
AA	K	W	0.38	K	W	0.47	1.4
	K	Mo	0.67	K	Mo	0.74	1.43
	K	Mo	0.7	K	W	0.47	1.12
	K	Mo	0.67	K	W	0.47	1.1
	Q	Mo/W	0.66	K	W	0.47	1.05
	K	Mo	0.67	Γ	W/Mo	1.36	1.43
	Q	Mo/W	0.66	Γ	W/Mo	1.36	1.38
A'B'	K	W	0.37	K	W	0.44	1.39
	K	Mo	0.63	K	Mo	0.71	1.42
	K	Mo	0.71	K	W	0.44	1.06
	K	Mo	0.63	K	W	0.44	1.04
	Q	Mo/W	0.66	K	W	0.44	1.01
	K	Mo	0.63	Γ	W/Mo	0.85	1.09
	Q	Mo/W	0.66	Γ	W/Mo	0.85	1.06
AB'	K	W	0.39	K	W	0.46	1.4
	K	Mo	0.66	K	Mo	0.72	1.41
	K	Mo	0.73	K	W	0.46	1.2
	K	Mo	0.66	K	W	0.46	1.18
	Q	Mo/W	0.61	K	W	0.46	1.08
	K	Mo	0.66	Γ	W/Mo	0.92	1.20
	Q	Mo/W	0.61	Γ	W/Mo	0.92	1.10

Table A.1: Effective masses and energy gaps of HBL $MoSe_2$-WSe_2 from DFT.

with elementary charge e, effective dielectric constant ε, screening length ρ_0, and Struve and Neumann functions $H_0(x)$ and $Y_0(x)$. The binding energy was obtained as $E_b = -\min(E_n)$ from the minimal eigenvalue E_n, with $\varepsilon = 4.5$ and $\rho_0 = 1$ nm as parameters for $MoSe_2$ [183]. From DFT data we obtained the energy gaps and effective masses (in the units of free electron mass m_0) and summarized them in Tables A.1 and A.2 for HBL and HTL.

Stacking	k-point	Electron Layer	m_e (m_0)	k-point	Hole Layer	m_h (m_0)	Energy gap $E_g(eV)$
(AA)A'	K	W	0.39	K	W	0.48	1.4
	K	Mo'	0.83	K	Mo'	0.79	1.42
	K	Mo	0.82	K	Mo	0.74	1.42
	K	Mo'	0.58	K	W	0.48	1.11
	K	Mo	0.6	K	W	0.48	1.1
	K	Mo'	0.83	K	W	0.48	1.09
	K	Mo	0.82	K	W	0.48	1.08
	Q	Mo/Mo'/W	0.57	K	W	0.48	0.88
	K	Mo	0.82	Γ	Mo/Mo'/W	0.80	1.21
	Q	Mo/Mo'/W	0.57	Γ	Mo/Mo'/W	0.80	1.01
(A'B')A'	K	W	0.39	K	W	0.46	1.39
	K	Mo'	0.83	K	Mo'	0.75	1.42
	K	Mo	0.81	K	Mo	0.74	1.42
	K	Mo'	0.61	K	W	0.46	1.07
	K	Mo	0.58	K	W	0.46	1.06
	K	Mo'	0.83	K	W	0.46	1.05
	K	Mo	0.81	K	W	0.46	1.04
	Q	Mo/Mo'/W	0.53	K	W	0.46	0.83
	K	Mo	0.81	Γ	Mo/W/Mo'	0.94	1.09
	Q	Mo/Mo'/W	0.53	Γ	Mo/W/Mo'	0.94	0.88
(AB')A'	K	W	0.38	K	W	0.44	1.4
	K	Mo'	0.81	K	Mo'	0.69	1.42
	K	Mo	0.79	K	Mo	0.73	1.4
	K	Mo'	0.63	K	W	0.44	1.21
	K	Mo	0.56	K	W	0.44	1.2
	K	Mo'	0.81	K	W	0.44	1.19
	K	Mo	0.79	K	W	0.44	1.18
	Q	Mo/Mo'/W	0.55	K	W	0.44	0.95
	K	Mo	0.79	Γ	Mo/W/Mo'	0.82	1.11
	Q	Mo/Mo'/W	0.55	Γ	Mo/W/Mo'	0.82	0.89

Table A.2: Effective masses and energy gaps of HTL $MoSe_2$-WSe_2 from DFT

Appendix B

Symmetry analysis of interlayer excitons in heterobilayers

THIS CHAPTER IS BASED ON THE SUPPLEMENTARY INFORMATION OF THE ORIGINAL PUBLICATION [P2]
Förg, M., Colombier, L., Patel, R. K., Lindlau, J., Mohite, A. D., Yamaguchi, H., Glazov, M. M., Hunger, D. & Högele, A. Cavity-control of interlayer excitons in van der Waals heterostructures. *Nature Communications* **10,** 3697 (2019)

B.1 Symmetry of transition metal dichalcogenide monolayers

The real space lattice of a TMD ML crystal is shown in Figure B.1. Yellow and blue circles represent the positions of chalcogen and metal atoms, respectively.

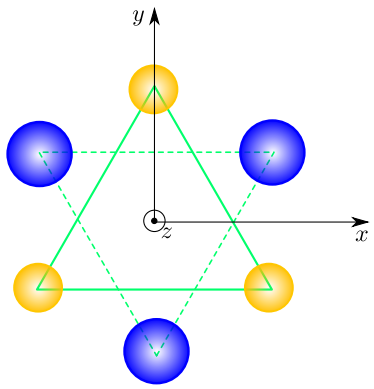

Figure B.1: Positions of atoms in the lattice of a TMD ML. Blue and yellow circles represent the positions of metal and chalcogen atoms, respectively.

To introduce the transformation rules for the wavefunctions, we follow Ref. [76] and (using $\cos 2\pi/3 = -1/2$) define the action of C_3 rotation as:

$$\psi(\boldsymbol{r}) \to D_{C_3}\psi(\boldsymbol{r}) = \psi(\boldsymbol{r}') = \psi(\hat{C}_3^{-1}\boldsymbol{r}), \quad \hat{C}_3^{-1} = \begin{pmatrix} -1/2 & \sqrt{3}/2 & 0 \\ -\sqrt{3}/2 & -1/2 & 0 \\ 0 & 0 & 1 \end{pmatrix}, \tag{B.1}$$

or

$$x' = -\frac{x}{2} - \frac{\sqrt{3}y}{2}, \quad y' = -\frac{y}{2} + \frac{\sqrt{3}x}{2}.$$

Here the operator $\hat{C}_3$ is the coordinate transformation, D_{C_3} is the function transformation. As a result, we obtain

$$D_{C_3}(x+\mathrm{i}y) = e^{\mathrm{i}\frac{2\pi}{3}}(x+\mathrm{i}y), \quad D_{C_3}(x-\mathrm{i}y) = e^{-\mathrm{i}\frac{2\pi}{3}}(x-\mathrm{i}y), \tag{B.2}$$

$$D_{C_3}(x-\mathrm{i}y)^2 = e^{\mathrm{i}\frac{2\pi}{3}}(x-\mathrm{i}y)^2, \quad D_{C_3}(x+\mathrm{i}y)^2 = e^{-\mathrm{i}\frac{2\pi}{3}}(x+\mathrm{i}y)^2,$$

in full agreement with the character table for the C_{3h} point group [76]. The positions of metal atoms, $\boldsymbol{R}_M$, and of the chalcogen atoms, $\boldsymbol{R}_X$, in the unit cell (projected on the ML plane) are given by

$$\boldsymbol{R}_M = \frac{a_0}{2}(1, 1/\sqrt{3}), \quad \boldsymbol{R}_X = \frac{a_0}{2}(1, -1/\sqrt{3}), \tag{B.3}$$

where a_0 is the lattice constant (Figure B.1). The wavevectors of the $\boldsymbol{K}_\pm$ valleys are given by

$$\boldsymbol{K}_\pm = \frac{2\pi}{a_0}(\pm 2/3, 0). \tag{B.4}$$

Thus, the transformation rules for the Bloch factors $\exp(\mathrm{i}\boldsymbol{K}_\pm\boldsymbol{R}_{M,X})$ are given by

$$D_{C_3}\exp(\mathrm{i}\boldsymbol{K}_\pm R_M) = e^{\pm\mathrm{i}\frac{2\pi}{3}}\exp(\mathrm{i}\boldsymbol{K}_\pm R_M), \tag{B.5}$$

$$D_{C_3}\exp(\mathrm{i}\boldsymbol{K}_\pm R_X) = e^{\mp\mathrm{i}\frac{2\pi}{3}}\exp(\mathrm{i}\boldsymbol{K}_\pm R_X). \tag{B.6}$$

The valence band Bloch functions in $\boldsymbol{K}_\pm$ valleys are invariant if the center of point group transformation coincides with the center of the hexagon as in Figure B.1 [184, 185]. Therefore, the atomic orbital of the metal atoms of the valence band in the $\boldsymbol{K}_+$ ($\boldsymbol{K}_-$) valley transforms as a function with an angular momentum component $+2$ (-2). The correspondence between the representations of C_{3h} point group for different origin of coordinates (relevant for one valley of TMD ML) is given in Table B.1. For simplicity we denote the representations as Γ_n (rather than K_n), where $n = 1 \ldots 12$, despite the fact that these states are relevant to the K-points of the Brillouin zone.

B.2 Symmetry of vertical transition metal dichalcogenide heterobilayers

The schematic illustration of atomic registries in vertical TMD HBLs is shown in Figure 2.3. In H-type HBL, the layers are rotated by 180° with respect to each other, while in the R-type HBLs the rotation is absent. In the following we present the symmetry analysis of electronic states in vertical TMD HBLs and address the optical selection rules without phonon-assisted processes. To illustrate the group-theory approach we focus first on AB stacking. Successively, other registries are analyzed.

The symmetry of the HBL with AB stacking (the metal atom in one layer is on top of the metal atom in the second layer) is described by the C_{3v} point symmetry group. The three fold rotation axis C_3 goes through the metals and there are three "vertical" (i.e., containing the axis) reflection planes σ_v which contain metal and chalcogen atoms. Apart from the operations described above and the identity, there are no other symmetry operations in point group for AB stacking. The horizontal reflection plane vanishes since A and B layers are different, and thus mirror-reflection axes are also absent.

In the reciprocal space, due to π-rotation of the $MoSe_2$ layer with respect to the WSe_2 layer, the Brillouin zones are also rotated by π. The $\boldsymbol{K}_+$ valley of one ML is on top of the $\boldsymbol{K}_-$ valley of the other. In first approximation, the states are not hybridized due to weak coupling between the layers. The symmetry of the valley is C_3. Indeed, the three fold rotation remains, because $2\pi/3$ rotation transforms the $\boldsymbol{K}$-point to the equivalent one. On the other hand, all reflection planes vanish as the vertical reflection transforms $\boldsymbol{K} \to -\boldsymbol{K}$.

In order to establish the representations relevant for the bands, we determine the fixed point (origin) of the point group transformations. Whereas for a ML there is a freedom of choice (one can use one of three alternatives: (a) center of hexagon, (b) metal atom, (c) chalcogen atom), the origin for the bilayer is fixed by the stacking. For the AB stacking the origin is at the metal atom. Therefore, for the AB stacking the relevant column is (b) in Tab. B.1. Thus, we have 2 $\boldsymbol{K}$-points ($\boldsymbol{K}_W - \boldsymbol{K}'_M$ and $\boldsymbol{K}'_W - \boldsymbol{K}_M$), each has two orbital CBs and two orbital CBs stemming from the corresponding bands of $MoSe_2$ and WSe_2 MLs. In C_3 point group there are just three vector representations:

$$A\,(\Gamma_1): \quad \text{conduction band orbital function (invariant)}, \tag{B.7}$$
$$E_1\,(\Gamma_2): \quad \text{valence band orbital function in } \boldsymbol{K}_W - \boldsymbol{K}'_M\ (x+iy), \tag{B.8}$$
$$E_2\,(\Gamma_3): \quad \text{valence band orbital function in } \boldsymbol{K}'_W - \boldsymbol{K}_M\ (x-iy), \tag{B.9}$$

the representations E_1 and E_2 are connected by the time-reversal. Moreover, there are just three spinor representations in C_3 point group:

$$\Gamma_4: \ (\uparrow), \quad \Gamma_5: \ (\downarrow), \quad \Gamma_6: \ (\text{either } +3/2 \text{ or } -3/2). \tag{B.10}$$

Table B.2 summarizes the representations for CB and VB states for the AB stacking. By taking into account the multiplication rules

$$\Gamma_5 \times \Gamma_4^* = \Gamma_5 \times \Gamma_5 = \Gamma_3, \quad \Gamma_4 \times \Gamma_5^* = \Gamma_4 \times \Gamma_4 = \Gamma_2, \tag{B.11}$$
$$\Gamma_5 \times \Gamma_5^* = \Gamma_4 \times \Gamma_4^* = \Gamma_4 \times \Gamma_5 = \Gamma_1,$$
$$\Gamma_6 \times \Gamma_5^* = \Gamma_6 \times \Gamma_4 = \Gamma_3, \quad \Gamma_6 \times \Gamma_4^* = \Gamma_6 \times \Gamma_5 = \Gamma_2,$$

Table B.2 allows us to establish the selection rules for the interband transitions as:

- $\boldsymbol{K}'_W - \boldsymbol{K}_M$, topmost valence band ($WSe_2$) to bottom $\uparrow$ conduction band ($MoSe_2$) — z,
- $\boldsymbol{K}'_W - \boldsymbol{K}_M$, topmost valence band ($WSe_2$) to top $\downarrow$ conduction band ($MoSe_2$) — σ^-,
- $\boldsymbol{K}_W - \boldsymbol{K}'_M$, topmost valence band ($WSe_2$) to bottom $\downarrow$ conduction band ($MoSe_2$) — z,
- $\boldsymbol{K}_W - \boldsymbol{K}'_M$, topmost valence band ($WSe_2$) to top $\uparrow$ conduction band ($MoSe_2$) — σ^+.

Other stackings are analyzed in Tabs. B.3 and B.4.

For the AA' stacking the center of point group transformations is chosen in the center of hexagon and the selection rules are:

- $\boldsymbol{K}'_W - \boldsymbol{K}_M$, topmost valence band ($WSe_2$) to bottom $\uparrow$ conduction band ($MoSe_2$) — σ^-,
- $\boldsymbol{K}'_W - \boldsymbol{K}_M$, topmost valence band ($WSe_2$) to top $\downarrow$ conduction band ($MoSe_2$) — σ^+,

- $\boldsymbol{K}_W - \boldsymbol{K}'_M$, topmost valence band ($WSe_2$) to bottom $\downarrow$ conduction band ($MoSe_2$) — σ^+,
- $\boldsymbol{K}_W - \boldsymbol{K}'_M$, topmost valence band ($WSe_2$) to top $\uparrow$ conduction band ($MoSe_2$) — σ^-.

For the A'B stacking the center of point group transformations is chosen in the chalcogen atom and the selection rules are:

- $\boldsymbol{K}'_W - \boldsymbol{K}_M$, topmost valence band ($WSe_2$) to bottom $\uparrow$ conduction band ($MoSe_2$) — σ^+,
- $\boldsymbol{K}'_W - \boldsymbol{K}_M$, topmost valence band ($WSe_2$) to top $\downarrow$ conduction band ($MoSe_2$) — z,
- $\boldsymbol{K}_W - \boldsymbol{K}'_M$, topmost valence band ($WSe_2$) to bottom $\downarrow$ conduction band ($MoSe_2$) — σ^-,
- $\boldsymbol{K}_W - \boldsymbol{K}'_M$, topmost valence band ($WSe_2$) to top $\uparrow$ conduction band ($MoSe_2$) — z.

In the R-type stacking the point group symmetry is the same C_{3v}. For the AA case the rotation center should be chosen as the center of hexagon. Correspondingly,

- $\boldsymbol{K}_W - \boldsymbol{K}_M$, topmost valence band ($WSe_2$) to bottom $\uparrow$ conduction band ($MoSe_2$) — σ^+,
- $\boldsymbol{K}_W - \boldsymbol{K}_M$, topmost valence band ($WSe_2$) to top $\downarrow$ conduction band ($MoSe_2$) — z,
- $\boldsymbol{K}'_W - \boldsymbol{K}'_M$, topmost valence band ($WSe_2$) to bottom $\downarrow$ conduction band ($MoSe_2$) — σ^-,
- $\boldsymbol{K}'_W - \boldsymbol{K}'_M$, topmost valence band ($WSe_2$) to top $\uparrow$ conduction band ($MoSe_2$) — z.

For the AB' case the centers of hexagon in the W-based ML (hole layer) correspond to the metals Mo in the electron layer. Thus, the rotation center can be chosen as the metal atom in the W-based layer and the chalcogen atom in the Mo-based layer:

- $\boldsymbol{K}_W - \boldsymbol{K}_M$, topmost valence band ($WSe_2$) to bottom $\uparrow$ conduction band ($MoSe_2$) — z,

- $\boldsymbol{K}_W - \boldsymbol{K}_M$, topmost valence band ($WSe_2$) to top $\downarrow$ conduction band ($MoSe_2$) — σ^-,
- $\boldsymbol{K}'_W - \boldsymbol{K}'_M$, topmost valence band ($WSe_2$) to bottom $\downarrow$ conduction band ($MoSe_2$) — z,
- $\boldsymbol{K}'_W - \boldsymbol{K}'_M$, topmost valence band ($WSe_2$) to top $\uparrow$ conduction band ($MoSe_2$) — σ^+.

For the A'B' case the centers of hexagon in the W-based ML (hole layer) correspond to the dichalcogenides Se in the electron layer. Thus, the rotation center can be chosen as the chalcogen atom in the W-based layer and the metal atom in the Mo-based layer:

- $\boldsymbol{K}_W - \boldsymbol{K}_M$, topmost valence band ($WSe_2$) to bottom $\uparrow$ conduction band ($MoSe_2$) — σ^-,
- $\boldsymbol{K}_W - \boldsymbol{K}_M$, topmost valence band ($WSe_2$) to top $\downarrow$ conduction band ($MoSe_2$) — σ^+,
- $\boldsymbol{K}'_W - \boldsymbol{K}'_M$, topmost valence band ($WSe_2$) to bottom $\downarrow$ conduction band ($MoSe_2$) — σ^+,
- $\boldsymbol{K}'_W - \boldsymbol{K}'_M$, topmost valence band ($WSe_2$) to top $\uparrow$ conduction band ($MoSe_2$) — σ^-.

According to the D_{3d} point group which describes A'B $MoSe_2$-WSe_2 HBLs symmetries, only three spinor representations exist for the energy bands: Γ_6 for the top most WSe_2 VB, Γ_6 for the top $MoSe_2$ CB and Γ_5 (Γ_4) for the bottom $MoSe_2$ CB in the $K_M(K'_M)$ valley. These band symmetries determine the selection rules of the momentum-allowed transitions shown in Figure 2.7. All other band symmetries are summarized in Figure 2.7 and Figure 2.8 for H-type and R-type stacking respectively.

valley	band	(a) hexagon	(b) metal	(c) chalcogen
$\boldsymbol{K}_+$	valence	Γ_1	Γ_3	Γ_2
	conduction	Γ_2	Γ_1	Γ_3
$\boldsymbol{K}_-$	valence	Γ_1	Γ_2	Γ_3
	conduction	Γ_3	Γ_1	Γ_2
$\boldsymbol{K}_+$	valence $\uparrow$	Γ_7	Γ_{10}	Γ_{11}
	conduction $\uparrow$	Γ_{11}	Γ_7	Γ_{10}
	conduction $\downarrow$	Γ_9	Γ_8	Γ_{12}
$\boldsymbol{K}_-$	valence $\downarrow$	Γ_8	Γ_9	Γ_{12}
	conduction $\downarrow$	Γ_{12}	Γ_8	Γ_9
	conduction $\uparrow$	Γ_{10}	Γ_7	Γ_{11}

Table B.1: Correspondence between the representations of the C_{3h} point groups relevant for $\boldsymbol{K}_\pm$ in ML TMD. Both vector and spinor representations are given, $\uparrow$ and $\downarrow$ denote the spin-up $|1/2, +1/2\rangle$ and spin-down $|1/2, -1/2\rangle$ states. Only the topmost valence band ($\uparrow$ in $\boldsymbol{K}_+$ valley and $\downarrow$ in $\boldsymbol{K}_-$ valley) are relevant.

valley	band	representation
$\boldsymbol{K}'_W - \boldsymbol{K}_M$	valence	Γ_2
	conduction	Γ_1
$\boldsymbol{K}_W - \boldsymbol{K}'_M$	valence	Γ_3
	conduction	Γ_1
$\boldsymbol{K}'_W - \boldsymbol{K}_M$	valence $\downarrow$	Γ_4
	conduction $\uparrow$	Γ_4
	conduction $\downarrow$	Γ_5
$\boldsymbol{K}_W - \boldsymbol{K}'_M$	valence $\uparrow$	Γ_5
	conduction $\downarrow$	Γ_5
	conduction $\uparrow$	Γ_4

Table B.2: Symmetries of bands in $\boldsymbol{K}_W - \boldsymbol{K}'_M$ and $\boldsymbol{K}'_W - \boldsymbol{K}_M$ points of HBL with AB stacking.

valley	band	representation
$\boldsymbol{K}'_W - \boldsymbol{K}_M$	valence	Γ_1
	conduction	Γ_2
$\boldsymbol{K}_W - \boldsymbol{K}'_M$	valence	Γ_1
	conduction	Γ_3
$\boldsymbol{K}'_W - \boldsymbol{K}_M$	valence $\downarrow$	Γ_5
	conduction $\uparrow$	Γ_6
	conduction $\downarrow$	Γ_4
$\boldsymbol{K}_W - \boldsymbol{K}'_M$	valence $\uparrow$	Γ_4
	conduction $\downarrow$	Γ_6
	conduction $\uparrow$	Γ_5

Table B.3: Symmetries of bands in $\boldsymbol{K}_W - \boldsymbol{K}'_M$ and $\boldsymbol{K}'_W - \boldsymbol{K}_M$ points of HBL with AA' stacking (centers of hexagons coincide in the MLs).

valley	band	representation
$\boldsymbol{K}'_W - \boldsymbol{K}_M$	valence	Γ_2
	conduction	Γ_2
$\boldsymbol{K}_W - \boldsymbol{K}'_M$	valence	Γ_3
	conduction	Γ_3
$\boldsymbol{K}'_W - \boldsymbol{K}_M$	valence $\downarrow$	Γ_6
	conduction $\uparrow$	Γ_4
	conduction $\downarrow$	Γ_6
$\boldsymbol{K}_W - \boldsymbol{K}'_M$	valence $\uparrow$	Γ_6
	conduction $\downarrow$	Γ_5
	conduction $\uparrow$	Γ_6

Table B.4: Symmetries of bands in $\boldsymbol{K}_W - \boldsymbol{K}'_M$ and $\boldsymbol{K}'_W - \boldsymbol{K}_M$ points of HBL with A'B stacking (chalcogenes coincide).

valley	band	representation
$\boldsymbol{K}_W - \boldsymbol{K}_M$	valence	Γ_1
	conduction	Γ_2
$\boldsymbol{K}_W - \boldsymbol{K}_M$	valence	Γ_1
	conduction	Γ_3
$\boldsymbol{K}_W - \boldsymbol{K}_M$	valence $\uparrow$	Γ_4
	conduction $\uparrow$	Γ_6
	conduction $\downarrow$	Γ_4
$\boldsymbol{K}'_W - \boldsymbol{K}'_M$	valence $\downarrow$	Γ_5
	conduction $\downarrow$	Γ_6
	conduction $\uparrow$	Γ_5

Table B.5: Symmetries of bands in $\boldsymbol{K}_W - \boldsymbol{K}_M$ and $\boldsymbol{K}'_W - \boldsymbol{K}'_M$ points of HBL with AA stacking (centers of hexagons coincide).

valley	band	representation
$\boldsymbol{K}_W - \boldsymbol{K}_M$	valence	Γ_3
	conduction	Γ_3
$\boldsymbol{K}_W - \boldsymbol{K}_M$	valence	Γ_2
	conduction	Γ_2
$\boldsymbol{K}_W - \boldsymbol{K}_M$	valence $\uparrow$	Γ_5
	conduction $\uparrow$	Γ_5
	conduction $\downarrow$	Γ_6
$\boldsymbol{K}'_W - \boldsymbol{K}'_M$	valence $\downarrow$	Γ_4
	conduction $\downarrow$	Γ_4
	conduction $\uparrow$	Γ_6

Table B.6: Symmetries of bands in $\boldsymbol{K}_W - \boldsymbol{K}_M$ and $\boldsymbol{K}'_W - \boldsymbol{K}'_M$ points of HBL with AB' stacking.

valley	band	representation
$\boldsymbol{K}_W - \boldsymbol{K}_M$	valence	Γ_2
	conduction	Γ_1
$\boldsymbol{K}_W - \boldsymbol{K}_M$	valence	Γ_3
	conduction	Γ_1
$\boldsymbol{K}_W - \boldsymbol{K}_M$	valence $\uparrow$	Γ_6
	conduction $\uparrow$	Γ_4
	conduction $\downarrow$	Γ_5
$\boldsymbol{K}'_W - \boldsymbol{K}'_M$	valence $\downarrow$	Γ_6
	conduction $\downarrow$	Γ_5
	conduction $\uparrow$	Γ_4

Table B.7: Symmetries of bands in $\boldsymbol{K}_W - \boldsymbol{K}_M$ and $\boldsymbol{K}'_W - \boldsymbol{K}'_M$ points of HBL with A'B' stacking.

Bibliography

1. Abbott, E. A. Flatland: A Romance of Many Dimensions (Seeley, 1884).
2. Novoselov, K. S., Geim, A. K., Morozov, S. V., *et al.* Electric Field Effect in Atomically Thin Carbon Films. *Science* **306,** 666–669 (2004).
3. Novoselov, K. S. Nobel Lecture: Graphene: Materials in the Flatland. *Rev. Mod. Phys.* **83,** 837–849 (2011).
4. Dean, C. R., Young, A. F., Meric, I., *et al.* Boron nitride substrates for high-quality graphene electronics. *Nat. Nanotechnol.* **5,** 722–726 (2010).
5. Ziletti, A., Carvalho, A., Trevisanutto, P. E., *et al.* Phosphorene oxides: Bandgap engineering of phosphorene by oxidation. *Phys. Rev. B* **91,** 085407 (2015).
6. Wang, Q. H., Kalantar-Zadeh, K., Kis, A., *et al.* Electronics and optoelectronics of two-dimensional transition metal dichalcogenides. *Nat. Nanotechnol.* **7,** 699–712 (2012).
7. Gibertini, M., Koperski, M., Morpurgo, A. F., *et al.* Magnetic 2D materials and heterostructures. *Nat. Nanotechnol.* **14,** 408–419 (2019).
8. Cui, C., Xue, F., Hu, W.-J., *et al.* Two-dimensional materials with piezoelectric and ferroelectric functionalities. *NPJ 2D Mater. Appl.* **2,** 1–14 (2018).
9. Huang, Y., Sutter, E., Shi, N. N., *et al.* Reliable Exfoliation of Large-Area High-Quality Flakes of Graphene and Other Two-Dimensional Materials. *ACS Nano* **9,** 10612–10620 (2015).
10. Geim, A. K. & Grigorieva, I. V. Van der Waals heterostructures. *Nature* **499,** 419–425 (2013).
11. Bonaccorso, F., Colombo, L., Yu, G., *et al.* Graphene, related two-dimensional crystals, and hybrid systems for energy conversion and storage. *Science* **347** (2015).
12. Novoselov, K. S., Mishchenko, A., Carvalho, A., *et al.* 2D materials and van der Waals heterostructures. *Science* **353** (2016).

13. Zhu, Z. Y., Cheng, Y. C. & Schwingenschlögl, U. Giant spin-orbit-induced spin splitting in two-dimensional transition-metal dichalcogenide semiconductors. *Phys. Rev. B* **84,** 153402 (2011).

14. Berkelbach, T. C., Hybertsen, M. S. & Reichman, D. R. Theory of neutral and charged excitons in monolayer transition metal dichalcogenides. *Phys. Rev. B* **88,** 045318 (2013).

15. Wang, Z., Chiu, Y.-H., Honz, K., *et al.* Electrical Tuning of Interlayer Exciton Gases in WSe_2 Bilayers. *Nano Lett.* **18,** 137–143 (2018).

16. Yao, W., Xiao, D. & Niu, Q. Valley-dependent optoelectronics from inversion symmetry breaking. *Phys. Rev. B* **77,** 235406 (2008).

17. Xiao, D., Liu, G.-B., Feng, W., *et al.* Coupled Spin and Valley Physics in Monolayers of MoS_2 and Other Group-VI Dichalcogenides. *Phys. Rev. Lett.* **108,** 196802 (2012).

18. Kang, J., Tongay, S., Zhou, J., *et al.* Band offsets and heterostructures of two-dimensional semiconductors. *Appl. Phys. Lett.* **102,** 012111 (2013).

19. Rivera, P., John R., S., Jones, A. M., *et al.* Observation of long-lived interlayer excitons in monolayer $MoSe_2$–WSe_2 heterostructures. *Nat. Commun.* **6,** 6242 (2015).

20. Miller, B., Steinhoff, A., Pano, B., *et al.* Long-Lived Direct and Indirect Interlayer Excitons in van der Waals Heterostructures. *Nano Lett.* **17,** 5229–5237 (2017).

21. Nagler, P., Ballottin, M. V., Mitioglu, A. A., *et al.* Giant magnetic splitting inducing near-unity valley polarization in van der Waals heterostructures. *Nat. Commun.* **8,** 1–6 (2017).

22. Rivera, P., Yu, H., Seyler, K. L., *et al.* Interlayer valley excitons in heterobilayers of transition metal dichalcogenides. *Nat. Nanotechnol.* **13,** 1004 (2018).

23. Fogler, M. M., Butov, L. V. & Novoselov, K. S. High-temperature superfluidity with indirect excitons in van der Waals heterostructures. *Nat. Commun.* **5,** ncomms5555 (2014).

24. Rivera, P., Seyler, K. L., Yu, H., *et al.* Valley-polarized exciton dynamics in a 2D semiconductor heterostructure. *Science* **351,** 688–691 (2016).

25. Ciarrocchi, A., Unuchek, D., Avsar, A., *et al.* Polarization switching and electrical control of interlayer excitons in two-dimensional van der Waals heterostructures. *Nat. Photonics* **13,** 131 (2019).

26. Jiang, C., Xu, W., Rasmita, A., *et al.* Microsecond dark-exciton valley polarization memory in two-dimensional heterostructures. *Nat. Commun.* **9,** 753 (2018).

27. Wang, Y., Wang, Z., Yao, W., *et al.* Interlayer coupling in commensurate and incommensurate bilayer structures of transition-metal dichalcogenides. *Phys. Rev. B* **95,** 115429 (2017).

28. Hsu, W.-T., Lin, B.-H., Lu, L.-S., *et al.* Tailoring excitonic states of van der Waals bilayers through stacking configuration, band alignment, and valley spin. *Sci. Adv.* **5,** eaax7407 (2019).

29. Gong, Y., Lei, S., Ye, G., *et al.* Two-step growth of two-dimensional WSe_2/$MoSe_2$ heterostructures. *Nano Lett.* **15,** 6135–6141 (2015).

30. Hsu, W.-T., Lu, L.-S., Wu, P.-H., *et al.* Negative circular polarization emissions from WSe_2 /$MoSe_2$ commensurate heterobilayers. *Nat. Commun.* **9,** 1–7 (2018).

31. Yu, H., Liu, G.-B., Tang, J., *et al.* Moiré excitons: From programmable quantum emitter arrays to spin-orbit–coupled artificial lattices. *Sci. Adv.* **3,** e1701696 (2017).

32. Regan, E. C., Wang, D., Jin, C., *et al.* Mott and generalized Wigner crystal states in WSe_2 /WS_2 moiré superlattices. *Nature* **579,** 359–363 (2020).

33. Tang, Y., Li, L., Li, T., *et al.* Simulation of Hubbard model physics in WSe_2 /WS_2 moiré superlattices. *Nature* **579,** 353–358 (2020).

34. Schneider, C., Glazov, M. M., Korn, T., *et al.* Two-dimensional semiconductors in the regime of strong light-matter coupling. *Nat. Commun.* **9,** 2695 (2018).

35. Liu, X., Galfsky, T., Sun, Z., *et al.* Strong light-matter coupling in two-dimensional atomic crystals. *Nat. Photonics* **9,** 30–34 (2015).

36. Flatten, L. C., He, Z., Coles, D. M., *et al.* Room-temperature exciton-polaritons with two-dimensional WS_2. *Sci Rep* **6** (2016).

37. Lundt, N., Klembt, S., Cherotchenko, E., *et al.* Room-temperature Tamm-plasmon exciton-polaritons with a WSe_2 monolayer. *Nat. Commun.* **7** (2016).

38. Sidler, M., Back, P., Cotlet, O., *et al.* Fermi polaron-polaritons in charge-tunable atomically thin semiconductors. *Nat. Phys.* **13,** 255–261 (2017).

39. Qian, X., Liu, J., Fu, L., *et al.* Quantum spin Hall effect in two-dimensional transition metal dichalcogenides. *Science* **346,** 1344–1347 (2014).

40. Najmaei, S., Liu, Z., Zhou, W., *et al.* Vapour phase growth and grain boundary structure of molybdenum disulphide atomic layers. *Nat. Mater.* **12,** 754–759 (2013).

41. Zhang, Y., Chang, T.-R., Zhou, B., *et al.* Direct observation of the transition from indirect to direct bandgap in atomically thin epitaxial $MoSe_2$. *Nat. Nanotechnol.* **9,** 111–115 (2014).

42. Zhang, X., Qiao, X.-F., Shi, W., *et al.* Phonon and Raman scattering of two-dimensional transition metal dichalcogenides from monolayer, multilayer to bulk material. *Chem. Soc. Rev.* **44,** 2757–2785 (2015).

43. Jin, Z., Li, X., Mullen, J. T., *et al.* Intrinsic transport properties of electrons and holes in monolayer transition-metal dichalcogenides. *Phys. Rev. B* **90,** 045422 (2014).

44. Luo, X., Zhao, Y., Zhang, J., *et al.* Anomalous frequency trends in MoS_2 thin films attributed to surface effects. *Phys. Rev. B* **88,** 075320 (2013).

45. Lui, C. H., Ye, Z., Ji, C., *et al.* Observation of interlayer phonon modes in van der Waals heterostructures. *Phys. Rev. B* **91,** 165403 (2015).

46. Lu, X., Luo, X., Zhang, J., *et al.* Lattice vibrations and Raman scattering in two-dimensional layered materials beyond graphene. *Nano Res.* **9,** 3559–3597 (2016).

47. Liu, G.-B., Shan, W.-Y., Yao, Y., *et al.* Three-band tight-binding model for monolayers of group-VIB transition metal dichalcogenides. *Phys. Rev. B* **88,** 085433 (2013).

48. Kośmider, K., González, J. W. & Fernández-Rossier, J. Large spin splitting in the conduction band of transition metal dichalcogenide monolayers. *Phys. Rev. B* **88** (2013).

49. Kormányos, A., Burkard, G., Gmitra, M., *et al.* Corrigendum: k.p theory for two-dimensional transition metal dichalcogenide semiconductors. *2D Mater.* **2,** 049501 (2015).

50. Zhao, W., Ribeiro, R. M., Toh, M., *et al.* Origin of Indirect Optical Transitions in Few-Layer MoS_2, WS_2, and WSe_2. *Nano Lett.* **13,** 5627–5634 (2013).

51. Zhang, C., Chen, Y., Johnson, A., *et al.* Probing Critical Point Energies of Transition Metal Dichalcogenides: Surprising Indirect Gap of Single Layer WSe_2. *Nano Lett.* **15,** 6494–6500 (2015).

52. Wang, G., Chernikov, A., Glazov, M. M., *et al.* Colloquium: Excitons in atomically thin transition metal dichalcogenides. *Rev. Mod. Phys.* **90,** 021001 (2018).

53. Wang, G., Robert, C., Glazov, M. M., *et al.* In-plane propagation of light in transition metal dichalcogenide monolayers: optical selection rules. *Phys. Rev. Lett.* **119,** 047401 (2017).

54. Molas, M. R., Nogajewski, K., Slobodeniuk, A. O., *et al.* Optical response of monolayer, few-layer and bulk tungsten disulfide. *arXiv preprint.* arXiv: 1706.09285 (2017).

55. Zhang, X.-X., Cao, T., Lu, Z., *et al.* Magnetic brightening and control of dark excitons in monolayer WSe_2. *Nat. Nanotechnol.* **12,** 883–888 (2017).

56. He, J., Hummer, K. & Franchini, C. Stacking effects on the electronic and optical properties of bilayer transition metal dichalcogenides MoS_2, $MoSe_2$, WS_2, and WSe_2. *Phys. Rev. B* **89,** 075409 (2014).

57. Constantinescu, G., Kuc, A. & Heine, T. Stacking in Bulk and Bilayer Hexagonal Boron Nitride. *Phys. Rev. Lett.* **111,** 036104 (2013).

58. Lebedev, A. V., Lebedeva, I. V., Knizhnik, A. A., *et al.* Interlayer interaction and related properties of bilayer hexagonal boron nitride: ab initio study. *RSC Adv.* **6,** 6423–6435 (2016).

59. Alexeev, E. M., Ruiz-Tijerina, D. A., Danovich, M., *et al.* Resonantly hybridized excitons in moiré superlattices in van der Waals heterostructures. *Nature* **567,** 81–86 (2019).

60. Zhang, C., Gong, C., Nie, Y., *et al.* Systematic study of electronic structure and band alignment of monolayer transition metal dichalcogenides in Van der Waals heterostructures. *2D Mater.* **4,** 015026 (2016).

61. Jin, C., Ma, E. Y., Karni, O., *et al.* Ultrafast dynamics in van der Waals heterostructures. *Nat. Nanotechnol.* **13,** 994–1003 (2018).

62. Gillen, R. & Maultzsch, J. Interlayer excitons in $MoSe_2$/WSe_2 heterostructures from first principles. *Phys. Rev. B* **97,** 165306 (2018).

63. Komsa, H.-P. & Krasheninnikov, A. V. Electronic structures and optical properties of realistic transition metal dichalcogenide heterostructures from first principles. *Phys. Rev. B* **88,** 085318 (2013).

64. Torun, E., Miranda, H. P. C., Molina-Sánchez, A., *et al.* Interlayer and intralayer excitons in MoS_2/WS_2 and $MoSe_2/WSe_2$ heterobilayers. *Phys. Rev. B* **97,** 245427 (2018).

65. Csonka, G. I., Perdew, J. P., Ruzsinszky, A., *et al.* Assessing the performance of recent density functionals for bulk solids. *Phys. Rev. B* **79,** 155107 (2009).

66. Shishkin, M. & Kresse, G. Self-consistent GW calculations for semiconductors and insulators. *Phys. Rev. B* **75,** 235102 (2007).

67. Grimme, S., Antony, J., Ehrlich, S., *et al.* A consistent and accurate ab initio parametrization of density functional dispersion correction (DFT-D) for the 94 elements H-Pu. *J. Chem. Phys.* **132,** 154104 (2010).

68. Grimme, S., Ehrlich, S. & Goerigk, L. Effect of the damping function in dispersion corrected density functional theory. *J. Comput. Chem.* **32,** 1456–1465 (2011).

69. Berghäuser, G. & Malic, E. Analytical approach to excitonic properties of MoS_2. *Phys. Rev. B* **89,** 125309 (2014).

70. Deilmann, T. & Thygesen, K. S. Finite-momentum exciton landscape in mono- and bilayer transition metal dichalcogenides. *2D Mater.* **6,** 035003 (2019).

71. Roth, L. M., Lax, B. & Zwerdling, S. Theory of Optical Magneto-Absorption Effects in Semiconductors. *Phys. Rev.* **114,** 90–104 (1959).

72. Bir, G. L. & Pikus, G. E. Symmetry and Strain-Induced Effects in Semiconductors (Wiley New York, 1974).

73. Xiao, D., Chang, M.-C. & Niu, Q. Berry phase effects on electronic properties. *Rev. Mod. Phys.* **82,** 1959–2007 (2010).

74. Wang, G., Bouet, L., Glazov, M., *et al.* Magneto-optics in transition metal diselenide monolayers. *2D Mater.* **2,** 034002 (2015).

75. Berry, M. V. Quantal phase factors accompanying adiabatic changes. *Proc. R. Soc. A* **392,** 45–57 (1984).

76. Koster, G. F. Properties of the Thirty-Two Point Groups (The MIT Press, 1963).

77. Glazov, M. M., Amand, T., Marie, X., *et al.* Exciton fine structure and spin decoherence in monolayers of transition metal dichalcogenides. *Phys. Rev. B* **89,** 201302 (2014).

78. Yu, H., Liu, G.-B. & Yao, W. Brightened spin-triplet interlayer excitons and optical selection rules in van der Waals heterobilayers. *2D Mater.* **5,** 035021 (2018).

79. Lopes dos Santos, J. M. B., Peres, N. M. R. & Castro Neto, A. H. Graphene Bilayer with a Twist: Electronic Structure. *Phys. Rev. Lett.* **99,** 256802 (2007).

80. Hermann, K. Periodic overlayers and moiré patterns: theoretical studies of geometric properties. *J. Phys.: Condens. Matter* **24,** 314210 (2012).

81. Carr, S., Massatt, D., Torrisi, S. B., *et al.* Relaxation and domain formation in incommensurate two-dimensional heterostructures. *Phys. Rev. B* **98,** 224102 (2018).

82. Enaldiev, V. V., Zólyomi, V., Yelgel, C., *et al.* Stacking domains and dislocation networks in marginally twisted bilayers of transition metal dichalcogenides. *arXiv preprint.* arXiv: 1911.12804 (2019).

83. Weston, A., Zou, Y., Enaldiev, V., *et al.* Atomic reconstruction in twisted bilayers of transition metal dichalcogenides. *arXiv preprint.* arXiv: 1911.12664 (2019).

84. Urbaszek, B. & Srivastava, A. Materials in flatland twist and shine. *Nature* **567,** 39 (2019).

85. Tran, K., Moody, G., Wu, F., *et al.* Evidence for moiré excitons in van der Waals heterostructures. *Nature* **567,** 71 (2019).

86. Seyler, K. L., Rivera, P., Yu, H., *et al.* Signatures of moiré-trapped valley excitons in $MoSe_2$ /WSe_2 heterobilayers. *Nature* **567,** 66 (2019).

87. Jin, C., Regan, E. C., Yan, A., *et al.* Observation of moiré excitons in WSe_2 /WS_2 heterostructure superlattices. *Nature* **567,** 76 (2019).

88. Shimazaki, Y., Schwartz, I., Watanabe, K., *et al.* Strongly correlated electrons and hybrid excitons in a moiré heterostructure. *Nature,* 1–6 (2020).

89. Wang, L., Shih, E.-M., Ghiotto, A., *et al.* Magic continuum in twisted bilayer WSe_2. *arXiv preprint.* arXiv: 1910.12147 (2019).

90. Fabry, C. & Perot, A. Théorie et applications d'une nouvelle méthode de spectroscopie interférentielle. *Annales de Chimie et de Physique, 7. Série* **16** (1899).

91. Saleh, B. E. A. & Teich, M. C. Fundamentals of Photonics (ed Goodman, J. W.) (John Wiley & Sons, Inc., 1991).

92. Zinth, W. & Zinth, U. Optik: Lichtstrahlen – Wellen – Photonen (De Gruyter, 2018).

93. Hodgson, N. & Weber, H. Optical Resonators: Fundamentals, Advanced Concepts, Applications (Springer Science & Business Media, 2005).

94. Benedikter, J., Hümmer, T., Mader, M., *et al.* Transverse-mode coupling and diffraction loss in tunable Fabry–Pérot microcavities. *New J. Phys.* **17,** 053051 (2015).

95. Gagliardi, G. & Loock, H.-P. Cavity-Enhanced Spectroscopy and Sensing (Springer Berlin Heidelberg, 2014).

96. Hunger, D., Steinmetz, T., Colombe, Y., *et al.* A fiber Fabry–Perot cavity with high finesse. *New J. Phys.* **12,** 065038 (2010).

97. Mader, M., Reichel, J., Hänsch, T. W., *et al.* A scanning cavity microscope. *Nat. Commun.* **6,** 7249 (2015).

98. Benedikter, J., Moosmayer, T., Mader, M., *et al.* Transverse-mode coupling effects in scanning cavity microscopy. *New J. Phys.* **21,** 103029 (2019).

99. Loudon, R. The Quantum Theory of Light 3rd ed (Oxford University Press, 2000).

100. Scully, M. O. & Zubairy, M. S. Quantum Optics (Cambridge University Press, 1997).

101. Hinds, E. in *Advances in Atomic, Molecular, and Optical Physics* 237–289 (Elsevier, 1990).

102. Purcell, E. M. Spontaneous emission probabilities at radio frequencies. *Phys. Rev.* **69,** 681 (1946).

103. Auffèves, A., Gerace, D., Gérard, J.-M., *et al.* Controlling the dynamics of a coupled atom-cavity system by pure dephasing. *Phys. Rev. B* **81** (2010).

104. Shore, B. W. & Knight, P. L. The jaynes-cummings model. *Journal of Modern Optics* **40,** 1195–1238 (1993).

105. Pau, S., Björk, G., Cao, H., *et al.* Theory of inhomogeneous microcavity polariton splitting. *Solid State Commun.* **98,** 781–784 (1996).

106. Henschel, K., Majer, J., Schmiedmayer, J., *et al.* Cavity QED with an ultracold ensemble on a chip: Prospects for strong magnetic coupling at finite temperatures. *Phys. Rev. A* **82** (2010).

107. Savona, V., Andreani, L. C., Schwendimann, P., *et al.* Quantum well excitons in semiconductor microcavities: unified treatment of weak and strong coupling regimes. *Solid State Commun.* **93,** 733–739 (1995).

108. Besga, B., Vaneph, C., Reichel, J., *et al.* Polariton Boxes in a Tunable Fiber Cavity. *Phys. Rev. Appl.* **3,** 014008 (2015).

109. Panzarini, G., Andreani, L. C., Armitage, A., *et al.* Exciton-light coupling in single and coupled semiconductor microcavities: Polariton dispersion and polarization splitting. *Phys. Rev. B* **59,** 5082 (1999).

110. Neumann, A., Lindlau, J., Colombier, L., *et al.* Opto-valleytronic imaging of atomically thin semiconductors. *Nat. Nanotechnol.* **12,** 329–334 (2017).

111. Hunger, D., Steinmetz, T., Colombe, Y., *et al.* A fiber fabry-perot cavity with high finesse. *New J. Phys.* **12,** 065038 (2010).

112. Fang, H. H., Han, B., Robert, C., *et al.* Control of the Exciton Radiative Lifetime in van der Waals Heterostructures. *Phys. Rev. Lett.* **123,** 067401 (2019).

113. Furman, S. A. & Tikhonravov, A. Basics of Optics of Multilayer Systems (Atlantica Séguier Frontieres, 1992).

114. Gong, Y., Lin, J., Wang, X., *et al.* Vertical and in-plane heterostructures from WS_2/MoS_2 monolayers. *Nat. Mater.* **13,** 1135–1142 (2014).

115. Li, M.-Y., Shi, Y., Cheng, C.-C., *et al.* Epitaxial growth of a monolayer WSe_2-MoS_2 lateral p-n junction with an atomically sharp interface. *Science* **349,** 524–528 (2015).

116. Kang, J., Li, J., Li, S.-S., *et al.* Electronic structural moiré pattern effects on MoS_2/$MoSe_2$ 2D heterostructures. *Nano Lett.* **13,** 5485–5490 (2013).

117. Tong, Q., Yu, H., Zhu, Q., *et al.* Topological mosaics in moire superlattices of van der Waals heterobilayers. *Nat. Phys.* **13,** 356–362 (2016).

118. Zhang, C., Chuu, C.-P., Ren, X., *et al.* Interlayer couplings, Moiré patterns, and 2D electronic superlattices in MoS_2/WSe_2 hetero-bilayers. *Sci. Adv.* **3,** e1601459 (2017).

119. Wu, F., Lovorn, T. & MacDonald, A. H. Topological exciton bands in moiré heterojunctions. *Phys. Rev. Lett.* **118,** 147401 (2017).

120. Wu, F., Lovorn, T. & MacDonald, A. Theory of optical absorption by interlayer excitons in transition metal dichalcogenide heterobilayers. *Phys. Rev. B* **97,** 035306 (2018).

121. Yu, H., Wang, Y., Tong, Q., *et al.* Anomalous Light Cones and Valley Optical Selection Rules of Interlayer Excitons in Twisted Heterobilayers. *Phys. Rev. Lett.* **115,** 187002 (2015).

122. Castellanos-Gomez, A., Buscema, M., Molenaar, R., *et al.* Deterministic transfer of two-dimensional materials by all-dry viscoelastic stamping. *2D Mater.* **1,** 011002 (2014).

123. Cadiz, F., Courtade, E., Robert, C., *et al.* Excitonic linewidth approaching the homogeneous limit in MoS_2 based van der Waals heterostructures : accessing spin-valley dynamics. *Phys. Rev. X* **7** (2017).

124. Ajayi, O. A., Ardelean, J. V., Shepard, G. D., *et al.* Approaching the intrinsic photoluminescence linewidth in transition metal dichalcogenide monolayers. *2D Mater.* **4,** 031011– (2017).

125. Wierzbowski, J., Klein, J., Sigger, F., *et al.* Direct exciton emission from atomically thin transition metal dichalcogenide heterostructures near the lifetime limit. *Sci. Rep.* **7,** 12383– (2017).

126. Pizzocchero, F., Gammelgaard, L., Jessen, B. S., *et al.* The hot pick-up technique for batch assembly of van der Waals heterostructures. *Nat. Commun.* **7,** 1–10 (2016).

127. Mak, K. F., He, K., Shan, J., *et al.* Control of valley polarization in monolayer MoS_2 by optical helicity. *Nat. Nanotechnol.* **7,** 494–498 (2012).

128. Zhu, B., Zeng, H., Dai, J., *et al.* Anomalously robust valley polarization and valley coherence in bilayer WS_2. *PNAS* **111,** 11606–11611 (2014).

129. Amin, B., P. Kaloni, T. & Schwingenschlögl, U. Strain engineering of WS_2 , WSe_2 , and WTe_2. *RSC Advances* **4,** 34561–34565 (2014).

130. Li, Y., Rao, Y., Mak, K. F., *et al.* Probing Symmetry Properties of Few-Layer MoS_2 and h-BN by Optical Second-Harmonic Generation. *Nano Lett.* **13,** 3329–3333 (2013).

131. Hsu, W.-T., Zhao, Z.-A., Li, L.-J., *et al.* Second Harmonic Generation from Artificially Stacked Transition Metal Dichalcogenide Twisted Bilayers. *ACS Nano* **8,** 2951–2958 (2014).

132. Ross, J. S., Wu, S., Yu, H., *et al.* Electrical control of neutral and charged excitons in a monolayer semiconductor. *Nat. Commun.* **4,** 1474 (2013).

133. Jiang, C., Liu, F., Cuadra, J., *et al.* Zeeman splitting via spin-valley-layer coupling in bilayer $MoTe_2$. *Nat. Commun.* **8,** 802 (2017).

134. Nagler, P., Plechinger, G., Ballotin, M., *et al.* Interlayer exciton dynamics in a dichalcogenide monolayer heterostructure. *2D Mater.* (2017).

135. Hill, H. M., Rigosi, A. F., Roquelet, C., *et al.* Observation of Excitonic Rydberg States in Monolayer MoS_2 and WS_2 by Photoluminescence Excitation Spectroscopy. *Nano Lett.* **15,** 2992–2997 (2015).

136. Li, Y., Chernikov, A., Zhang, X., *et al.* Measurement of the optical dielectric function of monolayer transition-metal Dichalcogenides:MoS_2, $MoSe_2$, WS_2 and WSe_2. *Phys. Rev. B* **90,** 205422 (2014).

137. Rigosi, A. F., Hill, H. M., Li, Y., *et al.* Probing Interlayer Interactions in Transition Metal Dichalcogenide Heterostructures by Optical Spectroscopy: MoS_2/WS_2 and $MoSe_2$/WSe_2. *Nano Lett.* **15,** 5033–5038 (2015).

138. Xu, X., Yao, W., Xiao, D., *et al.* Spin and pseudospins in layered transition metal dichalcogenides. *Nat. Phys.* **10,** 343–350 (2014).

139. Jones, A. M., Yu, H., Ghimire, N. J., *et al.* Optical generation of excitonic valley coherence in monolayer WSe_2. *Nat Nano* **8,** 634–638 (2013).

140. Kioseoglou, G., Hanbicki, A. T., Currie, M., *et al.* Optical polarization and intervalley scattering in single layers of MoS_2 and $MoSe_2$. *Sci. Rep.* **6,** 25041 (2016).

141. Mai, C., Barrette, A., Yu, Y., *et al.* Many-body effects in valleytronics: Direct measurement of valley lifetimes in single-layer MoS_2. *Nano Lett.* **14,** 202–206 (2013).

142. Mai, C., Seme"nov", Y. G., Barrette, A., *et al.* Exciton valley relaxation in a single layer of WS_2 measured by ultrafast spectroscopy. *Phys. Rev. B* **90,** 041414 (2014).

143. Kim, J., Jin, C., Chen, B., *et al.* Observation of ultralong valley lifetime in WSe_2/MoS_2 heterostructures. *Sci. Adv.* **3,** e1700518 (2017).

144. Temnov, V. V. & Woggon, U. Superradiance and Subradiance in an Inhomogeneously Broadened Ensemble of Two-Level Systems Coupled to a Low-Q Cavity. *Phys. Rev. Lett.* **95,** 243602 (2005).

145. Scheibner, M., Schmidt, T., Worschech, L., *et al.* Superradiance of quantum dots. *Nat. Phys.* **3,** 106–110 (2007).

146. Cong, K., Zhang, Q., Wang, Y., *et al.* Dicke superradiance in solids. *J. Opt. Soc. Am. B* **33,** C80–C101 (2016).

147. Stevens, C. E., Stroucken, T., Stier, A. V., *et al.* Superradiant coupling effects in transition-metal dichalcogenides. *Optica* **5,** 749 (2018).

148. Paik, E. Y., Zhang, L., Burg, G. W., *et al.* Interlayer exciton laser of extended spatial coherence in atomically thin heterostructures. *Nature* **576,** 80–84 (2019).

149. Hümmer, T. *Cavity-Enhanced Hyperspectral Raman and Absorption Microscopy* PhD thesis (Ludwig-Maximilians-Universität München, 2019).

150. Uphoff, M., Brekenfeld, M., Rempe, G., *et al.* Frequency splitting of polarization eigenmodes in microscopic Fabry–Perot cavities. *New J. Phys.* **17,** 013053 (2015).

151. Alexeev, E. M., Mullin, N., Ares, P., *et al.* Emergence of highly linearly polarized interlayer exciton emission in $MoSe_2$/WSe heterobilayers with transfer-induced layer corrugation. *arXiv preprint.* arXiv: 2004.05624 (2020).

152. Zhang, L., Gogna, R., Burg, G. W., *et al.* Highly valley-polarized singlet and triplet interlayer excitons in van der Waals heterostructure. *Phys. Rev. B* **100,** 041402 (2019).

153. Wang, T., Miao, S., Li, Z., *et al.* Giant Valley-Zeeman Splitting from Spin-Singlet and Spin-Triplet Interlayer Excitons in $WSe_2/MoSe_2$ Heterostructure. *Nano Lett.* **20,** 694–700 (2020).

154. Calman, E. V., Fowler-Gerace, L. H., Choksy, D. J., *et al.* Indirect Excitons and Trions in $MoSe_2/WSe_2$ van der Waals Heterostructures. *Nano Lett.* **20,** 1869–1875 (2020).

155. Joe, A. Y., Jauregui, L. A., Pistunova, K., *et al.* Electrically controlled emission from triplet charged excitons in atomically thin heterostructures. *arXiv preprint.* arXiv: 1912.07678 (2019).

156. Delhomme, A., Vaclavkova, D., Slobodeniuk, A., *et al.* Flipping exciton angular momentum with chiral phonons in $MoSe_2$/WSe_2 heterobilayers. *arXiv preprint.* arXiv: 2002.11997 (2020).

157. Splendiani, A., Sun, L., Zhang, Y., *et al.* Emerging Photoluminescence in Monolayer MoS_2. *Nano Letters* **10,** 1271–1275 (2010).

158. Mak, K. F., Lee, C., Hone, J., *et al.* Atomically thin MoS_2: A New direct-gap semiconductor. *Phys. Rev. Lett.* **105,** 136805 (2010).

159. Liu, X., Galfsky, T., Sun, Z., *et al.* Strong light–matter coupling in two-dimensional atomic crystals. *Nat. Photonics* **9,** 30–34 (2015).

160. Ruiz-Tijerina, D. A. & Fal'ko, V. I. Interlayer hybridization and moir\'e superlattice minibands for electrons and excitons in heterobilayers of transition-metal dichalcogenides. *Phys. Rev. B* **99,** 125424 (2019).

161. Horng, J., Stroucken, T., Zhang, L., *et al.* Observation of interlayer excitons in $MoSe_2$ single crystals. *Phys. Rev. B* **97,** 241404 (2018).

162. Mak, K. F., He, K., Lee, C., *et al.* Tightly bound trions in monolayer MoS_2. *Nat. Mater.* **12,** 207–211 (2013).

163. Courtade, E., Semina, M., Manca, M., *et al.* Charged excitons in monolayer WSe_2: Experiment and theory. *Phys. Rev. B* **96,** 085302 (2017).

164. Li, Z., Wang, T., Lu, Z., *et al.* Direct Observation of Gate-Tunable Dark Trions in Monolayer WSe2. *Nano Lett.* (2019).

165. Brotons-Gisbert, M., Baek, H., Molina-Sánchez, A., *et al.* Spin-layer locking of interlayer valley excitons trapped in moiré potentials. *arXiv preprint* (2019).

166. Woźniak, T., Junior, P. E. F., Seifert, G., *et al.* Exciton g-factors of van der Waals heterostructures from first principles calculations. *arXiv preprint.* arXiv: 2002.02542 (2020).

167. Xuan, F. & Quek, S. Y. Valley Zeeman effect and Landau levels in Two-Dimensional Transition Metal Dichalcogenides. *arXiv preprint.* arXiv: 2002.11993 (2020).

168. Gerber, I. C., Courtade, E., Shree, S., *et al.* Interlayer excitons in bilayer MoS_2 with strong oscillator strength up to room temperature. *Phys. Rev. B* **99,** 035443 (2019).

169. Deilmann, T., Rohlfing, M. & Wurstbauer, U. Light-matter interaction in van der Waals heterostructures. *arXiv preprint.* arXiv: 2002.08066 (2020).

170. Nayak, P. K., Horbatenko, Y., Ahn, S., *et al.* Probing Evolution of Twist-Angle-Dependent Interlayer Excitons in $MoSe_2$/WSe_2 van der Waals Heterostructures. *ACS Nano* **11,** 4041–4050 (2017).

171. Hanbicki, A. T., Chuang, H.-J., Rosenberger, M. R., *et al.* Double Indirect Interlayer Exciton in a $MoSe_2$/WSe_2 van der Waals Heterostructure. *ACS Nano* **12,** 4719–4726 (2018).

172. Cao, Y., Fatemi, V., Demir, A., *et al.* Correlated insulator behaviour at half-filling in magic-angle graphene superlattices. *Nature* **556,** 80–84 (2018).

173. Cao, Y., Fatemi, V., Fang, S., *et al.* Unconventional superconductivity in magic-angle graphene superlattices. *Nature* **556,** 43–50 (2018).

174. Chen, G., Sharpe, A. L., Gallagher, P., *et al.* Signatures of tunable superconductivity in a trilayer graphene moiré superlattice. *Nature* **572,** 215–219 (2019).

175. Chen, G., Jiang, L., Wu, S., *et al.* Evidence of a gate-tunable Mott insulator in a trilayer graphene moiré superlattice. *Nat. Phys.* **15,** 237–241 (2019).

176. Wu, F., Lovorn, T., Tutuc, E., *et al.* Hubbard Model Physics in Transition Metal Dichalcogenide Moiré Bands. *Phys. Rev. Lett.* **121,** 026402 (2018).

177. Hümmer, T., Noe, J., Hofmann, M. S., *et al.* Cavity-enhanced Raman microscopy of individual carbon nanotubes. *Nat. Commun.* **7,** 12155 (2016).

178. Waldherr, M., Lundt, N., Klaas, M., *et al.* Observation of bosonic condensation in a hybrid monolayer $MoSe_2$ -GaAs microcavity. *Nat. Commun.* **9,** 3286 (2018).

179. Klembt, S., Harder, T. H., Egorov, O. A., *et al.* Exciton-polariton topological insulator. *Nature* **562,** 552–556 (2018).

180. Mounet, N., Gibertini, M., Schwaller, P., *et al.* Two-dimensional materials from high-throughput computational exfoliation of experimentally known compounds. *Nat. Nanotechnol.* **13,** 246–252 (2018).

181. Keldysh, L. V. Coulomb interaction in thin semiconductor and semimetal films. *JEPT Lett.* **29,** 658–661 (1979).

182. Rytova, N. S. The screened potential of a point charge in a thin film. *Mosc. Univ. Phys. Bull.* **3,** 18 (1967).

183. Han, B., Robert, C., Courtade, E., *et al.* Exciton states in monolayer $MoSe_2$ and $MoTe_2$ probed by upconversion spectroscopy. *Phys. Rev. X* **8,** 031073 (2018).

184. Kormányos, A., Zólyomi, V., Drummond, N. D., *et al.* Monolayer MoS_2: trigonal warping, the Γ valley, and spin-orbit coupling effects. *Phys. Rev. B* **88,** 045416 (2013).

185. Kormányos, A., Burkard, G., Gmitra, M., *et al.* K· p theory for two-dimensional transition metal dichalcogenide semiconductors. *2D Mater.* **2,** 022001 (2015).

List of Publications

P1. Lindlau, J., Robert, C., Funk, V., Förg, M., Colombier, L., Neumann, A., Taniguchi, T., Watanabe, K., Glazov, M. M., Marie, X., Urbaszek, B. & Högele, A. Identifying optical signatures of momentum-dark excitons in monolayer transition metal dichalcogenides. *arXiv preprint.* arXiv: 1710.00988 (2017).

P2. Förg, M., Colombier, L., Patel, R. K., Lindlau, J., Mohite, A. D., Yamaguchi, H., Glazov, M. M., Hunger, D. & Högele, A. Cavity-control of interlayer excitons in van der Waals heterostructures. *Nature Communications* **10,** 3697 (2019).

P3. Förg, M., Baimuratov, A. S., Kruchinin, S. Y., Vovk, I. A., Scherzer, J., Förste, J., Funk, V., Watanabe, K., Taniguchi, T. & Högele, A. Moiré excitons in $MoSe_2$-WSe_2 heterobilayers and heterotrilayers. *arXiv preprint.* arXiv: 2006.09105 (2020).

P4. Förste, J., Tepliakov, N. V., Kruchinin, S. Y., Lindlau, J., Funk, V., Förg, M., Watanabe, K., Taniguchi, T., Baimuratov, A. S. & Högele, A. Exciton g-factors in monolayer and bilayer WSe_2 from experiment and theory. *arXiv preprint.* arXiv: 2002.11646 (2020).

P5. Lindlau, J., Selig, M., Neumann, A., Colombier, L., Förste, J., Funk, V., Förg, M., Kim, J., Berghäuser, G., Taniguchi, T., Watanabe, K., Wang, F., Malic, E. & Högele, A. The role of momentum-dark excitons in the elementary optical response of bilayer WSe_2. *Nature Communications* **9,** 2586 (2018).

P6. Gebhardt, C., Förg, M., Yamaguchi, H., Bilgin, I., Mohite, A. D., Gies, C., Florian, M., Hartmann, M., Hänsch, T. W., Högele, A. & Hunger, D. Polariton hyperspectral imaging of two-dimensional semiconductor crystals. *Scientific Reports* **9,** 1–9 (2019).

List of Abbreviations

2D	two-dimensional
Ag	silver
APD	avalanche photodiode
Au	gold
CB	conduction band
CCD	charge-coupled device
CVD	chemical vapor deposition
DFT	density functional theory
DR	differential reflectance
FWHM	full-width at half-maximum
HBL	heterobilayer
hBN	hexagonal boron nitride
HTL	heterotrilayer
LP	linear polarizer
ML	monolayer
MoO_3	molybdenum trioxide
$MoSe_2$	molybdenum diselenide
NA	numerical aperture
PDMS	polydimethylsiloxane
PL	photoluminescence
PLE	photoluminescence excitation
PMMA	polymethyl methacrylate
PPC	polypropylene carbonate
ROC	radius of curvature
Se	selenium
SHG	second harmonic generation
Si	silicon

SiO_2	silicon dioxide
TMD	transition metal dichalchogenide
TRPL	time-resolved photoluminescence
VB	valence band
WO_3	tungsten trioxide
WP	wave plate
WS_2	tungsten disulfide
WSe_2	tungsten diselenide
ZPL	zero phonon line

Danksagung

Zum Schluss möchte ich allen danken, die mich während meiner Promotion unterstützt und begleitet haben.

Allen voran geht mein Dank an Alexander Högele, der mir die Möglichkeit gegeben hat in seiner Arbeitsgruppe zu forschen und zu promovieren. Danke, dass ich stets die Möglichkeit hatte, meine eigenen Ideen und Projekte zu verfolgen. In unseren Gesprächen über explorative Messungen sind wissenschaftliche Fragestellungen entstanden. Du hattest immer ein Auge fürs Detail und einen Blick dafür, welche Datensätze das Projekt noch sinnvoll ergänzen können.

Ein großer Dank gilt auch allen meinen Doktoranden-Kollegen aus unserer Arbeitsgruppe für das freundliche Arbeitsklima: Jonathan Förste, Victor Funk, Lukas Husel, Zhije Li, Jessica Lindlau, Andre Neumann, Jonathan Noé, Manuel Nutz, Johannes Scherzer und Samarth Vadia. Danke Manu, dass man immer mit Fragen zu sämtlichen Themen zu dir kommen konnte und du als unser Hackerman alle Computerprobleme lösen konntest. Danke Jonathan der Große für die wunderbare Reiseleitung in Japan und die beständigen kulinarischen Belehrungen. Danke Victor für die hilfreichen Gespräche, fürs Probenbauen und die nette Zeit in Dresden und Österreich. Danke großer Jonathan für die gemeinsamen Magnetfeldmessungen und deine Künste als Barista, die ich nur zu gern in Anspruch genommen habe. Thank you Samarth for sharing your wisdom regarding physics, papers and English with us and for giving me shelter in a windy night. Danke Johannes für deine Unterstützung beim Trilagen-Projekt.

I am also very grateful to our Postdocs for the collaborative work environment: Anvar Baimuratov, Ismail Bilgin, Leo Colombier, Xin Huang, Robin Patel and Shen Zhao. Thank you Anvar for explaining me all the theory. Thank you Leo and Robin for the joint measurements during the cavity-project.

Ein großes Dankeschön geht auch an alle aus der Arbeitsgruppe Hunger, die mir mit Rat und Tat bezüglich der Cavity zur Seite standen: David Hunger, Thomas Hümmer, Matthias Mader und Julia Benedikter.

Diese Arbeit wäre nicht möglich gewesen ohne die hervorragende Zusammenarbeit am Lehrstuhl. Hier geht ein Dank an Jörg Kotthaus, der den Lehrstuhl aufgebaut hat.

Danke an Heribert Lorenz, der im Hintergrund dafür sorgt, dass alles reibungslos funktioniert. Ein besonderes Dankeschön geht auch an Anton Heindl, der die Helium und Stickstoffversorgung aller Experimente gewährleistet. Reinhold Rath möchte ich für das Reparieren der Pumpen danken und Stephan Manus dafür, dass er sämtliche Elektronik wieder gangbar macht. Danke an Philipp Altpeter, unseren Meister des Reinraums, der zu Fragen rund um die Probenprozessierung immer die richtigen Antworten hat. Christian Obermayer möchte ich für das Justieren unserer Laser-Systeme danken. Ein weiteres Dankeschön geht an Martina Edenhofer und Dayse Ferreira e Silva fürs Kümmern um alle organisatorischen Belange.

Zum Schluss möchte ich mich bei meiner Familie bedanken, die mich in dieser Zeit so wunderbar unterstützt hat. Ein Dank geht an meine Eltern und Schwiegereltern, die zwar nie ganz verstanden haben was ich mache und warum ich das mag, aber sich doch immer geduldig angehört haben, was mich gerade beschäftigt. Am allermeisten möchte ich mich bei meiner Frau Theresa und meinen beiden Söhnen Lukas und Jakob bedanken. Ihr habt mir immer geholfen, wenn es gerade nicht gut lief und es war mir möglich, auf andere Gedanken zu kommen, sobald ich nach Hause kam. Ihr wart ein wunderbarer Ausgleich und eine unersetzbare Stütze. Danke Theresa, dass du mir oft den Rücken frei gehalten hast, mich immer wieder motiviert hast und an meiner Seite warst.